國立交通大學

機械工程學系

碩士論文

並聯矩陣整合型發電風車動力效率數值分析

A Numerical Analysis of Power Efficiency of Wind Rotor System in Parallel Matrix

研究生：馮嘉軒

指導教授：陳俊勳 教授

中華民國一〇〇年六月

並聯矩陣整合型發電風車動力效率數值分析

A Numerical Analysis of Power Efficiency of Wind Rotor System in Parallel Matrix

研究生：馮嘉軒
指導教授：陳俊勳

Student：Jia-Shiuan Feng
Advisor：Chiun-Hsun Chen

國立交通大學
機械工程學系
碩士論文

A Thesis
Submitted to Department of Mechanical Engineering
College of Engineering
National Chiao Tung University
In Partial Fulfiillment of the Requirements
For the Degree of
Master of Science
In Mechanical Engineering
June 2011
Hsinchu, Taiwan, Republic of China

中華民國一〇〇年六月

A Numerical Analysis of Power Efficiency of Wind Rotor System in Parallel Matrix

並聯矩陣整合型發電風車動力效率數值分析

學生：馮嘉軒　　　　指導教授：陳俊勳

國立交通大學機械工程學系

摘要

本研究使用流體力學套裝軟體 Fluent 分析二葉式 Savonius 風車周圍的流場與效能，研究主題分為單一風車與並聯矩陣系統，改變參數為風速、周速比及相位角差，此外探討風向對並聯矩陣系統的影響，最後討論兩個主題的差異，並與其他文獻之提升效能方法進行比較。

從模擬結果可得知，單一風車在同一周速比的情況下，功率係數（c_p）會隨風速提升而略微提高，另外比較單一風車在大氣與風洞中的情境後發現，由於風洞中邊界的影響，使得風車在大氣中的效能會低於在風洞中的情境。二維模擬結果顯示，在並聯矩陣系統中，相位角差 90°可得到最好的 c_p，為單一風車情況下的 2.05 倍。並聯矩陣系統的效能提升主要歸因於風車間的正向干擾情形，而流場的波動現象在此效應中扮演主要角色，但此種正向干擾效應受風向改變的影響極大。當風向改變 45°時，其效能會趨近於甚至低於單一風車情況下的效能。在三維模擬中，並聯矩陣系統的最大效能會達到單一風車的 1.45 倍，另外比較二維與三維 c_p 的差異，在單一風車條件下其比值為 1.28，而在並聯矩陣系統中為 1.83。

關鍵字：Savonius 風車、並聯矩陣系統、功率係數

A Numerical Analysis of Power Efficiency of Wind Rotor System in Parallel Matrix

Student: Jia-Shiuan Feng Advisor: Prof. Chiun-Hsun Chen

Department of Mechanical Engineering

National Chiao Tung University

ABSTRACT

This study employs a computational fluid dynamics (CFD) software, Fluent, to analyze the flow fields around two-bladed Savonius wind rotors and their corresponding performances. It is divided into two topics: one is a study of a single Savonius wind rotor, and the other is of a parallel matrix system. Both are carried out by the related parametric studies. The parameters for the single wind rotor are wind velocity and tip speed ratio. The ones for the parallel matrix system are wind velocity, tip speed ratio, phase angle difference and wind direction change. Then, comparison between the two systems is discussed. Besides, comparisons with other studies are also given.

The simulation results show that the c_p (power coefficient) of a single wind rotor slightly increases with wind speeds at the same tip speed ratio, and the performance of the one in atmosphere is lower than that inside the wind tunnel due to the influence of walls. In the 2-D simulation results of parallel matrix system, phase angle difference 90° can obtain the best c_p that is 2.05 times of that by a single wind rotor. The higher performance of parallel matrix system is resulted from the positive interaction between these Savonius wind rotors, and the flow fluctuation plays the major role in contributing to this effect, but this effect is strongly influenced by the change of wind direction. When wind direction is 45°, the c_p of the parallel matrix system becomes almost the same or even lower than that of a single one. The maximal c_p in the parallel matrix system by 3-D simulation is about 1.45 times of that by a single Savonius wind rotor. The ratio of 2-D c_p to 3-D one is 1.28 in the single Savonius wind rotor condition and 1.83 in the parallel matrix system.

Keywords: Savonius wind rotor; parallel matrix system; c_p (power coefficient)

ACKNOWLEDGEMENTS

首先必須感謝我的指導教授　陳俊勳教授，總是耐心地糾正我的錯誤並給予指導，使我在這兩年內學習到許多處理事情與解決問題的能力。感謝曾錦錬學長給了我這個題目並也給予許多指導。感謝老朋友伯華教導我許多風車模擬的技巧，淑敏在指導我的英文上有莫大的幫助，還有崔燕勇師門的林子翔同學也在模擬上給予我許多建議。另外也感謝國科會計畫的經費支持。

再來是感謝這兩年陪我一起度過的實驗室的諸位。云婷開心的笑聲是我每天的動力來源，當我遇到許多煩惱時妳也總是靜靜的聆聽並給予我建議與鼓勵。聖容是實驗室最厲害的開心果，沒有妳的話這兩年生活一定會失色不少。世庸是最常與我相處在一起的人，不管在瑣事還是正事上都給我許多幫助。與你們三個住在一起的這一年，一定是我這一生中非常重要的回憶。還有總是睡不飽的黃鈞，也是我一同前進與成長的好夥伴。感謝學長榮貴、瑭原、宗翰給予過我許多幫助，家維學長與彥成學長在模擬上也給了我許多建議，學弟凌宇、詠翔、鉦鈞與天洋則總是為我帶來歡笑，衷心希望你們接下來一年也能每天都開懷大笑。

感謝所有曾經給過我鼓勵的朋友們，雖然可能一時無法把名字都一一點出來，但你們曾經給予過我的，我都不會忘記。最後，必須鄭

重感謝我的父母，雖然我很常感到彷徨失措，但你們總相信自己的兒子一定是最好的，一定不會問題的，也永遠以笑容迎接我回家，這才是我在遇到挫折時還能繼續前進的最大動力。還有我親愛的哥哥與堂姐，你們的鼓勵也是這兩年不容忽視的一環。

　　也許我還不成熟，對於未來也依然感到茫然，只能持續摸索，但我知道在這兩年得到的許多珍貴的經驗與回憶，那是什麼都無法換走的。

CONTENTS

LIST OF TABLE

LIST OF FIGURES

CHAPTER 1

INTRODUCTION

1.1 Motivation

The world population is increasing at a fast rate, and the growth rate especially is quite high in developing countries. According to the calculation and projection of world population by the United Nations, there are 6.4 billion people in 2004, and the population will grow up to 8.5 billion in 2025 and 10 billion in 2050. As expected, the demands for energy and food are increasing simultaneously.

In 2008, total worldwide energy consumption was 474 exajoules (474×1018 J) with 80 to 90 percent from the combustion of fossil fuels. Dependence on fossil fuels may cause serious problems including not only the energy shortage crisis but also the rapid change of global climate due to carbon dioxide emissions. The dramatic rise in carbon dioxide emissions over the 20th and early 21st centuries (see **Fig. 1.1**) is because of the anthropogenic burning of fossil fuels primarily. Therefore, to replace fossil fuels with renewable energy causing no environmental impacts becomes an important issue. **Fig. 1.2** shows that renewable energy, such as the wind power or solar energy, has very low carbon dioxide emissions during production. Although nuclear energy emits no carbon dioxide during power generation either, but the impact of nuclear waste would cause more severe environmental problems than that of carbon dioxide emissions. Hence, researches of renewable energy are extremely of importance, and wind power plays an important role in this field.

Wind power is the conversion of wind energy into a useful form of energy by functioning wind turbines. They are classified into horizontal axis wind turbine (HAWT) and vertical axis wind turbine (VAWT) according to their appearances as shown in **Fig. 1.3**. The rotational axis of HAWTs is horizontal to the ground, and that of VAWTs is vertical. After a long period of development, almost all of the wind power generation systems adopt HAWTs because of their higher c_p (Power Coefficient) comparing to the one of VAWTs. Generally speaking, the c_p of HAWTs is ranged from 0.30 to 0.45, and that of VAWTs is about 0.15 to 0.30. However, there are some problems in using HAWTs. First, the high tip speed ratio of HAWTs causes low-frequency noise. Second, the distance between HAWTs should be sufficient to avoid interferences of wind fields. Third, sometimes HAWTs take a long time to be oriented in the wind direction. Last but not least, it might be a huge cost to install a HAWT for its land preparations, installation, maintenance, and repair. Therefore, feasibilities of VAWTs, which have lower costs and simple structures but with lower c_p should be taken into account with some improvements.

Although the c_p of VAWTs is lower than the one of HAWTs, there are ways to improve their performance. This research proposes an idea to achieve this purpose. Such idea is to put a plurality of VAWTs connecting in parallel with a fixed distance between them and they rotate with a specific phase angle difference. In this way, the performance would be improved by utilizing wind fields effectively. By adopting this idea, the present work is interesting in investigating the performance differences between a single general Savonius wind rotor (see **Fig. 1.4**) and a plurality of those installed in parallel by using Computational Fluid Dynamics (CFD) technique.

1.2 Literature Review

Shigetomi et al. [1] studied the interactive flow field around two Savonius wind rotors by experimental investigation using particle image velocimetry. They found that there exist power-improvement interactions between two rotating Savonius rotors in appropriate arrangements. The interactions are caused by the Magnus effect to provide the additional rotation of the downstream rotor and the periodic coupling of local flow between two wind rotors. However, the interactions of two wind rotors are sensitive to the direction of wind losing one of the advantages of VAWTs.

Antheaume et al. [2] applied a CFD software, Fluent, to investigate the performances of vertical-axis Darrieus wind rotors in different working fluids by using k-ε turbulent model under steady-state condition. They also discussed the average efficiency of several wind rotors connected in parallel. The results showed that increasing the number of wind rotors or decreasing the distance between wind rotors can make the efficiency higher due to the velocity streamlines straightening effect by the configuration. In addition, the performances working in water are much higher than those in air.

Fujisawa [3] studied the performances of two-bladed Savonius wind rotors with different overlap ratios ranged from 0 to 0.5 by experimental investigations. The results showed that the performance of a Savonius wind rotor reaches a maximum at overlap ratio 0.15 because the advancing blade is strengthened by the flow through the overlap. When the overlap ratio becomes larger, the recirculation zone grows causing a deterioration of the performance.

Blackwell et al. [4] investigated the performances of fifteen configurations of Savonius wind rotors by testing in a low speed wind tunnel. What they investigated included parameters, such as number of blades, wind velocity, wind rotor height, and blade overlap ratio. The results showed that first of all, the two-bladed configurations have better performance than the three-bladed ones, except starting torque. Second, the performance increases with aspect ratio slightly. Last, the optimum overlap ratio is 0.1 to 0.15.

Pope et al. [5] applied Fluent to investigate the performances of one VAWT and compared the predictions with experimental data. By the reason that a free spinning turbine cannot be fully simulated, they used constant rotational speeds of the VAWT in simulations and changed the specification of parameters to reveal freely moving turbine blades in experiments. They indicated that determining the performance at constant rotational speed is valuable since any power generation connected to the electricity grid needs to operate at constant speed.

Howell et al. [6] applied Fluent to investigate the performances of one VAWT in 2-D and 3-D simulations and compared the predictions with experimental data. The turbulence model used was RNG k-ε model, by which the applicability in flow fields involves large flow separations. The error bars on experimental data were fixed at ±20% of measured values. The results showed that the performances predicted by 2-D simulations are apparently higher than those by 3-D simulations and experimental data due to the effect of the over tip vortices.

Hu and Tong [7] used Fluent to analyze the performances in VAWT with windshield for decreasing the counter torque as shown in **Fig. 1.5**. They used k-ε RNG turbulent model and SIMPLE algorithm in 2-D simulations. The results showed that about 15° of inclination angle between the bottom of windshield and x-axis gives the highest value of torque.

Kamoji et al. [8] compared the performance differences between conventional Savonius wind rotors with and without central shaft between the end plates in an open jet wind tunnel. Investigation was undertaken to study the effects of overlap ratio, blade arc angle, aspect ratio and Reynolds number. The results showed that the performance of the Savonius wind rotor without central shaft is higher than that with central shaft.

Altan et al. [9] introduced a curtaining arrangement to improve the performance and increase the efficiency of a tow-bladed Savonius wind rotor without changing its basic structure. They placed two wind-deflecting plates in front of the wind rotor to prevent the negative torque opposite the wind rotor rotation. The experimental results showed that c_p is increased to about 38% with the optimum curtain arrangement and is much higher than 16% obtained without curtain.

Mohamed et al. [10] used a CFD software to investigate the performances of two-bladed and three-bladed Savonius wind rotors with and without putting an obstacle to prevent the influence of wind on the returning blade. They concluded that an appropriate arrangement of the obstacle can increases c_p by 27.3% for two-bladed Savonius wind rotors and 27.5% for three-bladed ones. Therefore, the overall effect of the obstacle is extremely positive for both designs. Furthermore, the two-bladed wind rotors are better than three-bladed configurations by considering the resultant c_p and the cost and complexity of the wind rotor.

Saha et al. [11] used a wind tunnel to test and investigate the performances by different number of blades and stages, different geometries of blade and inserting valves on the concave side of blade or not. The results were as follows. First, with an increases of the number of blades, the performance of wind rotor decreases. Second, twisted geometry blade profile has a better performance than the semicircular blade geometry. Third, the c_p of a two-stage Savonius wind rotor is higher than those of single-stage and three-stage wind rotors. Last, the valve-aided Savonius wind rotor with three blades shows a better performance than the conventional wind rotor.

Zhao et al. [12] applied computational fluid dynamics software to investigate the performance of new helical Savonius wind rotors. They analyzed the differences of the wind rotors with different aspects ratio, number of blades, overlap distance and helical angle. The results showed that three-blade helical wind rotor has lower c_p compared with two-bladed helical wind rotor. And the best overlap ratio, aspect ratio, and helical angle are 0.3, 6.0 and 180°, respectively.

Gupta et al. [13] studied the performances of a Savonius wind rotor and a Savonius-Darrieus machine with overlap variation by experimental investigations. For the Savonius-Darrieus machine, there was a two-bladed Savonius wind rotor in the upper part and a Darrieus machine in the lower side. The result showed that c_p with 20% overlap is higher than 16.2% without overlap. They also concluded that the improvement of c_p can be achieved for the Savonius-Darrieus wind machine compared with the general Savonius rotor.

Irabu and Roy [14] introduced a guide-box tunnel to improve the c_p of Savonius wind rotors and prevent the damage by strong wind disaster. The guide-box tunnel was like a rectangular box as wind passage and the test wind rotor was included. It was able to adjust the inlet mass flow rate by its variable area ratio between the inlet and outlet. The experimental results showed that the maximum c_p of the two-bladed wind rotor using the guide-box tunnel is about 1.23 times of c_p of the wind rotor without the guide-box tunnel and 1.5 times of a three-bladed wind rotor. Besides, the two-bladed wind rotor is better than the three-bladed in converting wind power through guide-box tunnel effectively, except the starting rotation.

Chinchilla et al. [15] studied the need for further researches and developments on improved airfoil or blade characteristics on straight bladed VAWT. They indicated that the asymmetric airfoils would enable VAWTs to self start and could be utilized in the regions of low or turbulent air.

Chang et al. [16] analyzed wind characteristics and wind turbine characteristics in Taiwan by mathematical formulations using the measured data of hourly mean wind speed at 25 weather stations from 1961 to 1999. They indicated that in the west coast, Hengchun Peninsula and some small surrounding islands, there are outstanding wind sources being suitable for wind power generation.

1.3 Scope of Present Study

This study employs a computational fluid dynamics (CFD) software, Fluent, to analyze the flow fields around two-bladed Savonius wind rotors and their corresponding performances. The scope of this study is illustrated in **Fig. 1.6**. First, a reference case is established, and the comparison between simulation results and experimental data is given to ensure the capability of the applied model. Then this research is divided into two topics: one is a study of a single Savonius wind rotor, and the other is of a parallel matrix system. Both the two topics are carried out by the corresponding parametric studies. The parameters for the single wind rotor are wind velocity and tip speed ratio, and for the parallel matrix system are wind velocity, tip speed ratio and phase angle difference. After that, the influence of wind direction change on the parallel system is also studied. Then, comparisons between the two systems are discussed. Besides, comparisons with other researches, such as improvements by adding windshields or twisted rotor systems, are also given.

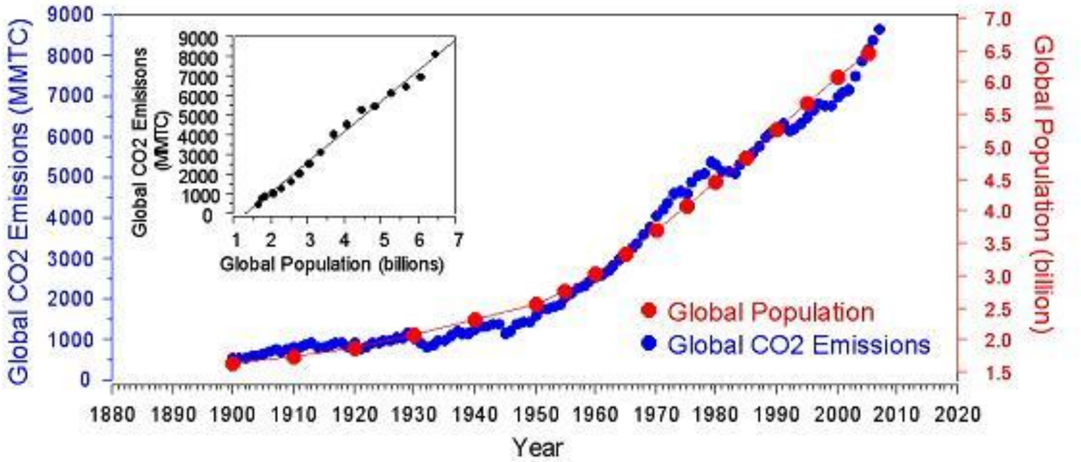

Fig. 1.1 Evolution of global population and global carbon dioxide emissions since 1900

http://www.worldclimatereport.com/index.php/2008/01/30/what-the-future-holds-in-store/

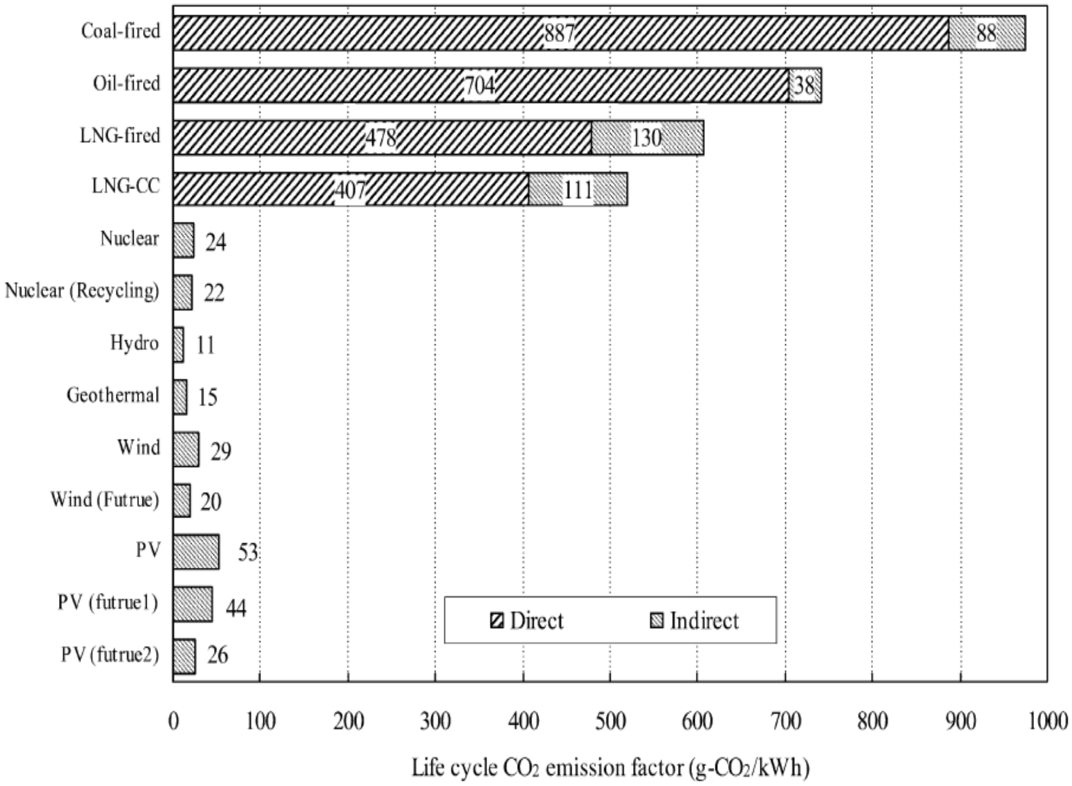

Fig. 1.2 Life cycle CO_2 emission factors for different types of power generation systems [16]

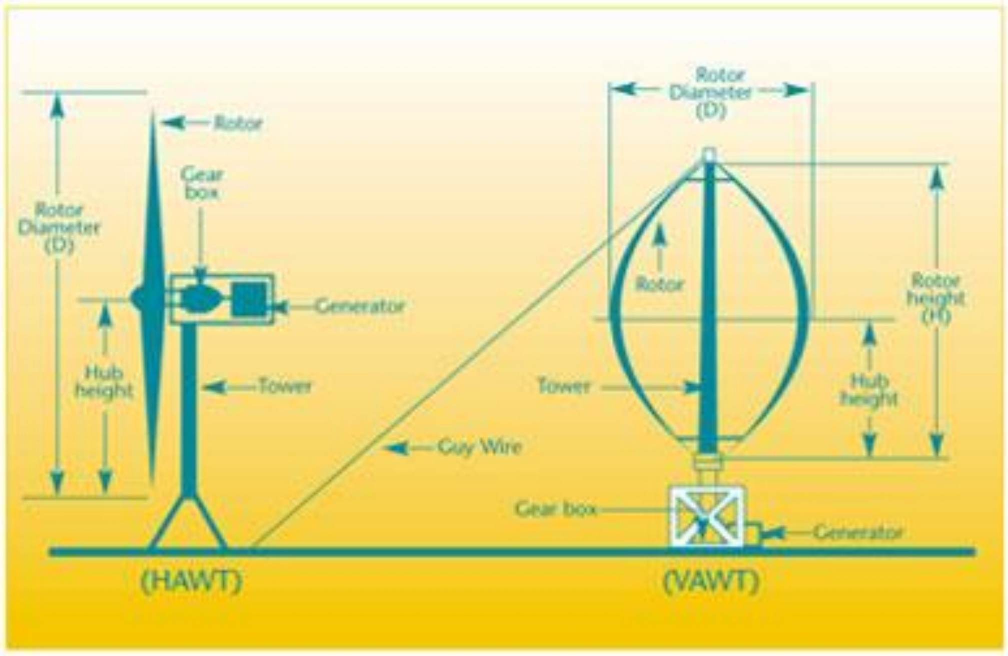

Fig. 1.3 Wind turbine configurations

http://colonizeantarctica.blogspot.com/

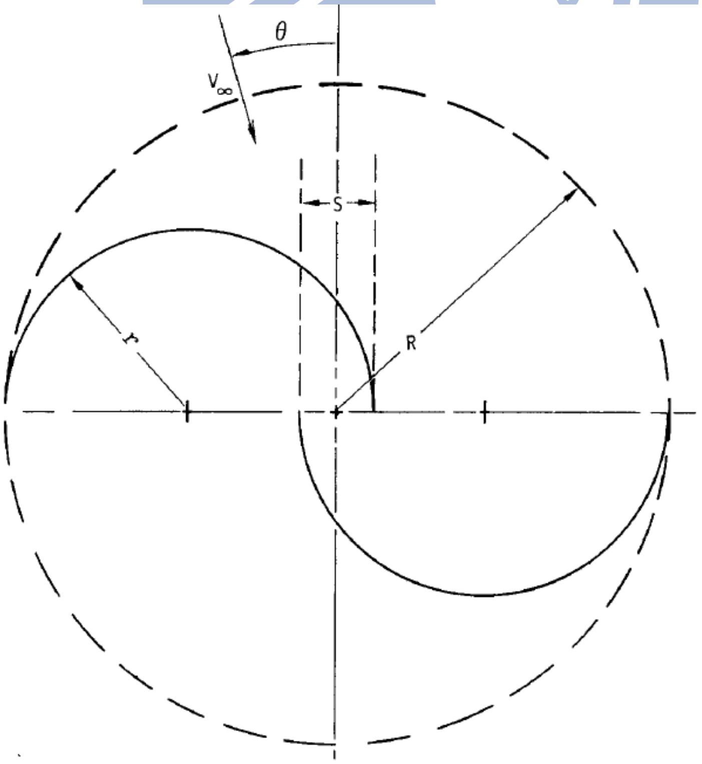

Fig. 1.4 Schematic of a two-bladed Savonius wind rotor [4]

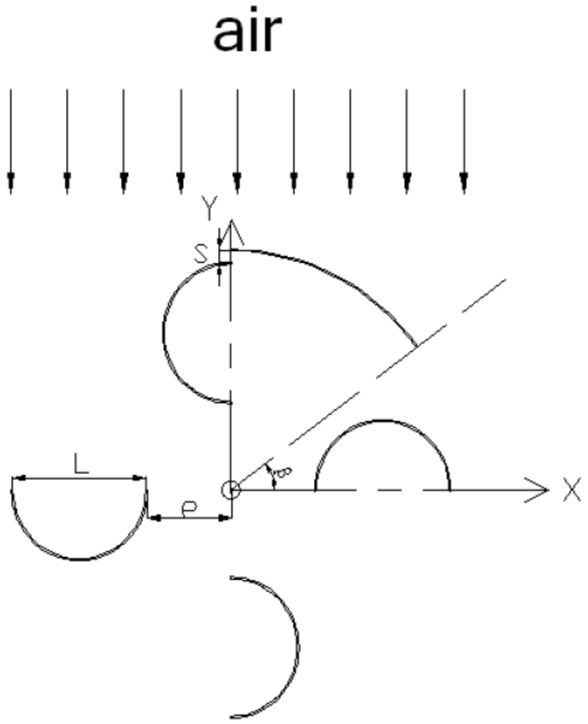

Fig. 1.5 VAWT with windshield [6]

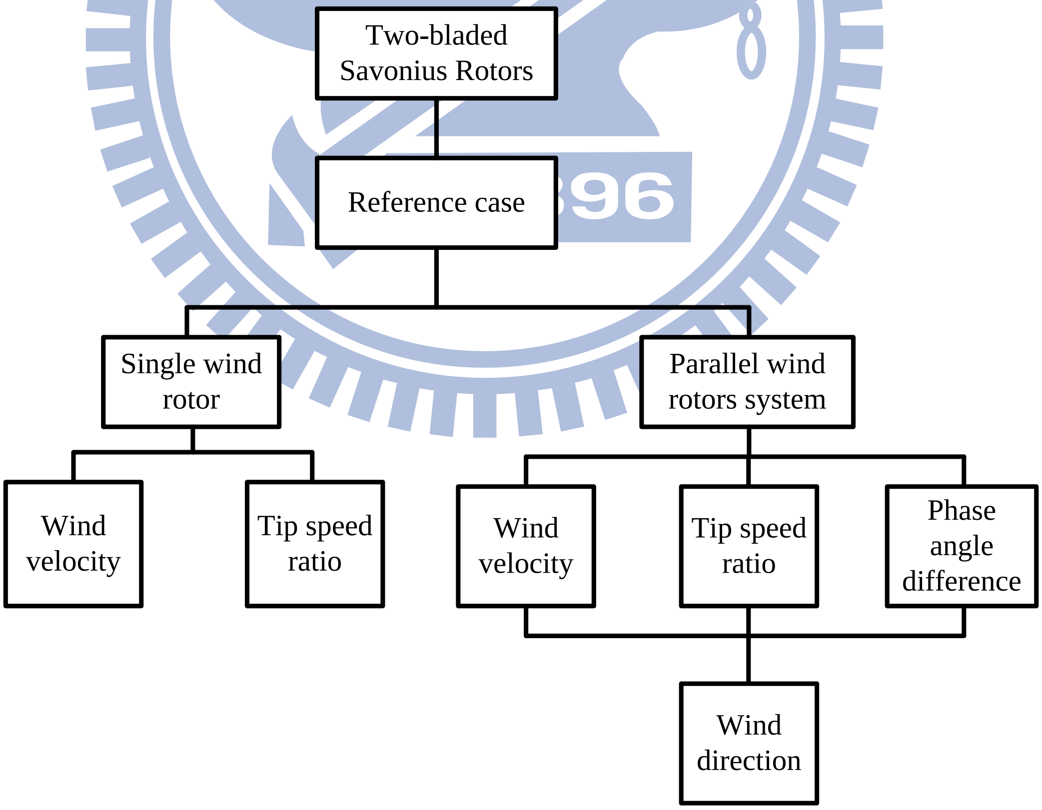

Fig. 1.6 The scope of this study

CHAPTER 2

FUNDAMENTALS OF WIND ENERGY

2.1 Brief History of Wind Energy

The first wind machine was known as appearing about 2200 years ago in Persia for grinding grains. Then the Romans used the same way for the same purpose around 250 A.D. By the fourteenth century, the Dutch employed windmills to drain water in the low-lying areas of the Rhine River delta.

The first use of windmill for producing electricity was in 1888. And the first such windmill was built and used by Charles Brush in Ohio, U.S.A. Ten years later, about 72 wind turbines were being used to produce electricity in the range of about 5 to 25kW.

In the twentieth century, wind turbines were used around the world. There existed many small electricity generating sites in Denmark, and wind power was a large part of them. In Australia, wind turbines were used to power remote post offices. In America, rural farms had used wind power originally. Eventually, this generated electricity was connected to grid later. By 1930, more than six million wind turbines had been manufactured in American and it was the first time that the utilization of wind energy was based on an industrially mass-produced. The first megawatt wind turbine was built in USA in 1941. In the 1970s and 1980s, the U.S. Government promoted the technology through NASA and researched many of the designs that still use today.

In the end of 2002, there was roughly 32GW of power supplied from wind energy in the world. Europe has been the leader in wind power utilization, contributing 76% of the total. In 2006, roughly 65GW of rated power were installed in wind farms worldwide, of which more than 47GW located in Europe, and more than 11GW in the United States.

2.2 Basics of Wind Energy Conversion

2.2.1 Power Conversion and Power Coefficient

From the expression for kinetic energy in flowing air, the power contained in the wind passing an area A with the wind velocity v_1 is:

$$P_W = \frac{\rho}{2} A v_1^3 \tag{2-1}$$

where ρ is air density, depending on air pressure and moisture. For practical calculations it may be assumed $\rho \approx 1.225 kg/m^3$. The air streams in axial direction through the wind turbine, of which *A* is the swept area. The useful mechanical power obtained is expre2ssed by means of the power coefficient c_p:

$$P = c_p \frac{\rho}{2} A v_1^3 \tag{2-2}$$

The wind velocity, whose value ahead of the turbine plane is v_1, suffers retardation due to the power conversion to a speed v_3 far behind the wind turbine, as shown in **Fig. 2.1**. Simplified theory claims that in the plane of the moving blades the velocity is of average value $v_2 = (v_1 + v_3)/2$. On this basis, Betz has shown by a simple calculation that the maximum useful power can be obtained for $v_3/v_1 = 1/3$ in 1920; where the power coefficient $c_p = 16/27 \approx 0.593$. In reality, wind turbine displays the maximum values $c_{p,\ max} = 0.4 \sim 0.5$ due to losses, such as profile loss, tip loss and loss due to wake rotation. In order to determine the mechanical power available for the load machine, such as electrical generator or pump, Eq. (2-2) has to be multiplied with an efficiency of the drive train, taking losses in bearings, couplings and gear boxes into account.

An important parameter of wind rotor is the tip-speed ratio λ. It is defined as a ratio of the circumferential velocity of blade tips to the wind speed:

$$\lambda = {}^{u}/_{v_1} = \frac{D}{2} \cdot \frac{\omega}{v_1} \tag{2-3}$$

where D is the outer turbine diameter and ω the angular wind rotor speed.

Considering that in the rotating mechanical system, the power is the product of torque T and angular speed ω (P = T · ω), then c_p becomes

$$c_p = \frac{P}{P_W} = \frac{T \cdot \omega}{\frac{1}{2}\rho A v_1^3} \tag{2-4}$$

Fig. 2.2 shows typical characteristics c_p (λ) for different types of wind rotors. Besides the constant maximum value according to Betz, the figure indicates a revised curve c_p by Schmitz, who takes the downstream deviation from axial air flow direction into account. The difference is notable in the region of lower tip speed ratios.

2.2.2 Wind Energy Converters Using Aerodynamic Drag or Lift

The momentum theory by Betz indicates the physically based, ideal limit value for the extraction of mechanical power from free-stream airflow without considering the design of the energy converter. However, the power which can be achieved under real conditions cannot be independent of the characteristics of the energy converter. The first fundamental difference which considerably influences the actual power depends on which aerodynamic forces are utilized for producing mechanical power. All bodies exposed to an airflow experience aerodynamic forces, which are defined as aerodynamic drag in the flow direction, and as aerodynamic lift perpendicular to the flow direction. The real power coefficients obtained are greatly dependent on whether aerodynamic drag or aerodynamic lift is used.

2.2.2.1 Drag Devices

The simplest type of wind energy conversion can be achieved by means of pure drag surfaces as shown in **Fig. 2.3**. The air impinges on the surface A with wind velocity v, and then the drag D can be calculated from the air density ρ, the surface area A, the wind velocity v, and the aerodynamic drag coefficient c_D as

$$D = c_D \frac{1}{2} \rho A v_r^2 = c_D \frac{1}{2} \rho A (v - u)^2 \tag{2-5}$$

The relative velocity, $v_r = v - u$, which effectively impinges on the drag area, is determined by wind velocity v and blade rotating speed $u = \omega R_M$, in which R_M is the mean radius. Then the resultant power is

$$P = D \cdot u = \frac{1}{2} \rho A v^3 \left[c_D \left(1 - \frac{u}{v}\right)^2 \frac{u}{v} \right] = \frac{1}{2} \rho A v^3 c_p \tag{2-6}$$

Analog to the approach described in Chapter 2.2.1, it can be shown that c_p reaches a maximum value with a velocity ratio of u/v = 1/3. The maximum value of c_p is then

$$c_{p,max} = \frac{4}{27} c_D \tag{2-8}$$

It is taken into account that the aerodynamic drag coefficient C_D of a concave surface curved against the wind direction can hardly exceed a value of 1.3. Thus, the maximum power coefficient $c_{p,\,max}$ of a general drag-type wind rotor becomes about 0.2, only one third of Betz's ideal c_p value of 0.593.

2.2.2.2 Lift Devices

Utilization of aerodynamic lift on wind rotor blade can achieve much higher power coefficients. The lift blade design employs the same principle that enables airplanes to fly. As shown in **Fig. 2.4**, when air flows over the blade, a pressure gradient is created between the upper and lower blade surfaces. The pressure at the lower surface is greater and thus acts to lift the blade. The lift occurred on a body by wind can be calculated from the air density ρ, acting area A, wind speed v, and aerodynamic lift coefficient c_L as

$$L = c_L \frac{1}{2} \rho A v^2 \tag{2-9}$$

When blades are attached to the central axis of a wind rotor, the lift is translated into rotational motion. All modern wind rotor types are designed for utilizing this effect, and the best type suited for this purpose is with a horizontal rotational axis. The aerodynamic force created is divided into a component in the direction of free-stream velocity, the drag D, and a component perpendicular to the free-stream velocity, the lift L. The lift force L can be further divided into a component L_{torque} in the plane of rotation of the wind rotor, and a component L_{thrust} perpendicular to the plane of rotation. L_{torque} constitutes the driving torque of the wind rotor.

Modern airfoils, developed for aircraft wings and which are also applied in wind rotors, have an extremely favorable lift-to-drag ratio. It could show qualitatively how much more effective the utilization of aerodynamic lift as a driving force must be. However, it is no longer possible to calculate the power coefficients of lift-type wind rotors quantitatively with the aid of elementary physical relationships alone.

2.3 Vertical and Horizontal Axis Wind Rotors

Wind rotors are approximately classified into two general types by their orientations: horizontal-axis type and vertical-axis type. A horizontal-axis wind rotor has its blades rotating on an axis parallel to the ground and a vertical-axis one has that rotating on an axis perpendicular to the ground. There are a number of designs for both, and each type has certain advantages and disadvantages.

However, the number of vertical-axis wind rotor for commercial uses is much less than that of horizontal-axis wind rotor.

2.3.1 Wind Rotors with a Vertical Axis of Rotation

The oldest design of wind rotors is with a vertical axis of rotation. At the beginning, vertical-axis wind rotors could only be built for using aerodynamic drag. It was only recently that engineers succeeded in developing vertical-axis designs which could also utilize aerodynamic lift effectively. Darrieus proposed such design which has been considered as a promising concept for modern wind turbines in 1925. The Darrieus wind rotor resembles a gigantic eggbeater and the geometric shape of the wind rotors blades is complicated that is difficult to manufacture. Furthermore, there is a variation of the Darrieus wind rotor which is called H-rotor. Instead of curved wind rotor blades, straight blades connected to the wind rotor shaft by struts are used.

Savonius wind rotor, which is investigated in this research, is also one type of vertical-axis wind rotors. The wind rotor was invented by a Finnish engineer, Savonius in 1922. Savonius wind rotor is one of the simplest wind rotors to manufacture. Because it is drag-type devices, Savonius wind rotor extracts much less of the wind power than the other similarly-sized lift-type wind rotor.

2.3.2 Horizontal Axis Wind Rotors

The earliest design of this wind turbine type was the big Dutch-style windmill, used for milling grain primarily. Another early type of these turbines was the windmill that was on most all farms in the early twentieth century. This type of wind turbines is the dominant design principle in wind energy technology today. The undisputed superiority of this design to date is primarily based on the reason that the wind rotor blade shape can be aerodynamically optimized and the highest efficiency can be achieved when aerodynamic lift is utilized appropriately.

These turbines usually need to adjust the angle of the entire wind rotor with the change of wind direction. They achieve the objective by using a yaw system which can move the entire wind rotor left or right in small increments. They can also control the wind rotor torque and power output by adjusting the blade angle using the pitching mechanism. However, designs differing from standard concept are also common and simplifications of construction, such as the absence of the pitching mechanism, can be found, particularly in small wind turbines.

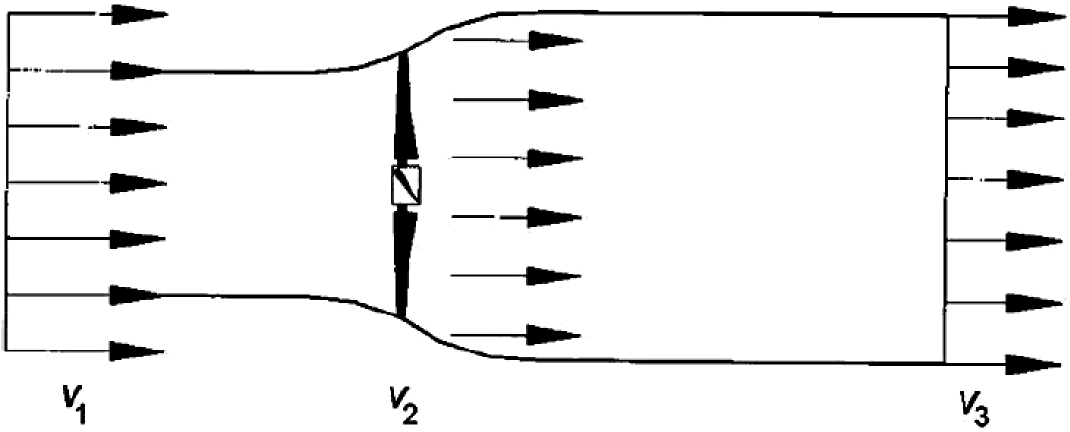

Fig. 2.1 Idealized fluid model for a wind rotor [17]

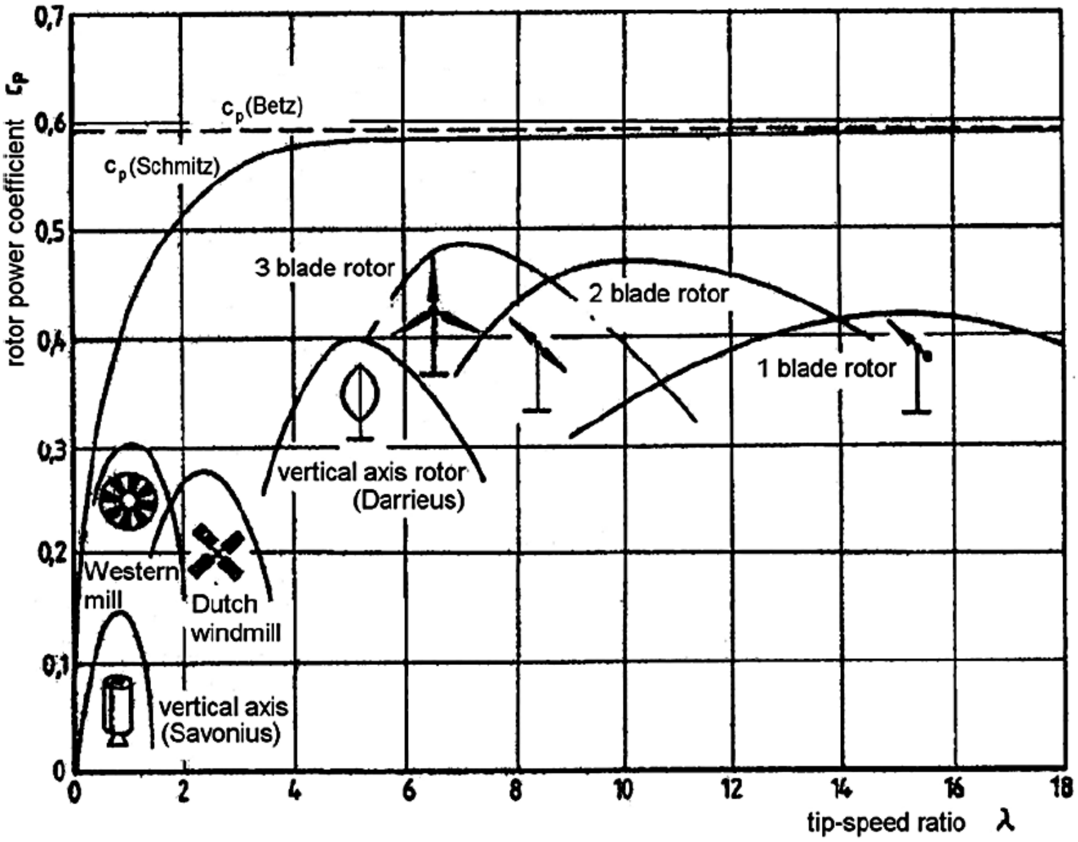

Fig. 2.2 Typical power coefficients of different wind rotor types over tip-speed ratio [17]

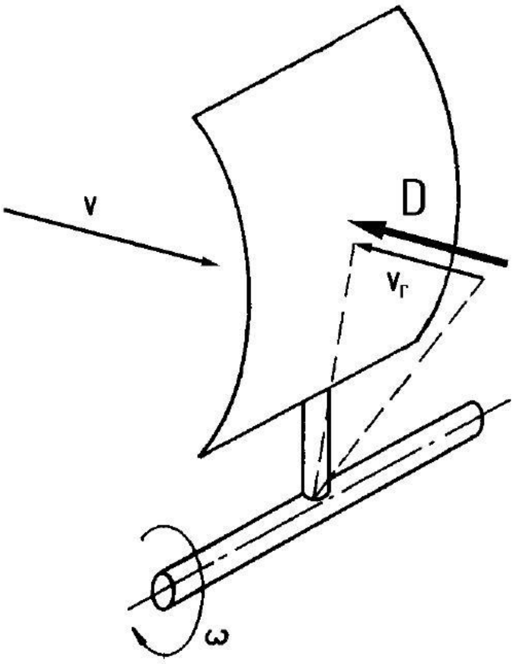

Fig. 2.3 Flow conditions and aerodynamic forces with a drag device [18]

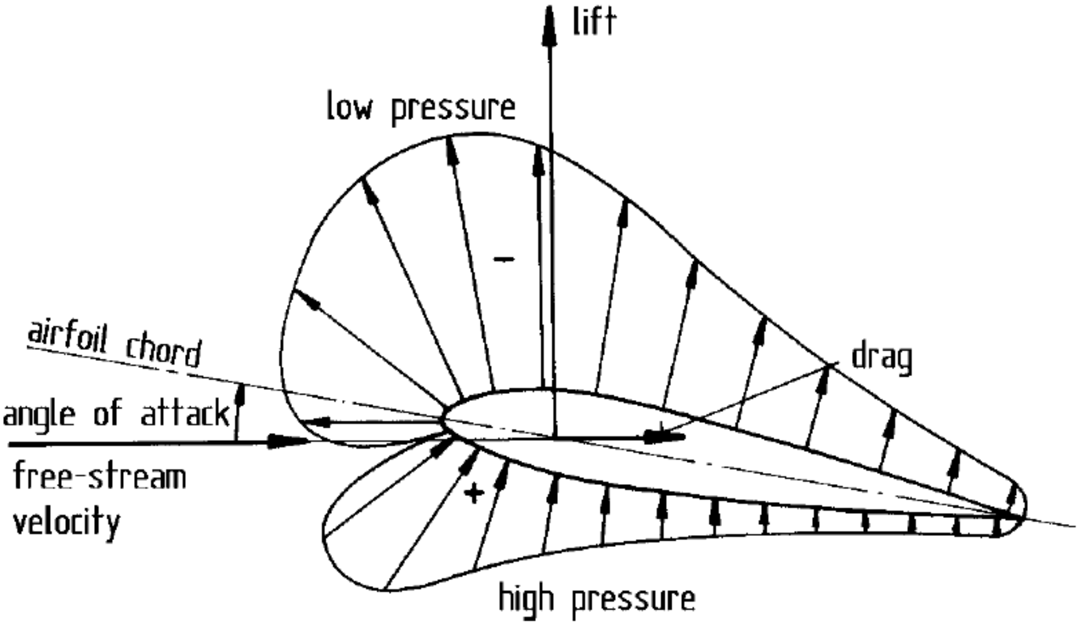

Fig. 2.4 Aerodynamic forces acting on an airfoil exposed to an air stream [18]

CHAPTER 3

MATHEMATICAL MODEL AND NUMERICAL ALGORITHM

3.1 Domain Descriptions

In this work, it is interesting to analyze the air flow field around one single rotating Savonius wind rotor firstly in conditions of different wind speeds and tip speed ratios by employing a CFD software, Fluent. Later, the studies of the parallel matrix system with three Savonius wind rotors in conditions of different wind speeds, tip speed ratios and phase angle differences are carried out. The influence of wind direction change on the parallel system is also studied.

The reference case in this work simulates the experimental one by Blackwell et al. [4]. The geometry of a two-bladed Savonius wind rotor is given in **Fig. 1.4** and the corresponding information is summarized in **Table 3.1**.

Table 3.1 Geometry Information

Number of Blades	2
Height (m)	1
Diameter (m)	0.9
Overlap Ratio of Blades	0.15

In order to simulate the situations of the reference case and the two topics mentioned above, three types of rectangular domains are set as shown in **Figs. 3.1, 3.2** and **3.3**, respectively. The first type including one single Savonius wind rotor inside the wind tunnel corresponds with the reference case; the second one is for the case of one single Savonius wind rotor in atmosphere; and the last is for the case of three Savonius wind rotors rotating with the same angular speed and connected in parallel in atmosphere with fixed distance. The distance between the centers of two wind rotors is 1.2m. All the conditions consider both 2-D and 3-D simulations. The dimensions of these domains are listed in **Table 3.2**.

Table 3.2 Dimensions of Domains

	Length	Width	Height (3-D)
A Single Rotor Inside (Reference)	11.9m	4.6m	2m
A Single Rotor in Atmosphere	14.5m	8m	2m
Three-rotor in Atmosphere	14.5m	10m	2m

Furthermore, the domains including three Savonius wind rotors with different wind directions are set as shown in **Fig. 3.4**, and the angles of wind direction are 0°, ±15°, ±30° and ±45°. For simplification, it does not include the consideration of the shaft of wind rotors.

3.2 Governing Equations

In order to make the physical problem more tractable, some assumptions are made as follows:

1. The flow is incompressible.
2. Turbulent expression applies the RNG k-ε model.

3. Neglect the heat transfer and buoyancy effects.

Based on the assumptions mentioned above, the governing equations are given in the following.

3.2.1 The Continuity and Momentum Equation

Turbulent flows are characterized by fluctuating velocity field. In Reynolds averaging, the solution variables in the instantaneous (exact) Navier-Stokes equations are decomposed into the mean (ensemble-averaged or time-averaged) and fluctuating components. For the velocity components:

$$u_i = \overline{u_i} + u_i{'} \tag{3-1}$$

where $\overline{u_i}$ and $u_i{'}$ are the mean and fluctuating velocity components (i = 1, 2, 3).

Likewise, for pressure and other scalar quantities:

$$\phi = \overline{\phi} + \phi' \tag{3-2}$$

where ϕ denotes a scalar such as pressure, energy, or species concentration. Substituting expressions of this form for the flow variables into the instantaneous continuity and momentum equations and taking a time (or ensemble) average (and dropping the overbar on the mean velocity, $\overline{u}$) yields the ensemble-averaged momentum equations. They can be written in Cartesian tensor form as:

$$\frac{\partial \rho}{\partial t} + \frac{\partial}{\partial x_j}(\rho u_i) = 0 \tag{3-3}$$

$$\frac{\partial}{\partial t}(\rho u_i) + \frac{\partial}{\partial x_j}(\rho u_i u_j) = -\frac{\partial P}{\partial x_i} + \frac{\partial}{\partial x_j}\left[\mu\left(\frac{\partial u_i}{\partial x_j} + \frac{\partial u_j}{\partial x_i} - \frac{2}{3}\delta_{ij}\frac{\partial u_l}{\partial x_l}\right)\right] + \frac{\partial}{\partial x_j}\left(-\rho\overline{u_i{'}u_j{'}}\right) \tag{3-4}$$

Eq. (3-3) and (3-4) are called Reynolds-averaged Navier-Stokes (RANS) equations. They have the same general form as the instantaneous Navier-Stokes equations, with the velocities and other solution variables now representing ensemble-averaged (or time-averaged) values. Additional terms now appear that represent the effects of turbulence. These Reynolds stresses, $-\rho\overline{u_i{}'u_j{}'}$, must be modeled in order to close Eq. (3-4).

3.2.2 RNG k-ε Model

The RNG-based k-ε turbulence model is derived from the instantaneous Navier-Stokes equations, using a mathematical technique called “renormalization group" (RNG) methods. The analytical derivation results in a model with constants different from those in the standard k-ε model. The additional terms and functions in the transport equations for k and ε are also different.

Transport Equations for the RNG k-ε Model

The turbulence kinetic energy, k, and its rate of dissipation, ε, are obtained from the following transport equations:

$$\frac{\partial}{\partial t}(\rho k) + \frac{\partial}{\partial x_i}(\rho k u_i) = \frac{\partial}{\partial x_j}\left(\alpha_k \mu_{eff} \frac{\partial k}{\partial x_j}\right) + G_k - \rho\varepsilon + S_k \tag{3-5}$$

and

$$\frac{\partial}{\partial t}(\rho\varepsilon) + \frac{\partial}{\partial x_i}(\rho\varepsilon u_i) =$$

$$\frac{\partial}{\partial x_j}\left(\alpha_\varepsilon \mu_{eff} \frac{\partial \varepsilon}{\partial x_j}\right) + C_{1\varepsilon}\frac{\varepsilon}{k}(G_k) - C_{2\varepsilon}\rho\frac{\varepsilon^2}{k} - R_\varepsilon + S_\varepsilon \tag{3-6}$$

The term of G_k represents the production of turbulence kinetic energy. From the exact equation for the transport of k, this term may be defined as $G_k = -\rho\overline{u_i{}'u_j{}'}\frac{\partial u_j}{\partial x_i}$. The quantities α_k and α_ε are the inverse effective Prandtl numbers for k and ε, respectively. S_k and S_ε are user-defined source terms.

Modeling the Turbulent Viscosity

The scale elimination procedure in RNG theory results in a differential equation for turbulent viscosity:

$$d\left(\frac{\rho^2 k}{\sqrt{\varepsilon\mu}}\right) = 1.72\frac{\hat{v}}{\sqrt{\hat{v}^3-1+C_v}}d\hat{v} \tag{3-7}$$

where

$$\hat{v} = \mu_{eff}/\mu$$

$$C_v \approx 100$$

Eq. (3-7) is integrated to obtain an accurate description of how the effective turbulent transport varies with the effective Reynolds number (or eddy scale), allowing the model to be better handled in the low-Reynolds-number and near-wall flows.

In the high-Reynolds-number limit, Eq. (3-7) gives

$$\mu_t = \rho C_\mu \frac{k^2}{\varepsilon} \tag{3-8}$$

with C_μ = 0.0845, derived using RNG theory.

RNG Swirl Modification

Turbulence, in general, is affected by rotation or swirl in the mean flow. The RNG model in FLUENT provides an option to account for the effects of swirl or rotation by modifying the turbulent viscosity appropriately. The modification takes the following functional form:

$$\mu_t = \mu_{t0}\, f(\alpha_s, \Omega, \frac{k}{\varepsilon}) \tag{3-9}$$

where μ_{t0} is the value of turbulent viscosity calculated without the swirl modification using either Eq. (3-7) or Eq. (3-8). Ω is a characteristic swirl number evaluated within FLUENT, and α_s is a swirl constant that assumes different values depending on whether the flow is swirl-dominated or only mildly swirling. This swirl modification always takes effect for axisymmetric, swirling flows and three-dimensional flows when the RNG model is selected. For mildly swirling flows (the default in FLUENT), α_s is set to 0.07. For strong swirling flows, however, a higher value of α_s can be used.

Calculating the Inverse Effective Prandtl Numbers

The inverse effective Prandtl numbers, k and ε, are computed using the following formula derived analytically by the RNG theory:

$$\left|\frac{\alpha-1.3929}{\alpha_0-1.3929}\right|^{0.6321}\left|\frac{\alpha+2.3929}{\alpha_0+2.3929}\right|^{0.3769}=\frac{\mu_{mol}}{\mu_{eff}} \tag{3-10}$$

where α_0= 1.0. In the high-Reynolds-number limit $(\mu_{mol}/\mu_{eff} \ll 1)$, $\alpha_k = \alpha_\varepsilon \approx 1.393$.

The R_ε Term in the ε Equation

The main difference between the RNG and standard k-ε models lies in the additional term in the ε equation given by

$$R_\varepsilon = \frac{C_\mu \rho \eta^3 (1-\eta/\eta_0)}{1+\beta\eta^3}\frac{\varepsilon^2}{k} \tag{3-11}$$

where $\eta \equiv S_k/\varepsilon$, η_0=4.38, β=0.012.

The effects of this term in the RNG ε equation can be seen more clearly by rearranging Eq. (3-6). Using Eq. (3-11), the third and fourth terms on the right-hand side of Eq. (3-6) can be merged, and the resultant ε equation can be rewritten as

$$\frac{\partial}{\partial t}(\rho\varepsilon)+\frac{\partial}{\partial x_i}(\rho\varepsilon u_i)=\frac{\partial}{\partial x_j}\left(\alpha_\varepsilon\mu_{eff}\frac{\partial\varepsilon}{\partial x_j}\right)+C_{1\varepsilon}\frac{\varepsilon}{k}(G_k+C_{3\varepsilon}G_b)-C^*_{2\varepsilon}\rho\frac{\varepsilon^2}{k} \qquad (3\text{-}12)$$

where $C^*_{2\varepsilon}$ is given by

$$C^*_{2\varepsilon}\equiv C_{2\varepsilon}+\frac{C_\mu\eta^3(1-{}^{\eta}/_{\eta_0})}{1+\beta\eta^3} \qquad (3\text{-}13)$$

In regions where $\eta < \eta_0$, the R term makes a positive contribution, and $C^*_{2\varepsilon}$ becomes larger than $C_{2\varepsilon}$. In the logarithmic layer, for instance, it can be shown that $\eta \approx 3.0$ gives $C^*_{2\varepsilon} \approx 2.0$, which is close in magnitude to the value of $C^*_{2\varepsilon}$ in the standard k-**ε** model (1.92). As a result, for weakly to moderately strained flows, the RNG model tends to give results largely comparable to the standard k-**ε** model.

In regions of large strain rate ($\eta > \eta_0$), however, the R term makes a negative contribution, making the value of $C^*_{2\varepsilon}$ less than $C_{2\varepsilon}$. In comparison with the standard k-**ε** model, the smaller destruction of **ε** augments **ε**, reducing k and, eventually, the effective viscosity. As a result, in rapidly strained flows, the RNG model yields a lower turbulent viscosity than the standard k-**ε** model.

Thus, the RNG model is more responsive to the effects of rapid strain and streamlining curvature than the standard k-**ε** model, which explains the superior performance of the RNG model for certain classes of flows.

Model Constant

The model constants C1**ε** and C2**ε** in Eq. (3-6) have values derived analytically by the RNG theory. These values, used by default in FLUENT, are

$$C_{1\varepsilon}=1.42, C_{2\varepsilon}=1.68$$

3.2.3 Standard Wall Functions

The standard wall functions in FLUENT are based on the proposal of

Launder and Spalding (1974), and have been most widely used for industrial flows.

Momentum

The law-of-the-wall for mean velocity yields

$$U^* = \frac{1}{k}\ln(Ey^*) \tag{3-14}$$

where

$$U^* \equiv \frac{U_P C_\mu{}^{1/4} k_P{}^{1/2}}{\tau_w/\rho} \tag{3-15}$$

$$y^* \equiv \frac{\rho C_\mu{}^{1/4} k_P{}^{1/2} y_P}{\mu} \tag{3-16}$$

In which

k = von Karman constant (=0.487)

E = empirical constant (=9.793)

U_P = mean velocity of the fluid at point P

K_P = turbulent kinetic energy at point P

y_P = distance from point P to the wall

μ = dynamic viscosity of the fluid

3.3 Boundary Conditions

In the model domain, there exist boundary conditions for the followings: rotation of the wind rotor, inlet surfaces, outlet surfaces, physical symmetric surfaces, and wall boundary conditions.

1. Rotation boundary condition

According to Eq. (2-3), the angular speed ω (rad/s) of the wind rotor is expressed as

$$\omega = \frac{2v_1\lambda}{D} \tag{3-23}$$

where D is the outer wind rotor diameter, ω the angular wind rotor speed, v_1 the wind velocity and λ the tip speed ratio.

2. The inlet boundary condition

The inlet boundary conditions are:

$$u = u_{in}$$

$$v = 0$$

$$w = 0$$

where u, v and w represent the velocity components in X, Y and Z directions, respectively.

3. The outflow boundary condition

Out flow boundary conditions are used to model flow exits where the details of the low velocity and pressure are not known.

4. The symmetrical boundary conditions

They can be used to model zero-shear slip walls in viscous flows. These surfaces are not affected by frictions. ($\frac{\partial u}{\partial y} = 0$)

5. Wall boundary conditions

The wall boundary conditions satisfy the no-slip condition (u, v, w =0) for velocity.

3.4 Introduction to FLUENT Software

FLUENT is a state-of-the-art computer program for modeling fluid flow and heat transfer in complex geometries. It provides complete mesh flexibility, including the ability to solve the flow problems using unstructured meshes that can be generated about complex geometries with relative ease. Supported mesh types include 2D triangular/quadrilateral, 3D tetrahedral/hexahedral/pyramid, and mixed (hybrid) meshes. FLUENT also allows refining or coarsening grid based on the flow solution.

FLUENT is written in the C computer language and makes full use of the flexibility and power offered by the language. Consequently, true dynamic memory allocation, efficient data structures, and flexible solver control are all possible. In addition, FLUENT uses a client/server architecture, which allows it to run as separate simultaneous processes on client desktop workstations and powerful compute servers. This architecture allows for efficient execution, interactive control, and complete flexibility between different types of machines or operating systems.

All functions required to compute a solution and display the results are accessible in FLUENT through an interactive, menu-driven interface.

3.5 Numerical Method

This study employs the computational fluid dynamics software Fluent to analyze the flow fields around rotating Savonius wind rotors. The finite volume iteration and SIMPLE algorithm are put in use to solve the governing equations of a transient flow field. And the corresponding grid movement is also solved by using sliding mesh method.

FLUENT uses Segregated Solver method to solve the governing integral equations for the conservation of mass and momentum, and (when appropriate) for energy and other scalars such as turbulence and chemical species. In case a control-volume-based technique is used that consists of:

- Division of the domain into discrete control volumes using a computational grid.
- Integration of the governing equations on the individual control volumes to construct algebraic equations for the discrete dependent variables such as velocities, pressure, temperature, and conserved scalars.
- Linearization of the discretized equations and solution of the resultant linear equation system to yield updated values of the dependent variables.

3.5.1 Segregated Solution Method

Using this approach, the governing equations are solved sequentially (i.e., segregated from one another). Because the governing equations are non-linear (and coupled), several iterations of the solution loop must be performed before a converged solution is obtained. Each iteration consists of the steps illustrated in **Fig. 3.5** and outlined below:

1. Fluid properties are updated, based on the current solution. (If the calculation has just begun, the fluid properties will be updated based on the initialized solution.)
2. The u, v, and w momentum equations are each solved in turn using current values for pressure and face mass fluxes, in order to update the velocity field.
3. Since the velocities obtained in Step 2 may not satisfy the continuity equation locally, a Poisson-type equation for the pressure correction is derived from the continuity equation and the linearized momentum equations. This

pressure correction equation is then solved to obtain the necessary corrections to the pressure and velocity fields and the face mass fluxes such that continuity is satisfied.

4. Where appropriate equations for scalars such as turbulence, energy, species, and radiation are solved using the previously updated values of the other variables.
5. When interphase coupling is to be included, the source terms in the appropriate continuous phase equations may be updated with a discrete phase trajectory calculation.
6. A check for convergence of the equation set is made.

These steps are continued until the convergence criteria are met.

3.5.2 Linearization: Implicit

In the segregated solution method the discrete, non-linear governing equations are linearized to produce a system of equations for the dependent variables in every computational cell. The resultant linear system is then solved to yield an updated flow-field solution.

The manner in which the governing equations are linearized may take an implicit form with respect to the dependent variable (or set of variables) of interest.

The implicit form is described in the following:

- Implicit: For a given variable, the unknown value in each cell is computed using a relation that includes both existing and unknown values from neighboring cells. Therefore each unknown will appear in more than one equation in the system, and these equations must be solved simultaneously to give the unknown quantities.

In the segregated solution method each discrete governing equation is linearized implicitly with respect to that equation's dependent variable. This will result in a system of linear equations with one equation for each cell in the domain. Because there is only one equation per cell, this is sometimes called a scalar system of equations. A point implicit (Gauss-Seidel) linear equation solver is used in conjunction with an algebraic multigrid (AMG) method to solve the resultant scalar system of equations for the dependent variable in each cell. For example, the x-momentum equation is linearized to produce a system of equations in which u velocity is the unknown. Simultaneous solution of this equation system (using the scalar AMG solver) yields an updated u-velocity field.

In summary, the segregated approach solves for a single variable field (e.g., p) by considering all cells at the same time. It then solves for the next variable field by again considering all cells at the same time, and so on. There is no explicit option for the segregated solver.

3.5.3 Discretization

FLUENT uses a control-volume-based technique to convert the governing equations to algebraic equations that can be solved numerically. This control volume technique consists of integrating the governing equations about each control volume, yielding discrete equations that conserve each quantity on a control-volume basis.

Discretization of the governing equations can be illustrated most easily by considering the steady-state conservation equation for transport of a scalar quantity ϕ. This is demonstrated by the following equation written in integral form for an arbitrary control volume V as follows:

$$\oint \rho\phi\vec{v}\cdot d\vec{A} = \oint \Gamma_{\phi}\nabla\phi\cdot d\vec{A} + \oint_{V} S_{\phi}dV \tag{3-24}$$

where

ρ = density

$\vec{v}$ = velocity vector

$\vec{A}$ = surface area vector

Γ_{ϕ} = diffusion coefficient for ϕ

$\nabla\phi$ = gradient of ϕ

S_{ϕ} = source of ϕ per unit volume

Eq. (3-24) is applied to each control volume, or cell, in the computational domain. The two-dimension, triangular cell shown in **Fig. 3.6** is an example of such a control volume. Discretization of Eq. (3-24) on a given cell yields

$$\sum_{f}^{N_{faces}} \rho_{f}\vec{v}_{f}\phi_{f}\cdot\vec{A}_{f} = \sum_{f}^{N_{faces}} \Gamma_{\phi}(\nabla\phi)_{n}\cdot\vec{A}_{f} + S_{\phi}V \tag{3-25}$$

where

N_{faces} = number of faces enclosing cell

ϕ_{f} = value of ϕ convected through face f

$\rho_{f}\vec{v}_{f}\cdot\vec{A}_{f}$ = mass flux through the face

$\vec{A}_{f}$ = area of face f

$(\nabla\phi)_{n}$ = magnitude of $\nabla\phi$ normal to face f

V = cell volume

The equations solved by FLUENT take the same general form as the one given above and apply readily to multi-dimension, unstructured meshes composed of arbitrary polyhedral.

By default, FLUENT stores discrete values of the scalar ϕ at the cell center (c0 and c1 in **Fig. 3.6**). However, face values ϕ_{f} are required for the convection terms in Eq. (3-25) and must be interpolated from the cell center values. This is accomplished using an upwind scheme.

First-Order Upwind Scheme

When first-order accuracy is desired, quantities at cell faces are determined by assuming that the cell-center values of any field variable represent a cell-average value and hold throughout the entire cell; the face quantities are identical to the cell quantities. Thus when first-order upwind is selected, the face value ϕ_f is set equal to the cell-center value of ϕ in the upstream cell.

3.5.4 SIMPLE Algorithm

The SIMPLE algorithm uses a relationship between velocity and pressure corrections to enforce mass conservation and to obtain the pressure field.

If the momentum equation is solved with a guessed pressure field p*, the resulting face flux J_f^*, computed from $J_f = \hat{J}_f + d_f(p_{c0} - p_{c1})$ (where p_{c0} and p_{c1} are the pressures within the two cells on either side of the face, and $\hat{J}_f$ contains the influence of velocities in these cell. The term d_f is a function of $\bar{a}_p$, the average of the momentum equation $\bar{a}_p$ coefficients for the cells on either side of face f.)

$$J_f^* = \hat{J}^*{}_f + d_f(p_{c0}^* - p_{c1}^*) \tag{3-26}$$

does not satisfy the continuity equation. Consequently, a correction J_f' is added to the face flux J_f^* so that the corrected face flux, J_f

$$J_f = J_f^* + J_f' \tag{3-27}$$

satisfies the continuity equation. The SIMPLE algorithm postulates that J_f'

be written as

$$J_f' = d_f(p_{c0}' + p_{c1}') \tag{3-28}$$

where p' is the cell pressure correction.

The SIMPLE algorithm substitutes the flux correction equations, Eq. (3-27) and (3-28), into the discrete continuity equation ($\sum_f^{N_{faces}} J_f A_f = 0$) to obtain a discrete equation for the pressure correction p' in the cell:

$$a_p p' = \sum_{nb} a_{nb} p_{nb}' + b \tag{3-29}$$

where the source term b is the net flow rate into the cell:

$$b = \sum_f^{N_{faces}} J_f^* A_f \tag{3-30}$$

The pressure-correction equation, Eq. (3-29), may be solved using the algebraic multigrid (AMG) method. Once a solution is obtained, the cell pressure and the face flux are used correctly.

$$p = p^* + \alpha_p p' \tag{3-31}$$

$$J_f = J_f^* + d_f(p_{c0}' - p_{c1}') \tag{3-32}$$

Here α_p is the under-relaxation factor for pressure. The corrected face flux J_f satisfies the discrete continuity equation identically during each iteration.

3.5.5 Sliding Mesh

The sliding mesh model allows adjacent grids to slide relative to one another. In doing so, the grid faces do not need to be aligned on the grid interface. This situation requires a means of computing the flux across the two non-conformal interface zones of each grid interface.

To compute the interface flux, the intersection between the interface zones is determined at each new time step. The resulting intersection produces one interior zone (a zone with fluid cells on both sides) and one or more periodic zones. If the problem is not periodic, the intersection produces one interior zone and a pair of wall zones (which will be empty if the two interface zones intersect entirely), as shown in **Fig. 3.7**. The resultant interior zone corresponds to where the two interface zones overlap; the resultant periodic zone corresponds to where they do not. The number of faces in these intersection zones will vary as the interface zones move relative to one another. Principally, fluxes across the grid interface are computed using the faces resulting from the intersection of the two interface zones, rather than from the interface zone faces themselves.

In the example shown in **Fig. 3.8**, the interface zones are composed of faces A-B and B-C, and faces D-E and E-F. The intersection of these zones produces the faces a-d, d-b, b-e, etc. Faces produced in the region where the two cell zones overlap (d-b, b-e, and e-c) are grouped to form an interior zone, while the remaining faces (a-d and c-f) are paired up to form a periodic zone. To compute the flux across the interface into cell IV, for example, face D-E is ignored and faces d-b and b-e are used instead, bringing information into cell IV from cells I and III, respectively.

3.6 Computational Procedure of Simulation

The complete operating procedure for using FLUENT package software is carried out through the following processes sequentially.

3.6.1 Model Geometry

For FLUENT calculations, it is necessary to build a model firstly. This study used the pre-processor software Gambit to build the case study model. It has to divide the case study into finite volumes in this step in order to generate grids conveniently. The details of geometry information can be referred in Section 3.1.

3.6.2 Grid Generation

After building the case study model, it has to use the pre-processor Gambit to generate grids as shown in **Fig. 3.9**. It defines the different grid sizes in different volumes in this step. Defining the smaller grid size for the smaller volume will increase the accuracy of the simulation, but it must consider the applicability of the grid size. If it adopts too small grid size in this step, the simulation time will be influenced. Besides, if the largest grid size is different from the smallest one too much, it will influence the FLUENT calculation.

3.6.3 FLUENT Calculation

Once determine the important features of the problem that one wants to solve, it will follow the basic procedural steps shown below.

1. Create the model geometry and grid.
2. Start the appropriate solver for 2D or 3D modeling.
3. Import the grid.
4. Check the grid.
5. Select the solver formulation.
6. Choose the basic equations to be solved: laminar or turbulent (or inviscid), chemical species or reaction, heat transfer models, etc. Identify additional models needed: fans, heat exchangers, porous media, etc.
7. Specify material properties.
8. Specify the boundary conditions.

9. Adjust the solution control parameters.
10. Initialize the flow field.
11. Calculate a solution.
12. Examine the results.
13. Save the results.
14. If necessary, refine the grid or consider revisions to the numerical or physical model.

3.6.4 Grid-independence Test

To justify numerical solutions acceptable, the grid-independence test should be taken.

As described in Section 3.1, there are three types of rectangular domain: one single Savonius wind rotor inside the wind tunnel, one single Savonius wind rotor in atmosphere, and three Savonius wind rotors in atmosphere. The grid-independence tests in 2-D simulations of these three types are carried out first.

In the case of one single Savonius wind rotor inside the wind tunnel, the boundary conditions of wind velocity 7 m/s and tip-speed ratio 0.86 are taken. Grid numbers of 7979, 10158, 13115, 15988 and 19049 are tested and the simulation results are shown in **Fig. 3.10(a)**. Because the changing rate of c_p from grid number 13115 to 15988 is small enough and remains almost the same value while the grid number increases, the number 13115 is selected.

The grid numbers of 9659, 11906, 15423, 18508 and 21755 in the case of one single Savonius wind rotor in atmosphere and 20921, 24377, 28469, 31719 and 35607 in three wind rotors in atmosphere are considered. The boundary conditions for both cases adopt wind velocity as 7 m/s and tip-speed ratio as 0.7.

The results are shown in **Fig. 3.10 (b)** and **(c)**. The same reason as the case inside the wind tunnel, grid numbers 15423 and 28469 are selected accordingly.

Now, the grid-independence tests of Z-axis in 3-D domain are also taken. The case of one single Savonius wind rotor inside the wind tunnel and grid number 13115 in 2-D domain is chosen, and the boundary conditions of wind velocity 7 m/s and tip-speed ratio 0.86 are used. The grid numbers 20, 40, 56, 72 and 96 in Z-axis are set and the corresponding results are shown in **Fig. 3.10 (d)**. For the same reason as above, the number 56 in Z-axis is selected.

The selected grids numbers of all the domains are listed in **Table 3.3**.

Table 3.3 Grid Numbers of all the Domains

	Grid Number (2-D)	Grid Number (3-D)
A Single Rotor Inside (Reference)	13115	741524
A Single Rotor in Atmosphere	15423	886676
Three-rotor in Atmosphere	28469	1608796

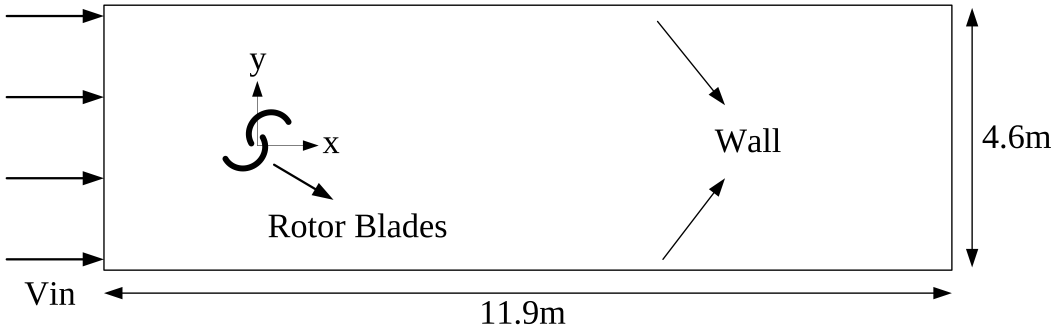

Fig. 3.1 The domain for one single Savonius wind rotor inside the wind tunnel (Reference)

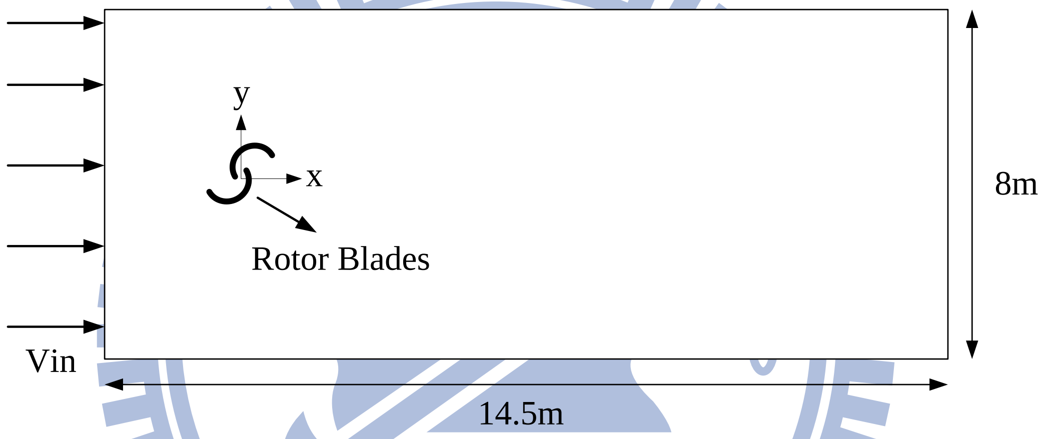

Fig. 3.2 The domain for one single Savonius wind rotor in atmosphere

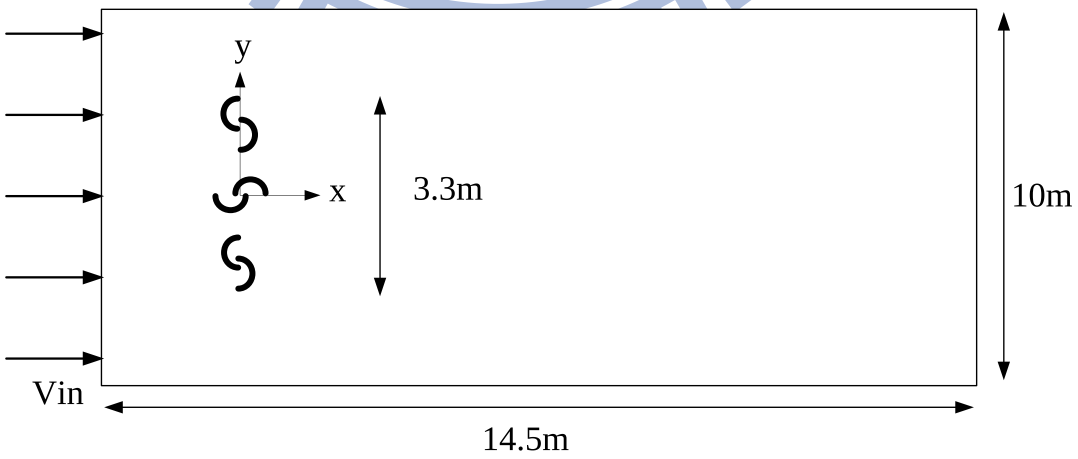

Fig. 3.3 The domain for three Savonius wind rotors in atmosphere

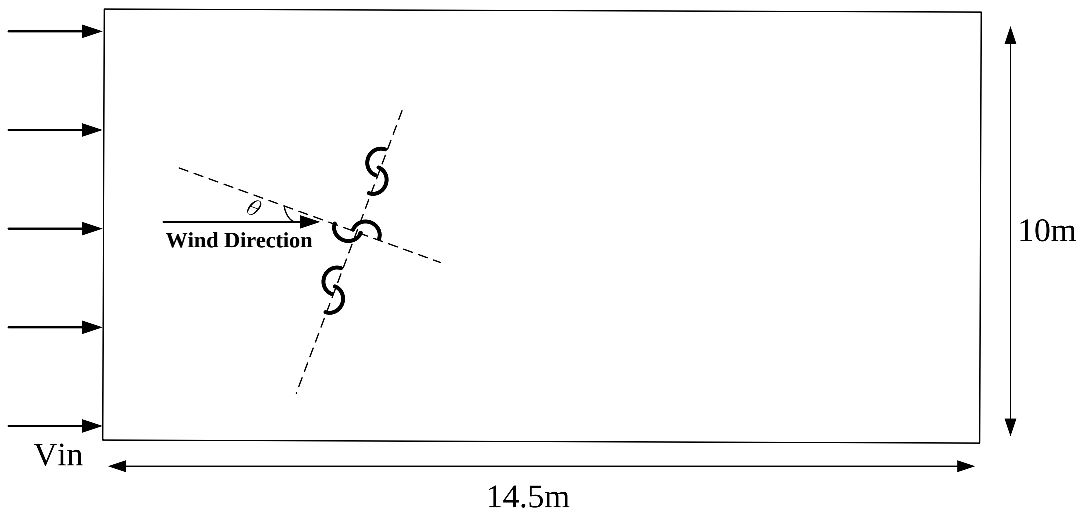

Fig. 3.4 The domain for three Savonius wind rotors in atmosphere with different wind direction (θ=0°, ±15°, ±30°, ±45°)

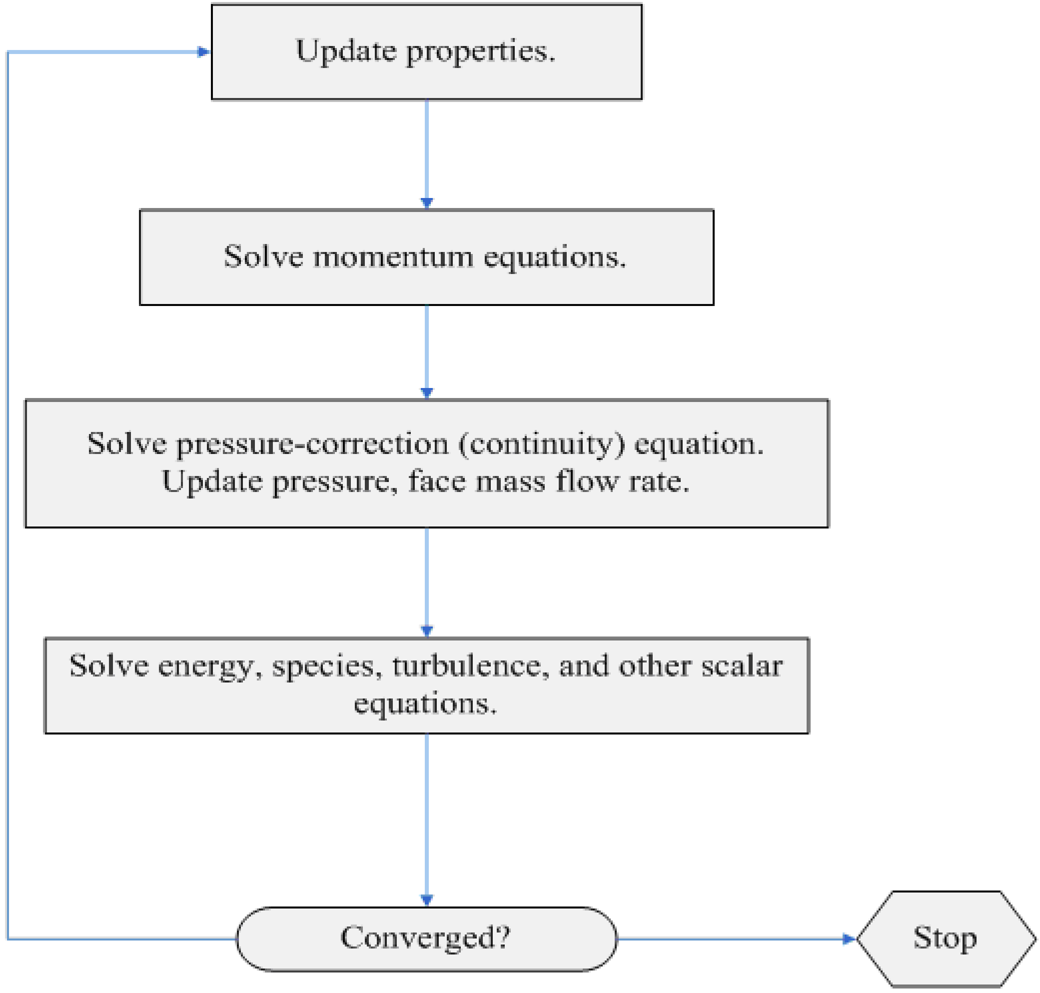

Fig. 3.5 Overview of the Segregated Solution Method

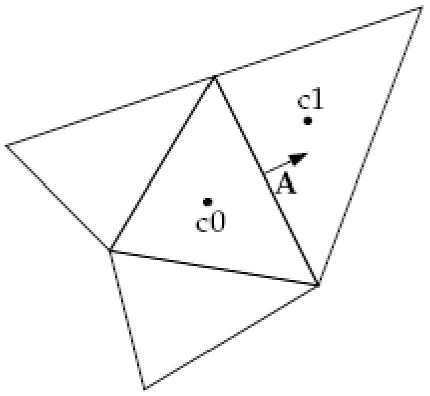

Fig. 3.6 Control Volume Used to Illustrate Discretization of a Scalar Transport Equation

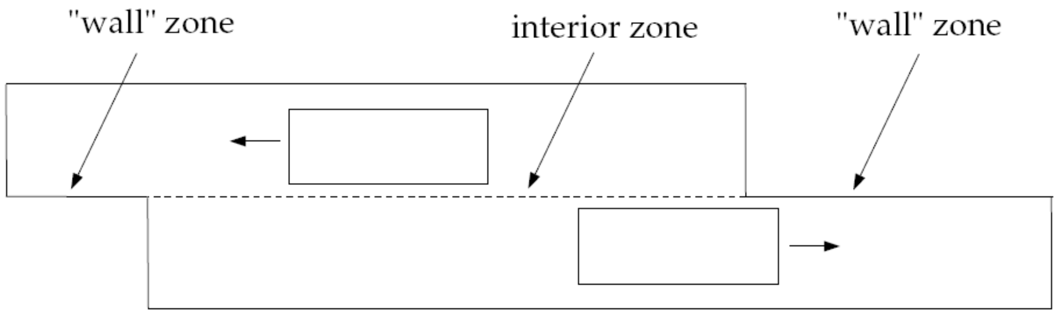

Fig. 3.7 Zones Created by Non-Periodic Interface Intersection

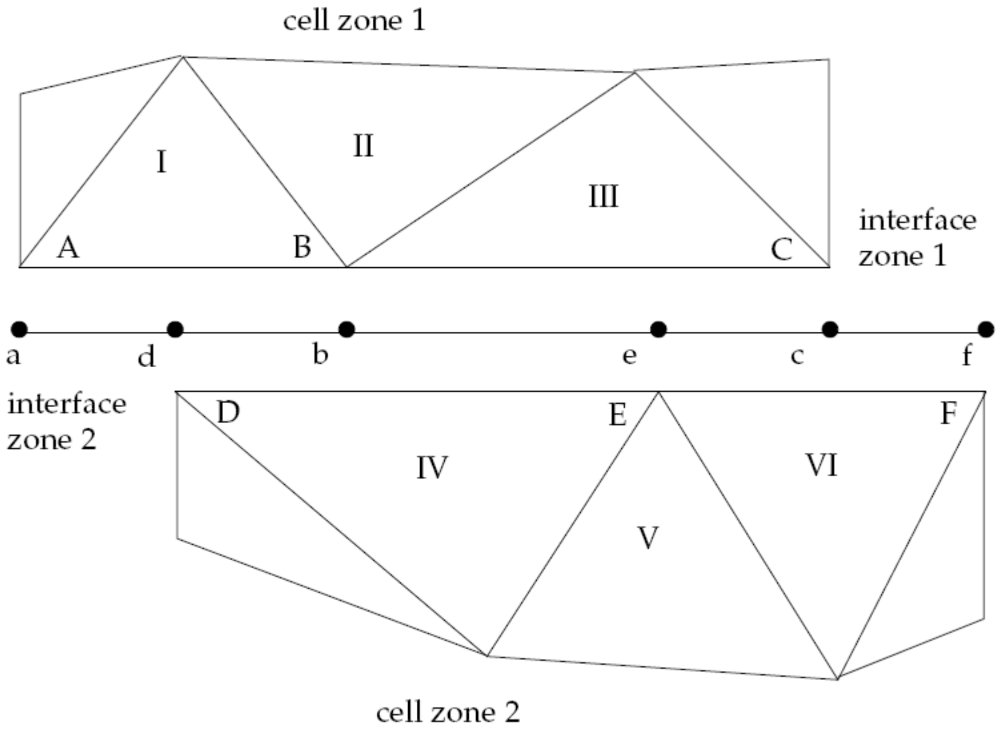

Fig. 3.8 Two-Dimensional Grid Interface

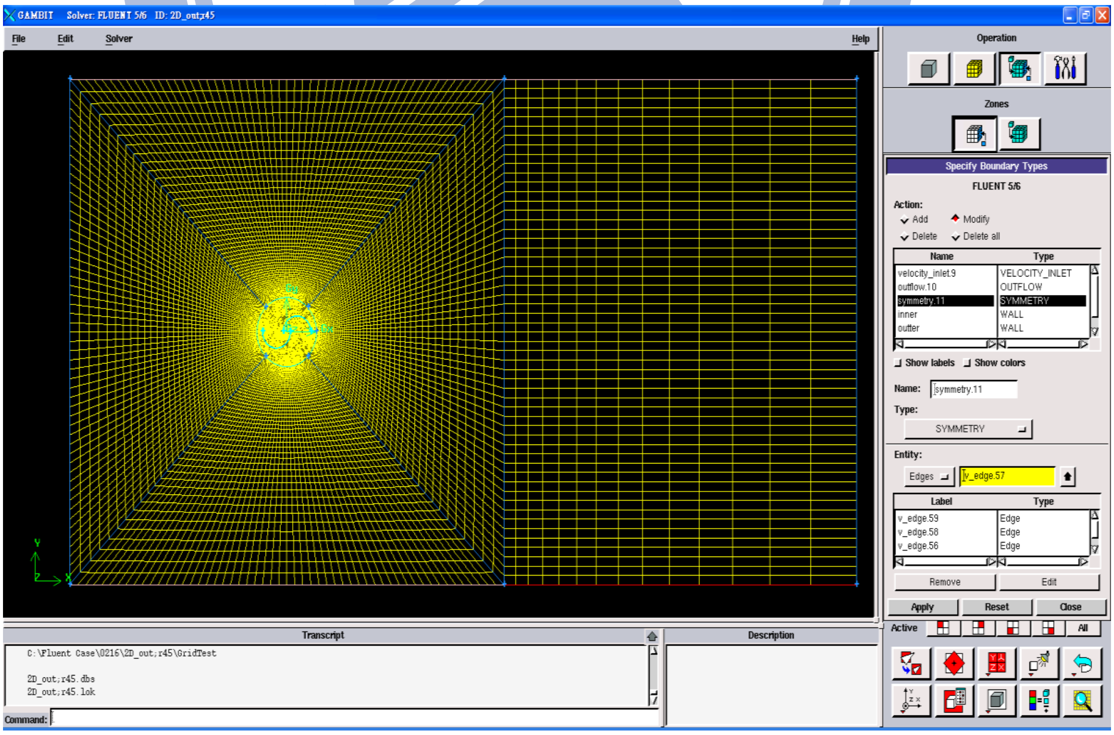

```
C:\Fluent Case\0216\2D_out;r45\GridTest

2D_out;r45.dbs
2D_out;r45.lok
```

Action: ◇ Add ◆ Modify ◇ Delete ◇ Delete all

Name	Type
velocity_inlet.9	VELOCITY_INLET
outflow.10	OUTFLOW
symmetry.11	SYMMETRY
inner	WALL
outter	WALL

Name: symmetry.11

Type: SYMMETRY

Entity: Edges v_edge.57

Label	Type
v_edge.59	Edge
v_edge.58	Edge
v_edge.56	Edge

Fig. 3.9 User Interface of Gambit

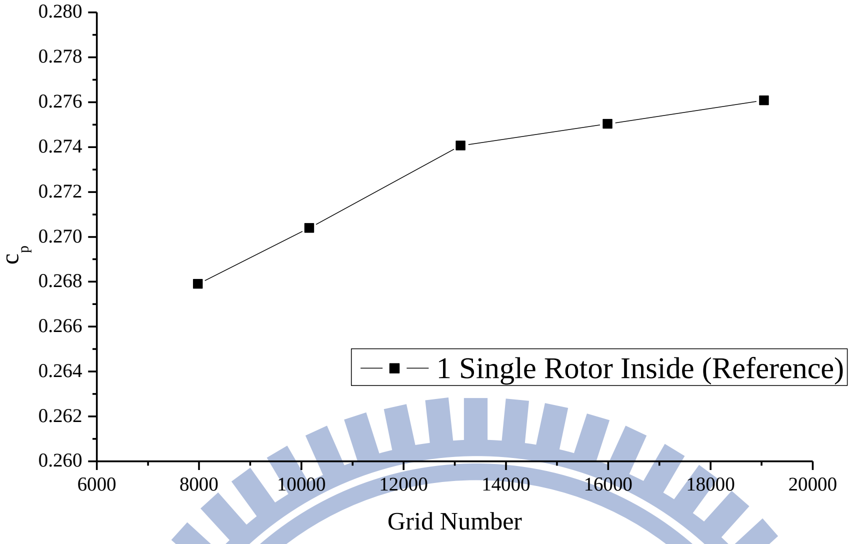
0.280
0.278
0.276
0.274
0.272
0.270
0.268
0.266
0.264
0.262
0.260
C_p
6000
8000
10000
12000
14000
16000
18000
20000
Grid Number
1 Single Rotor Inside (Reference)

(a)

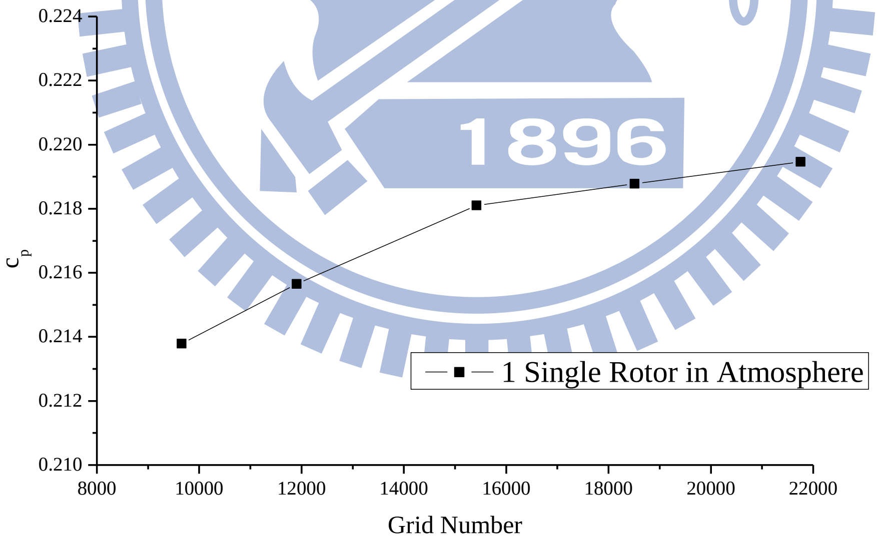
0.224
0.222
0.220
0.218
0.216
0.214
0.212
0.210
C_p
8000
10000
12000
14000
16000
18000
20000
22000
Grid Number
1 Single Rotor in Atmosphere

(b)

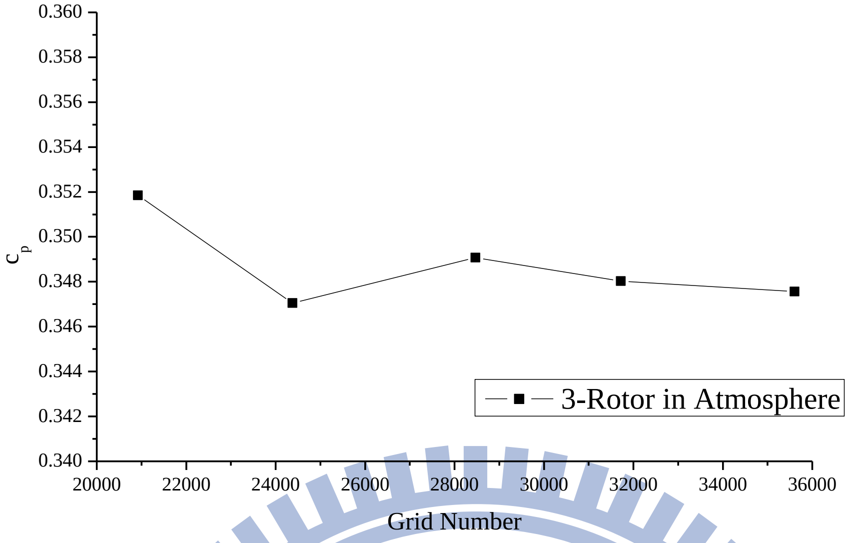

(c)

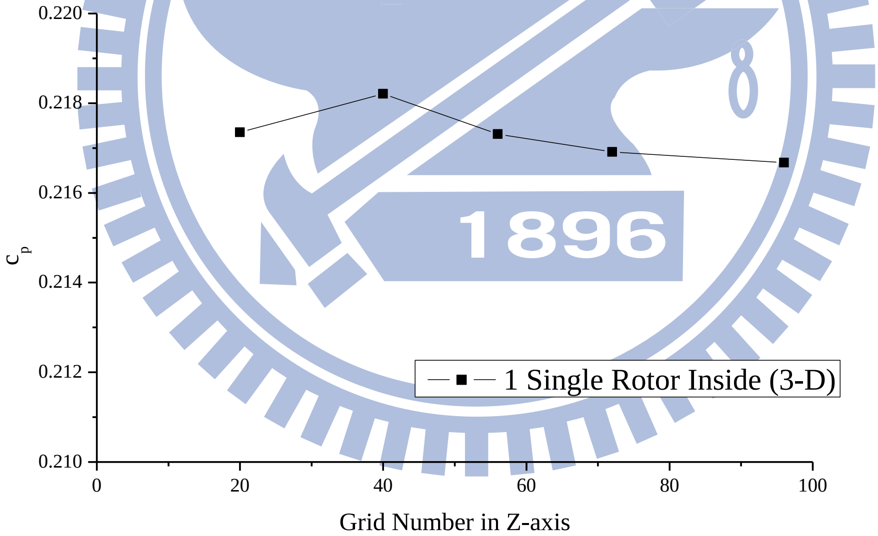

(d)

Fig. 3.10 Grid-independence tests: (a) 1 single rotor inside the wind tunnel (reference case); (b) 1 single rotor in atmosphere; (c) 3-rotor in atmosphere; (d) Grid number in Z-axis in 3-D domain

CHAPTER 4

RESULTS AND DISCUSSION

This study is divided into three parts. The research flow chart was already shown in **Fig. 1.6**. Firstly, the numerical investigation on performance of a single Savonius wind rotor is carried out and demonstrated in Section 4.1. Two conditions, a single Savonius wind rotor inside the wind tunnel corresponding to the reference case and a single Savonius wind rotor in atmosphere, are analyzed respectively. Secondly, a parallel matrix system, which includes three Savonius wind rotors rotating with the same angular speed, is demonstrated in Section 4.2. And the performance comparison between a single rotor and three-rotor connected in parallel is made. Furthermore, the influence of wind direction change on the parallel system is also studied. Finally, comparisons with other researches, such as improvements by adding windshields or twisted wind rotor systems, are given in Section 4.3.

4.1 A Single Savonius Wind Rotor

This topic consists of two categories, a single Savonius wind rotor inside the wind tunnel and a single Savonius wind rotor in atmosphere. The geometries are illustrated in **Figs. 3.1** and **3.2** and the corresponding information, such as the geometric data of the single Savonius wind rotor and the dimensions of the simulation domains are summarized in **Tables 3.1** and **3.2**.

4.1.1 A Single Savonius Wind Rotor inside the Wind Tunnel (Reference Case)

The reference case simulated in this work adopts the experimental one by

Blackwell et al. [4], who investigated the performances of fifteen configurations of Savonius wind rotors tested in a low speed wind tunnel. The Savonius wind rotor, with a predetermined load provided by an air motor, was allowed to rotate in a steady wind speed 7 or 14 m/s. When a steady rotation was achieved, a data was taken. After that, the load was changed slightly, causing a new rotational speed to get another data. By repeating these steps, the functions between c_p and tip-speed ratio in fixed wind speed were plotted. The experimental results in wind speeds of 7m/s and 14m/s are shown in **Fig. 4.1**. However, the turbine load is not considered in simulations, so the free spinning wind rotor cannot be fully simulated. The method in simulations is to specify constant rotational speeds and change the parameters to reveal freely moving wind rotor blades in experiments. The comparison between the predicted results and experimental measurements is given in this section.

The two and three dimensional simulations are carried out with the wind speeds of 7 and 14m/s and the tip speed ratios ranged from 0.4 to 1.2. 2-D model uses a grid number of 13115 and 3-D uses 741524, respectively. The parameters used are summarized in **Table 4.1**.

Table 4.1 Parameters for a single Savonius wind rotor inside the wind tunnel (Reference case)

Wind Speed	7 m/s and 14 m/s
Tip-Speed Ratio	0.4 ~ 1.2
Simulation Domain	2-D (11.9m × 4.6m)
	3-D (11.9m × 4.6m × 2m)

To observe the flow field, α is firstly defined as the angle of rotating wind blade relative to the initial angle and illustrated in **Fig. 4.2**. The description of flow field in 2-D simulation is given for demonstrating the fundamental phenomenon. The resultant torque curve of one single Savonius wind rotor with wind speed 7 m/s and tip-speed ratio 0.9 in a rotation (360°) is shown in **Fig. 4.3**. As shown in this figure, the maximal torque happens at α=10° and the minimal is at α=110°. The static pressure fields and velocity vector distributions around the single Savonus wind rotor at the two positions are demonstrated in **Figs. 4.4** and **4.5**, respectively. In **Fig. 4.4**, it shows that the pressure difference between the front and back sides of the retuning blade at α=110° is apparently higher than that at α=10°. A large vortex is generated around the tip at the low-pressure region behind the blade as shown in **Fig 4.5 (b)**. This effect would produce a negative torque and thus causes a lower torque. On the other hand, as shown in **Fig 4.5 (a)** at α=10°, the pressure difference between the front and back sides of the retuning blade is smaller, and the generated vortices are also smaller. Therefore, the negative torque is decreased, causing a higher torque.

Static pressure field and velocity vector distribution at a cross section at z = 1m (see Sec. 3.1) in 3-D simulations with tip-speed ratio 0.9 at α=10° and 110° are shown in **Figs. 4.6** and **4.7**, respectively. Comparing these two figures with **Figs. 4.4 and 4.5**, the phenomena in 3-D simulation are quite similar to those in 2-D one, only the pressure values are apparently lower than those in 2-D simulation due to the existence of one more dimension in 3-D simulation. When the wind hits blades, as shown in **Fig. 4.8**, the velocity vector distribution at y = 0, the air close to the top and bottom of the wind rotor will escape upwardly and downwardly, leading to a decrease of pressure around the wind rotor.

The performance comparisons between 2-D and 3-D predictions and with the corresponding experimental data are shown in **Fig. 4.9**. Considering the experimental measurements, the error bars on all the experimental data are fixed at ±20% of the measured value. Such value is proposed by Howell et al. [6], who also applied Fluent to compare the performances of a single VAWT by using 2-D and 3-D predictions with measurements. In **Fig. 4.9**, it clearly shows that the 3-D simulation is more suitable than the 2-D one in dealing with this problem. It is resulted from the effect mentioned above that the air close to the top and bottom of the wind rotor escape upwardly and downwardly. Such effect decreases the energy gained from wind and thus causes a lower performance. Moreover, the influence of frictions by end plates would lower the performance, too. For these reasons, the 3-D simulation is more suitable than the 2-D one, which cannot consider these effects.

The 2-D and 3-D predictions of a single Savonius wind rotor inside the wind tunnel in wind speeds of 7m/s and 14 m/s are shown in **Fig. 4.10**. In 2-D simulations, the maximum of c_p is 0.276 at wind speed 7 m/s and 0.278 at 14 m/s, whereas in 3-D simulations, the maximum of c_p is 0.222 at 7 m/s and 0.225 in 14 m/s. It also can be seen that in both 2-D and 3-D simulations, the c_p in wind speed 14 m/s are slightly higher than that in 7 m/s at the same tip-speed ratio. It is because the Reynolds number around the blades increases with wind speed, causing a delayed separation; see **Fig. 4.11,** the velocity vector distribution at z = 1m. Therefore, the drags on the advancing blades decrease and then cause a higher c_p.

4.1.2 A Single Savonius Wind Rotor in Atmosphere

To simulate a single Savonius wind rotor in atmosphere, its domain even with an application of symmetry is expected to be bigger than the one inside the wind tunnel. 2-D model uses a grid number of 15423, whereas 3-D model uses

886676. The parameters used are summarized in **Table 4.2** .

Table 4.2 Parameters for a single Savonius wind rotor in atmosphere

Wind Speed (m/s)	7 and 14
Tip-Speed Ratio	0.4 ~ 1.2
Simulation Domain	2-D (14.5m × 8m)
	3-D (14.5m × 8m × 2m)

Figure 4.12 shows the torque curve of one single Savonius wind rotor in atmosphere with wind speed 7 m/s and tip-speed ratio 0.9 in a rotation. In this figure, the maximal torque happens at α=10° and the minimum is at α=110°. The static pressure field and velocity vector distribution in 2-D simulation around the single wind rotor at the above two positions are shown in **Figs. 4.13** and **4.14**, respectively. The results show that both the maximum and minimum of torque are happened at the same position inside the wind tunnel, and the differences in pressure field and velocity vector distribution between the two conditions are unapparent.

Static pressure field and velocity vector distribution at a cross section of z = 1m in 3-D simulations with tip-speed ratio 0.9 at α=10° and 110° are shown in **Figs. 4.15** and **4.16**, respectively. Comparing these two figures with **Figs. 4.13** and **4.14**, the phenomena in 3-D simulation are similar to those in 2-D one and its pressure values are apparently lower than the ones in 2-D simulation. The reasons are the same as the situation inside the wind rotor as mentioned in Section 4.1.1.

The simulation results are shown in **Fig. 4.17**. In 2-D simulations, the results show that the maximum of c_p is 0.234 at wind speed 7 m/s and 0.236 at

14 m/s. In 3-D, the maximum of c_p is 0.182 at wind speed 7 m/s and 0.184 at 14 m/s. As shown in **Fig. 4.17**, the 2-D simulation results are apparently higher than 3-D ones, and the c_p slightly increases with wind speeds at the same tip speed ratio in both 2-D and 3-D simulation. The reasons are the same as the case of a single Savonius wind rotor inside the wind tunnel discussed in Section 4.1.1.

4.1.3 Performance Comparison between One Single Savonius Wind Rotor Inside the Wind Tunnel and the One in Atmosphere

Comparing the streamlines between one single wind rotor inside the wind tunnel and the one in atmosphere, the generated vortices around the one in atmosphere are slightly larger than those inside the wind tunnel (see **Figs. 4.18** and **4.19**). The difference is resulted from that the wind tunnel is not large enough to simulate the condition in atmosphere completely; therefore, rotating wind rotor would cause a higher pressure field (see **Figs. 4.4** and **4.13**), causing the curved streamlines. In **Figs. 4.18** and **4.19**, it can be seen that the wake length caused by flow separations in atmosphere is longer than that inside the wind tunnel both at $\alpha=10°$ and $\alpha=110°$. The larger wake flow field would make a higher difference in pressure between the front and back sides of the wind rotor, and then causes a higher drag. Therefore, the performance of one single Savonius wind rotor in atmosphere is lower than that inside the wind tunnel.

The performance comparisons between the one inside the wind tunnel and the one in atmosphere by 2-D and 3-D simulations are shown in **Figs. 4.20 (a)** and **(b)**. As shown in these two figures, the c_p of a single Savonius wind rotor in atmosphere is clearly lower than that inside the wind tunnel. The average difference is about 0.04 either in 2-D or 3-D simulation. The reasons have been mentioned above. Therefore, the simulations carried out in atmosphere are more practical.

4.2 The Parallel Matrix System with Three Savonius Wind Rotors

In this section, a parallel matrix system, which includes three Savonius wind rotors in atmosphere rotating with the same angular speed and the fixed distance, is studied. The domain geometry is shown in **Fig. 3.3** and the corresponding information is also summarized in **Tables 3.1** and **3.2**. The 2-D simulation standing for a perfect condition is studied in advance to observe the preliminary phenomena due to less computing time in 3-D simulation. After that, the 3-D simulation representing the actual situations is carried out. The parameters used for this case are summarized in **Table 4.3**.

Table 4.3 Parameters for three-rotor in atmosphere

The Distance between the Two Centers of Savonius Wind Rotors	1.2m
Wind Speed	7 m/s and 14 m/s
Phase Angle Difference	0°, 45°, 90° and 135°
Tip-Speed Ratio	0.4 ~ 1.7
Simulation Domain	2-D (14.5m × 10m)
	3-D (14.5m × 10m × 2m)

4.2.1 Three Savonius Wind Rotors in 2-D Simulation

The 2-D simulations with a grid number of 28469 are carried out in wind speeds of 7m/s and 14m/s and tip-speed ratios of 0.4 to 1.7 by using the 2-D domain. The parameters of phase angle differences 0°, 45°, 90° and 135° are selected because one period of the torque of a two-bladed Savonius wind rotor is 180°.

Fig. 4.21 shows the torque curves of the three Savonius wind rotors with phase angle difference 90°, wind speed 7 m/s at tip-speed ratio 0.9 in a rotation. The torque of a single Savonius wind rotor is also provided. As shown in this figure, all the three Savonius wind rotors in the parallel matrix system have apparently higher performances than that of a single Savonius wind rotor. It also can be observed that the torque of the middle Savonius wind rotor gets the best promotion. The reason is that the flow field around the middle wind rotor is influenced by both the top and bottom ones, so the flow fluctuation effect on this wind rotor is higher than the other two.

As shown in **Fig. 4.21**, the maximal torque in the middle wind rotor happen at α=40° and the minimum is at α=120°. Then, static pressure field and velocity vector distribution around three Savonus wind rotors at the above two positions are given in **Figs. 4.22** and **4.23**, respectively. At α=40°, the pressure difference between the front and the back sides of the advancing blade of the middle wind rotor make a positive torque, and the influence of the bottom one causes the fluid flowing to the region behind the retuning blade to decrease the pressure difference, and thus lower the drag forcing on the retuning blade. Therefore, an apparently higher torque is produced. At α=120°, the pressure difference in the retuning blade would produce a drag and thus causes a lower torque. However, the influence of the top one makes the fluid flowing to the region behind the retuning blade and then reduces the vortex behind the blade; and the bottom one affects the fluid flowing to the region behind the advancing blade to increase the positive torque. Therefore, the minimal torque is increased and is higher than those of the other two. As a result, the interaction between wind rotors would increase the positive torque and decrease the negative torque, and then produce a higher the performance.

The 2-D simulation results are shown in **Fig. 4.24**, and the comparison with a single Savonius wind rotor in atmosphere is also given. The resultant maximums of c_p in these conditions are listed in the flowing table.

Table 4.4 Comparisons of the maximums of c_p between a single rotor and three-rotor in 2-D simulations

	Wind Speed (m/s)	Phase Angle Difference (°)	Maximum of c_p
Three-rotor system	7	0	0.435
		45	0.466
		90	0.479
		135	0.419
	14	0	0.446
		45	0.467
		90	0.473
		135	0.421
A Single Rotor	7 m/s		0.234
	14 m/s		0.236

As shown in the above table, the best phase angle difference in such system is 90° and the poorest one is 135°. The suitability of phase angle difference for more energy gained from wind is based on the shape of the two semicircular blades of these Savonius wind rotors. However, even the c_p with phase angle difference 135° is the worst one, it is still 1.79 times of that by a single Savonius wind rotor. Phase angle difference 90° can obtain the best c_p, which is 2.05 times of that by a single Savonius wind rotor. The higher performance is resulted from the positive interaction between these Savonius wind rotors, and the flow fluctuation plays the major role in contributing to this effect. According to the research of Howell et al. [6], the fluctuation is caused by reasons, such as the potential disturbances around the rotating blades and the large vortex shedding due to the flow separation from the wind rotor's blade (see **Fig. 4.25**). The influence of the fluctuation velocity on the power output is explained by separating the inflow velocity into time average and fluctuation components as following:

$$\begin{aligned} W &= Cu^3 \\ &= C(\bar{u} + u')^3 \\ &= C\left(\bar{u}^3 + 3\bar{u}^2 \cdot u' + 3\bar{u} \cdot u'^2 + u'^3\right) \end{aligned}$$

$$\Rightarrow \ \overline{W} = C\bar{u}^3 \cdot \left[1 + 3\left(\frac{u'}{\bar{u}}\right)^2\right]$$

where C represents the constant to u^3 with all the other factors fixed, and the over bar indicates time averaging. Therefore, it can be concluded that the time average power output will increase with the fluctuation of velocity.

This positive interaction by connecting three Savonius wind rotors in parallel may gain apparently the higher performance, but it might be sensitive to the direction of wind. Therefore, the influence of wind direction on the parallel system is studied now. The system with phase angle difference 90° are chosen with the wind velocity 7 m/s and tip-speed ratio 0.9. The angles of wind direction are 0°, ±15°, ±30° and ±45°. The results are shown in **Fig. 4.26,** and a comparison with a single Savonius wind rotor is given as well. In the figure, the change of wind direction will clearly affect and lower the c_p of the parallel matrix system at 0°. When $\theta = 45°$, its c_p stays almost the same as that of a single Savonius wind rotor; and when $\theta = -45°$, the c_p is even lower than that of a single one. **Figs. 4.27 (a)** and **(b)** shows the velocity vector distribution around the three Savonius wind rotors with a wind direction $\theta = -45°$ at $\alpha=0°$ and 90°, respectively. As shown in these two figures, the above mentioned effect that the pressure difference on the retuning blade is decreased by the effect of the lower wind rotor is reduced due to the changed arrangement relative to the wind direction. The lower wind rotor could not affect the fluid flowing to the region behind the retuning blade of the upper one to reduce the vortex. Therefore, a negative torque is increased and then causes a lower performance. It indicates that the parallel matrix system is strongly influenced by the change of wind direction, representing that one of the advantages in VAWTs is lost.

However, 2-D simulations representing perfect condition can not reveal the actual phenomena in reality. Therefore, 3-D simulations are carried out next.

4.2.2 Three Savonius Wind Rotors in 3-D Simulation

In this section, the 3-D simulations, whose domain is with a grid number of 1608769, are carried out with wind speeds of 7m/s and 14m/s and tip-speed ratio of 0.4 to 1.2. Phase angle difference 90° is selected due to its best performance obtained in 2-D simulations.

Static pressure field and velocity vector distribution at a cross section z = 1m in 3-D simulations with tip-speed ratio 0.9 at $\alpha=40°$ and 120° are shown in **Figs. 4.28** and **4.29**, respectively. Comparing these two figures with these in 2-D simulation, the 3-D flow field is similar to 2-D one and the phenomena are the same as the cases discussed in Section 4.2.1. However, it can be seen that the values of negative pressure are apparently lower than those in 2-D simulation. The reason will be discussed in the next section.

The 3-D simulation results and performance comparison with a single Savonius wind rotor in atmosphere are shown in **Fig. 4.30**. The corresponding maximal c_p are listed in **Table 4.5**.

Table 4.5 Comparisons of the maximum c_ps between a single rotor and three-rotor with phase angle difference 90° in 3-D simulation

	Wind Speed (m/s)	Max. c_p
Three-rotor (phase angle difference 90°)	7	0.266
	14	0.268
A single Rotor	7	0.182
	14	0.184

The results show that either in wind speed 7 or 14 m/s, the maximal c_p in the parallel matrix system is about 1.45 times of that by a single Savonius wind rotor.

4.2.3 Comparison between 2-D and 3-D Simulation Results

The performance comparisons between the two simulation situations, 2-D and 3-D, with wind speeds 7 m/s and 14 m/s are shown in **Figs. 4.31 (a)** and **(b)**, respectively. The solid line represents 3-D simulation results and the dash line represents 2-D's.

The power output can be derived from c_p as follows:

$$c_p = \frac{W}{\frac{1}{2}\rho A v^3}$$

$$\Rightarrow W = c_p \cdot \left(\frac{1}{2}\rho A v^3\right)$$

By using the above equation, the maximums of average power output of a Savonius wind rotor in the two conditions, the parallel matrix system with phase angle difference 90° and a single Savonius wind rotor, are calculated and the results are listed in **Table 4.6**.

Table 4.6 The maximums of average power output of a Savonius wind rotor in the two systems

condition	Simulation	Wind Speed (m/s)	Average Power output (W/per rotor)
Three-rotor system with phase angle difference 90°	2-D	7	90.53
		14	714.43
	3-D	7	50.25
		14	406.05
A Single Rotor	2-D	7	44.26
		14	356.79
	3-D	7	34.48
		14	278.16

From the above table, it can be seen that the difference between 2-D and 3-D simulation results is apparent. In the single Savonius wind rotor condition, the ratio of 2-D c_p to 3-D one is about 1.28; and in the parallel matrix system, the corresponding ratio is about 1.83. The reason is that the performance enhancement in the parallel matrix system depends on the positive interactions between wind rotors. As mentioned in Section 4.1.1, the air close to the top and bottom of the wind rotor will escape upwardly and downwardly and thus the energy gained from wind around the regions is reduced. This effect would be intensified when multiple Savonius wind rotors are connected in parallel. As shown in **Fig. 4.32**, the phenomenon of escaping fluid in the case of three single Savonius wind rotors is more apparent than that in the case of the single one. This effect would apparently lower the negative pressure behind the wind rotor (see **Fig. 4.28**) and then the influence of generated vortices to reduce the performance is intensified.

In summary, the fundamental phenomena could be observed from 2-D simulations in general and this way could also reduce the computing time substantially. But if the actual phenomena and performances in reality are expected to be found, 3-D simulations should be carried out necessarily.

4.3 Comparisons with Other Researches

In order to improve the performance of Savonius wind rotors, there are some methods existed in other researches. The most common methods are to change the shape of blade, such as the use of twisted blade geometry, and to put an obstacle to prevent the influence of wind on the returning blade. The comparisons between parallel matrix system and these methods are given in this section.

Altan et al. [8] experimentally investigated the method of adding windshields. In an optimal arrangement, the c_p is 2.375 times of that without windshield. Saha et al. [10] brought up that the two-bladed Savonius wind rotor system with two-stage and twisted blades can get the optimal arrangement and the performance is 1.72 times of one general two-bladed Savonius wind rotor’s. And the performance of parallel matrix system with three Savonius wind rotors in this research can obtain about 1.45 times of that in the single Savonius wind rotor system in 3-D simulations.

Comparing the three improvement methods, adding windshields can achieve the most promotion in c_p. But it still owns a restriction that the influence of wind direction change would be very severe. The second method, which changes the geometry of blade, is fair, and it would not be affected by the change of wind direction. However, the twisted blades, more difficult to manufacture, may need much higher cost than that of the general semicircular blades. Therefore, the parallel matrix system seems to be regarded as a compromising way that does not need to change the geometry of the shape and also can obtain good promotion of c_p. But it still has the restriction on wind directions, just like the method of adding windshields.

Therefore, comparisons in performance, extra cost and restriction of wind direction of the three methods are summarized as follows:

Performance:

Adding windshields > Using Twisted blades > Parallel matrix system

Extra cost:

Using Twisted blades > Adding windshields > Parallel matrix system

Restriction of wind direction:

Adding windshields > Parallel matrix system > Using Twisted blades

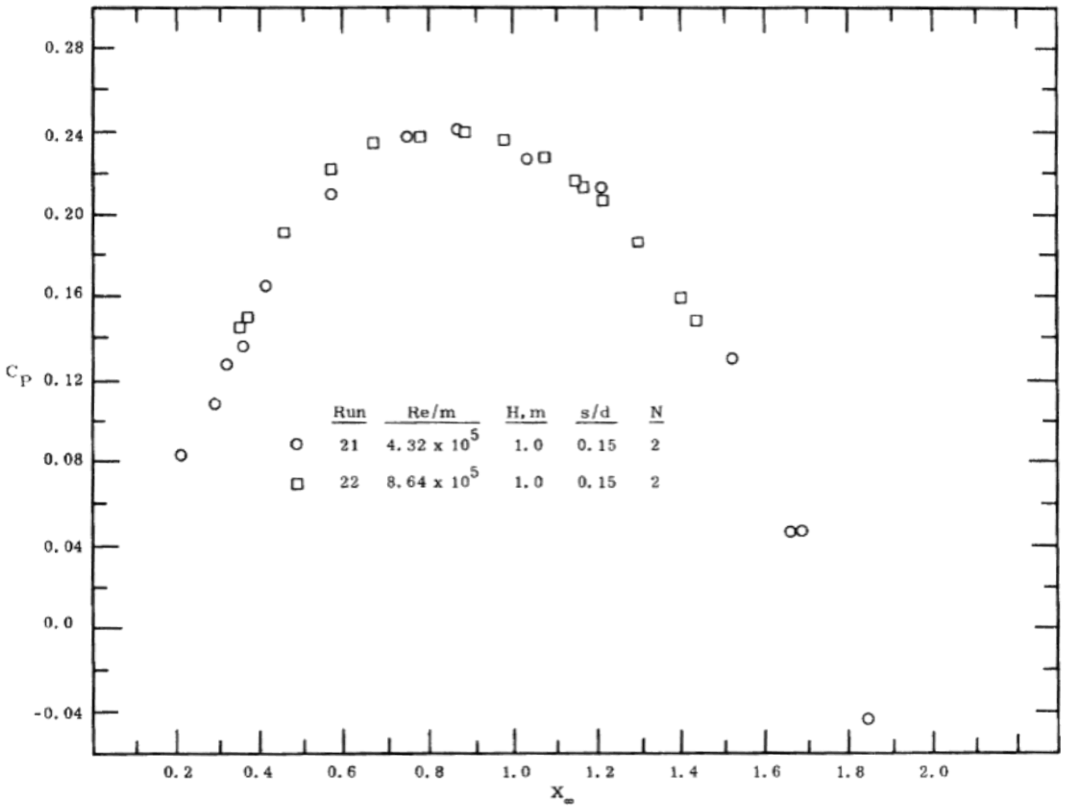

Fig. 4.1 The experimental results of a single Savonius wind rotor inside the wind tunnel (Reference case) [4]

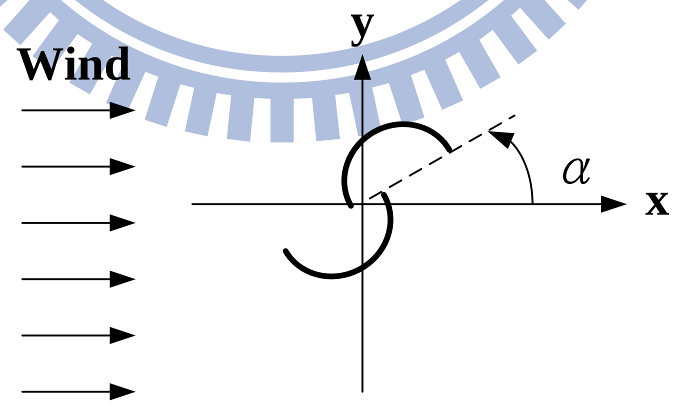

Fig. 4.2 The defined angle α of rotating wind blade relative to the initial angle

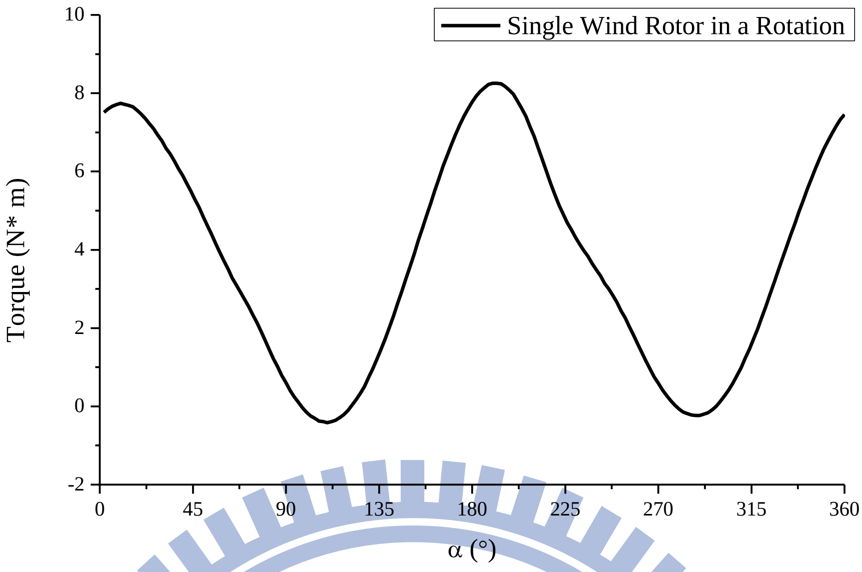

Fig 4.3 Torque curve of one single Savonius wind rotor inside the wind tunnel with wind speed 7 m/s and tip-speed ratio 0.9 in a rotation

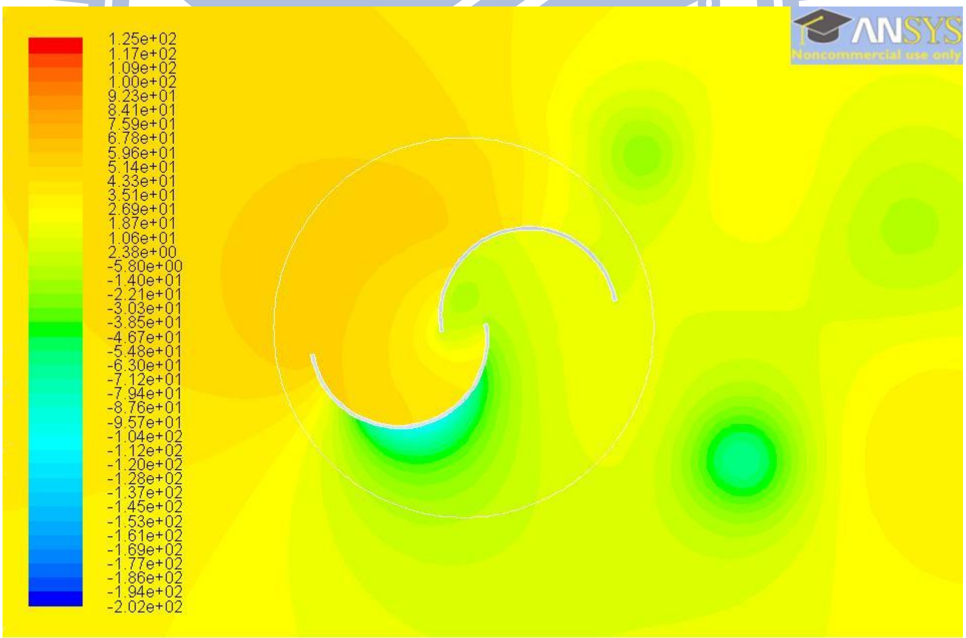

(a)

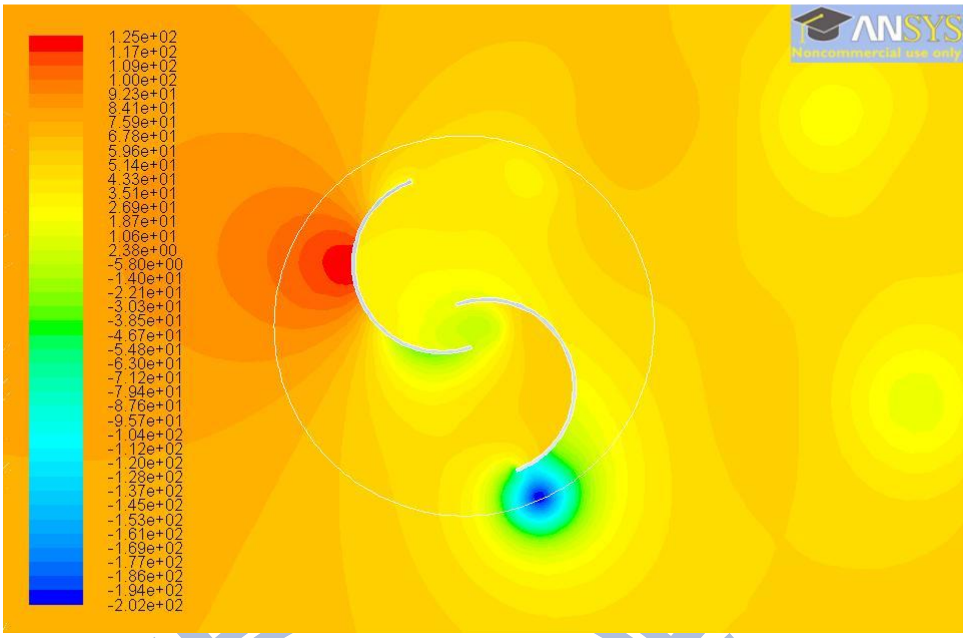

(b)

Fig. 4.4 Static pressure field around one single Savonius wind rotor inside the wind tunnel in 2-D simulation at: (a) α=10°; (b) α=110°

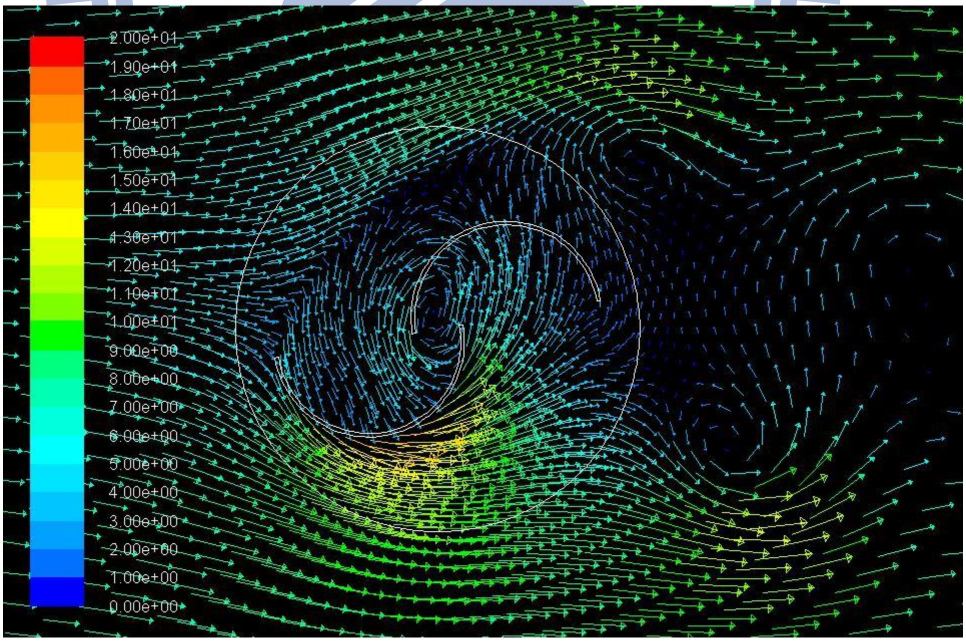

(a)

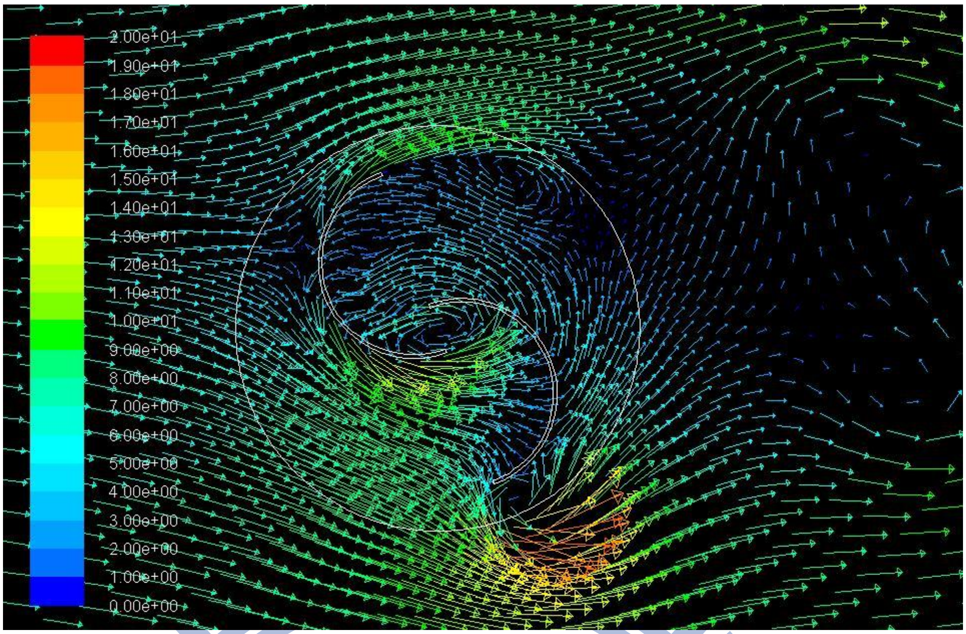

(b)

Fig. 4.5 Velocity vector distribution around one single Savonius wind rotor inside the wind tunnel in 2-D simulation at: (a) α=10°; (b) α=110°

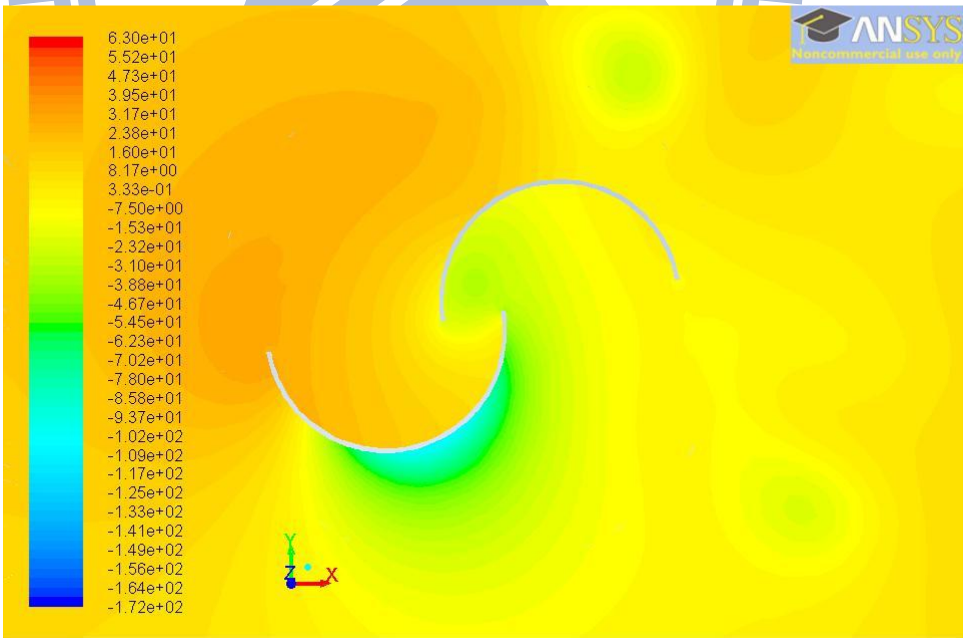

(a)

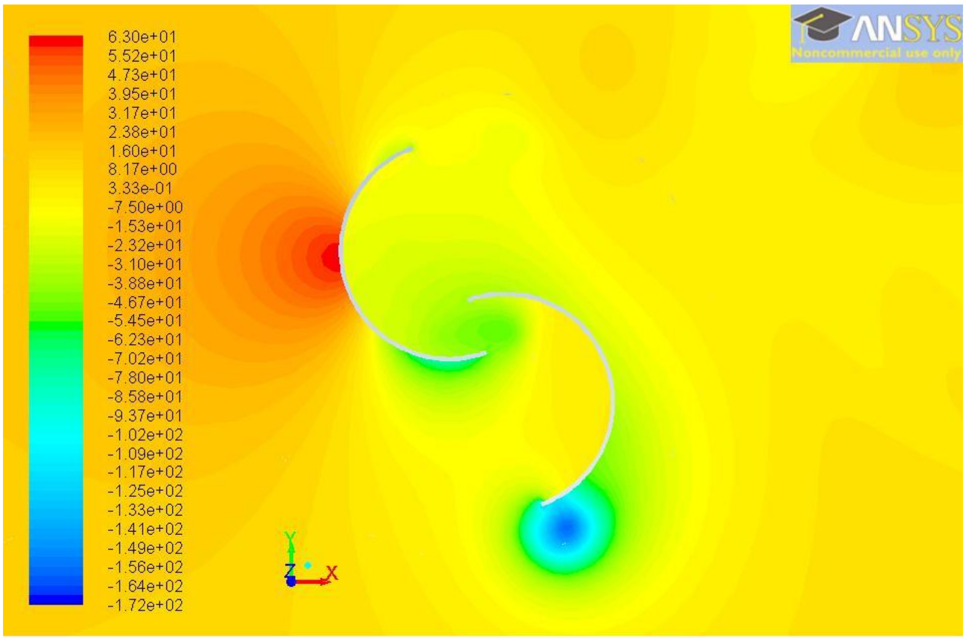

(b)

Fig. 4.6 Static pressure field around one single Savonius wind rotor inside the wind tunnel in 3-D simulation at z = 1m and: (a) α=10°; (b) α=110°

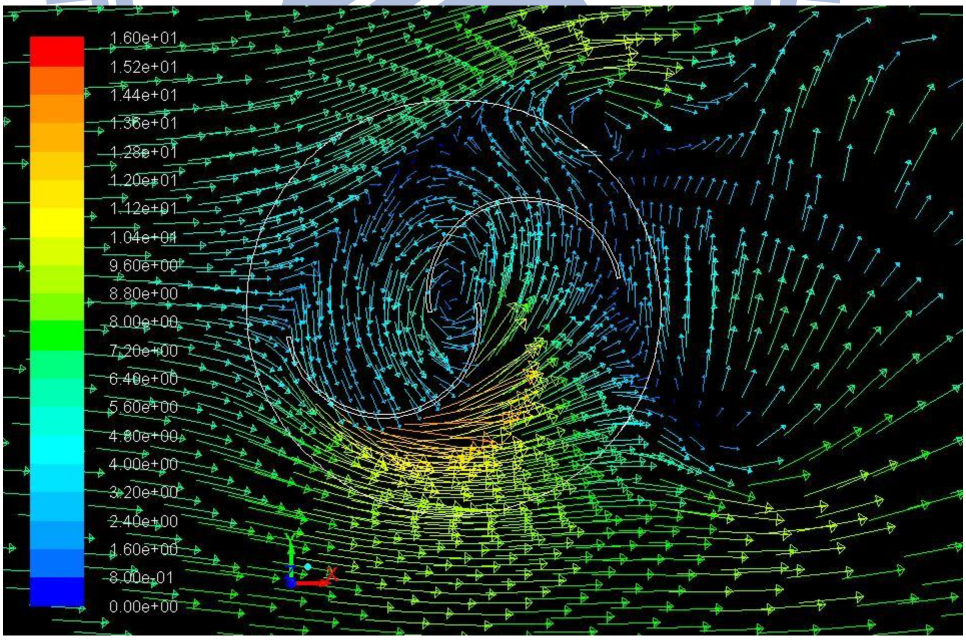

(a)

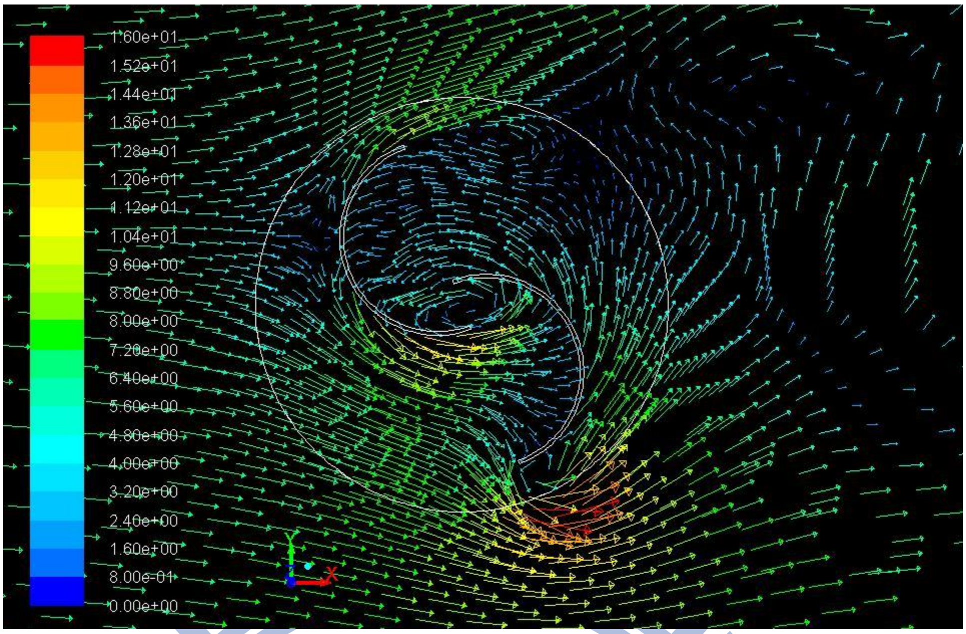

(b)

Fig. 4.7 Velocity vectors distribution around one single Savonius wind rotor inside the wind tunnel in 3-D simulation at z = 1m and: (a) α=10°; (b) α=110°

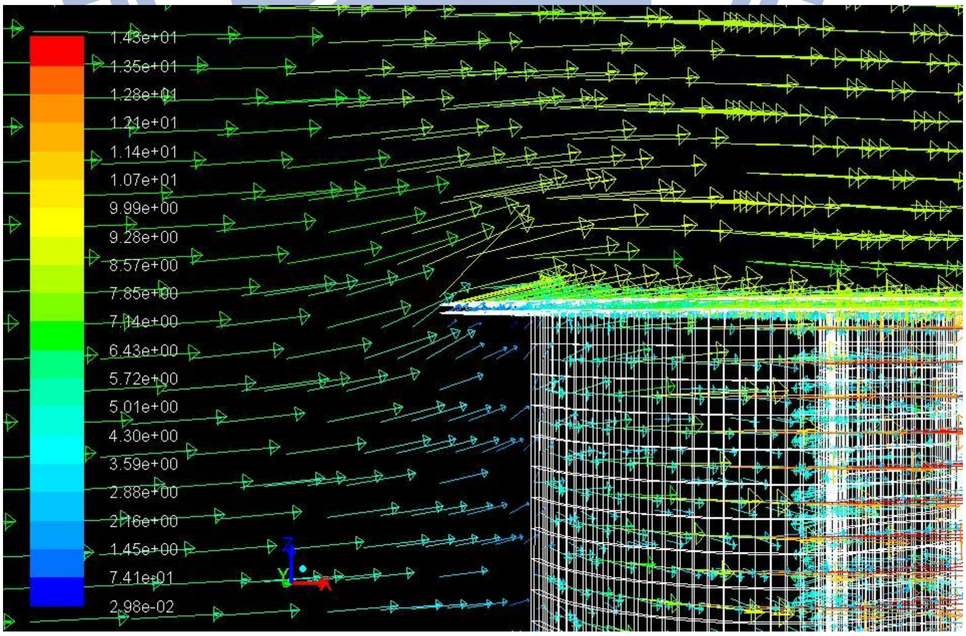

(a)

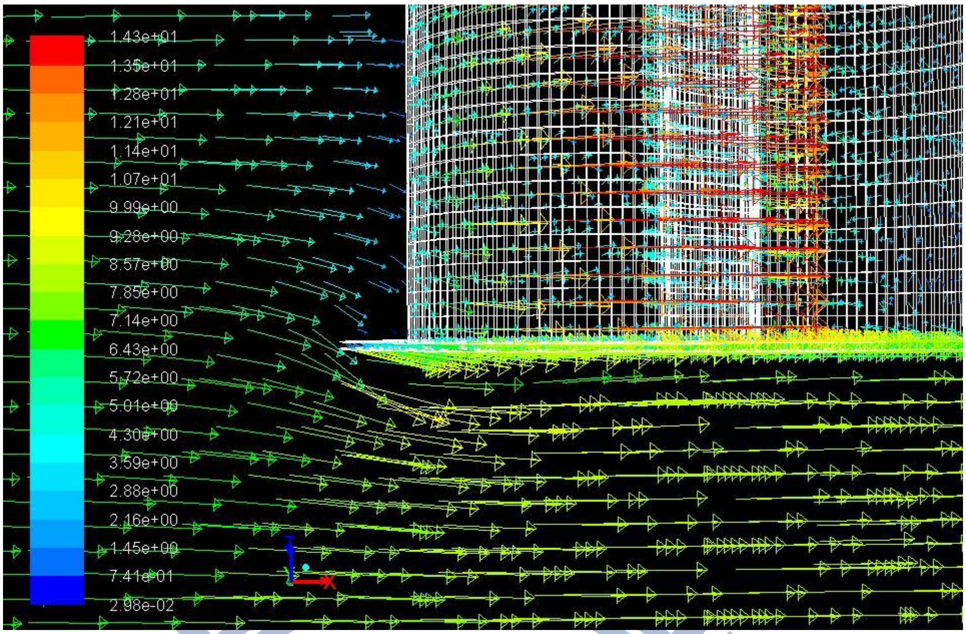

(b)

Fig. 4.8 Velocity vector distribution in 3-D simulation at y = 0 around: (a) the top end plate; (b) the bottom end plate

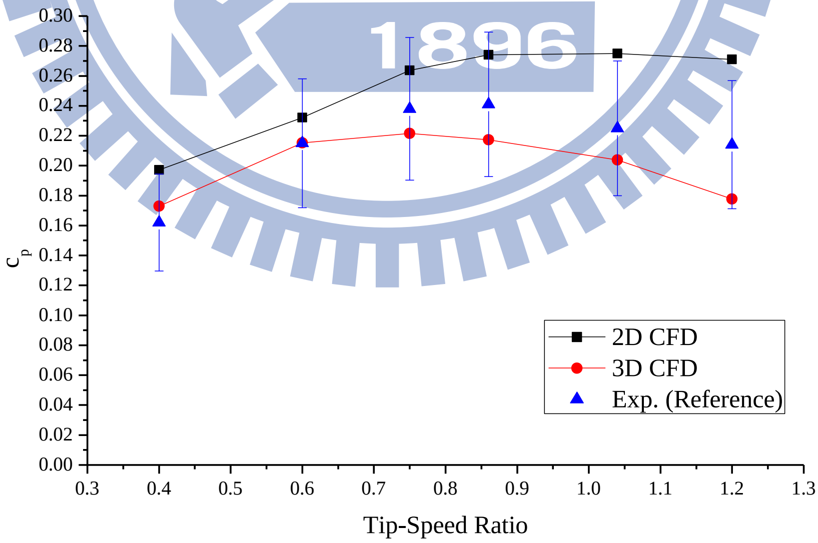

(a)

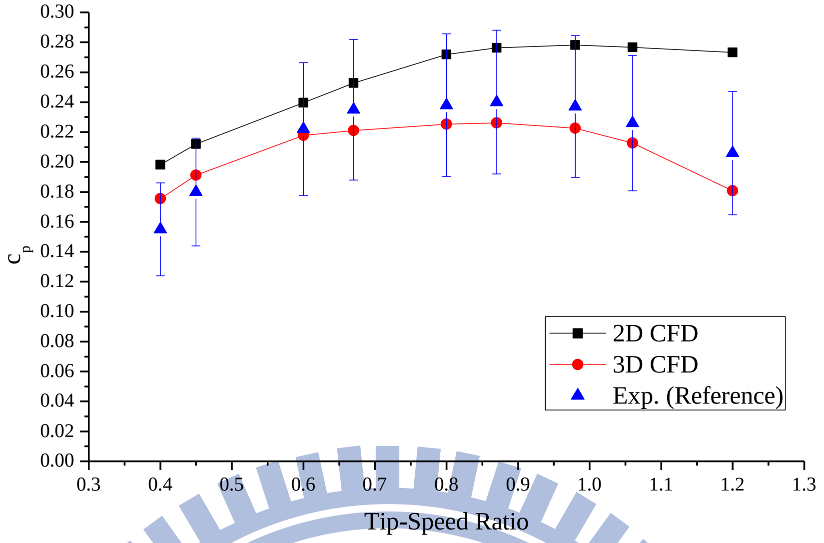

(b)

Fig. 4.9 A single Savonius wind rotor inside the wind tunnel comparing with experimental data in: (a) wind speed 7 m/s; (b) wind speed 14 m/s

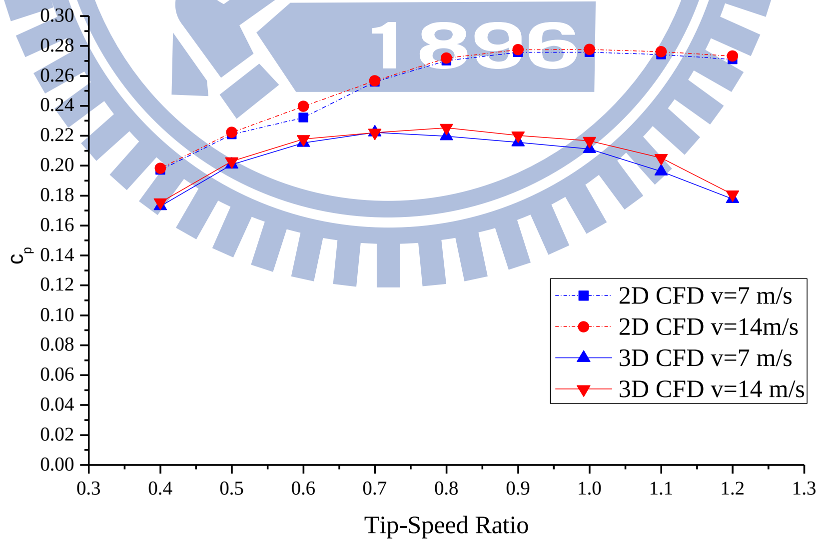

Fig. 4.10 The performance of a single Savonius rotor inside the wind tunnel

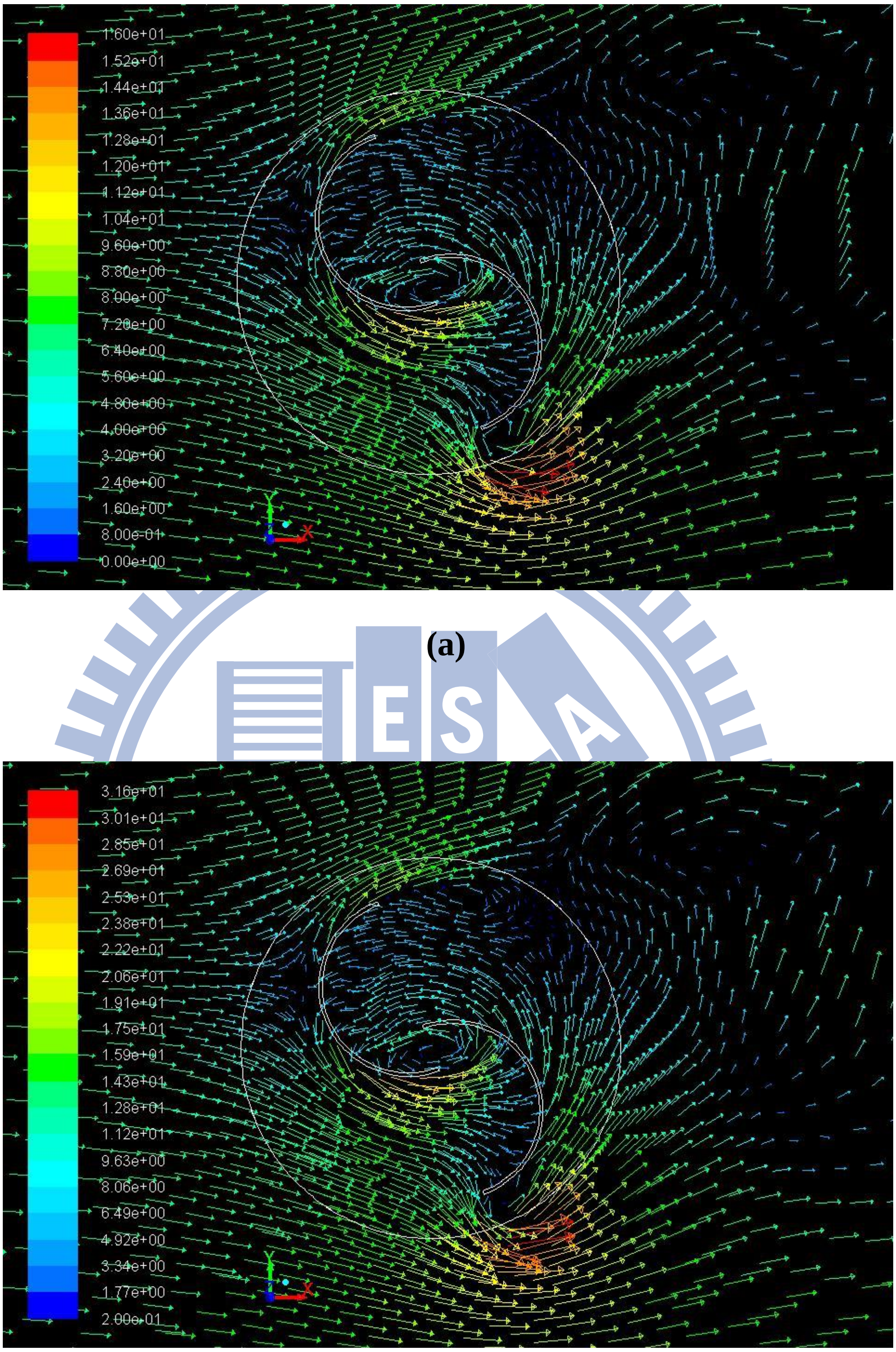

(a)

(b)

Fig. 4.11 Velocity vector distribution around one single Savonius wind rotor inside the wind tunnel at z=1m and α=110° in wind speed: (a) 7m/s; (b) 14m/s

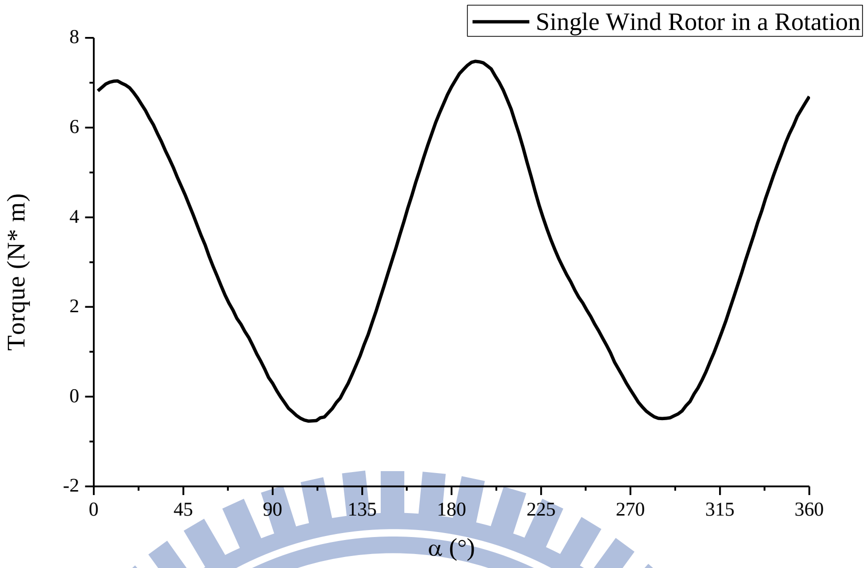

Fig 4.12 Torque curve of one single Savonius wind rotor in atmosphere with wind speed 7 m/s and tip-speed ratio 0.9 in a rotation

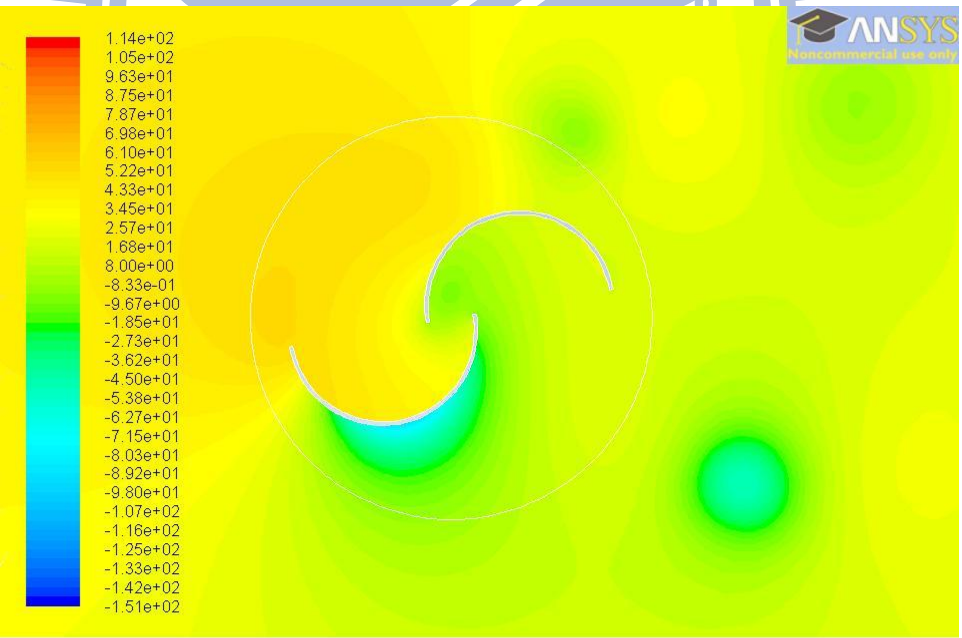

(a)

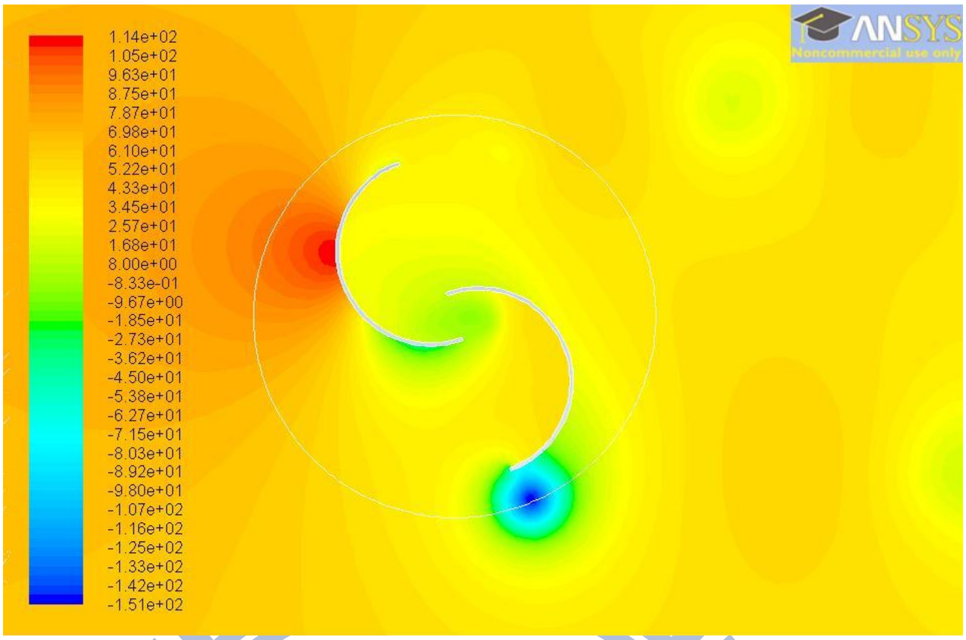

(b)

Fig. 4.13 Static pressure field around one single Savonius wind rotor in atmosphere in 2-D simulation at: (a) α=10°; (b) α=110°

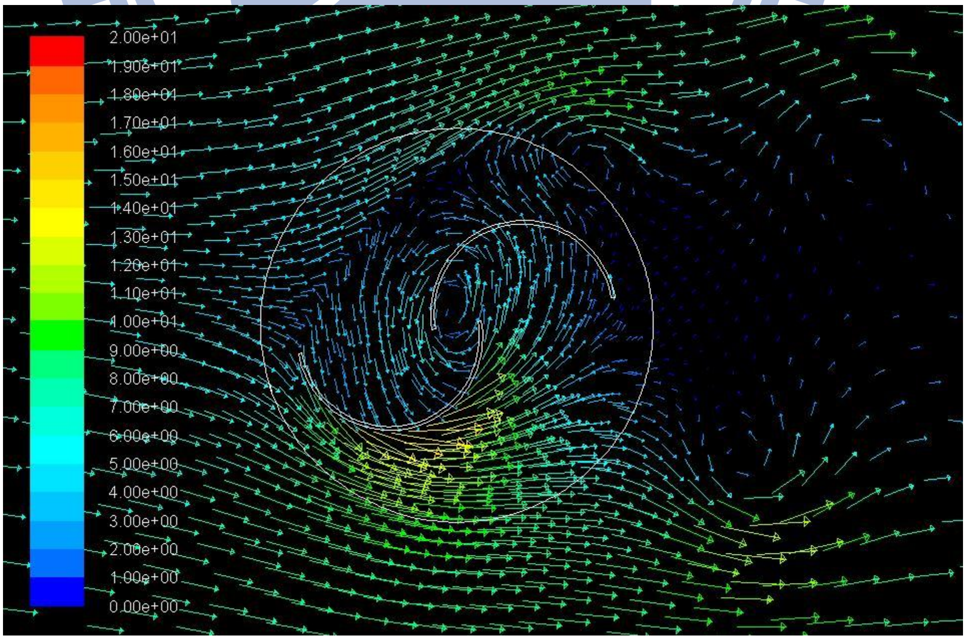

(a)

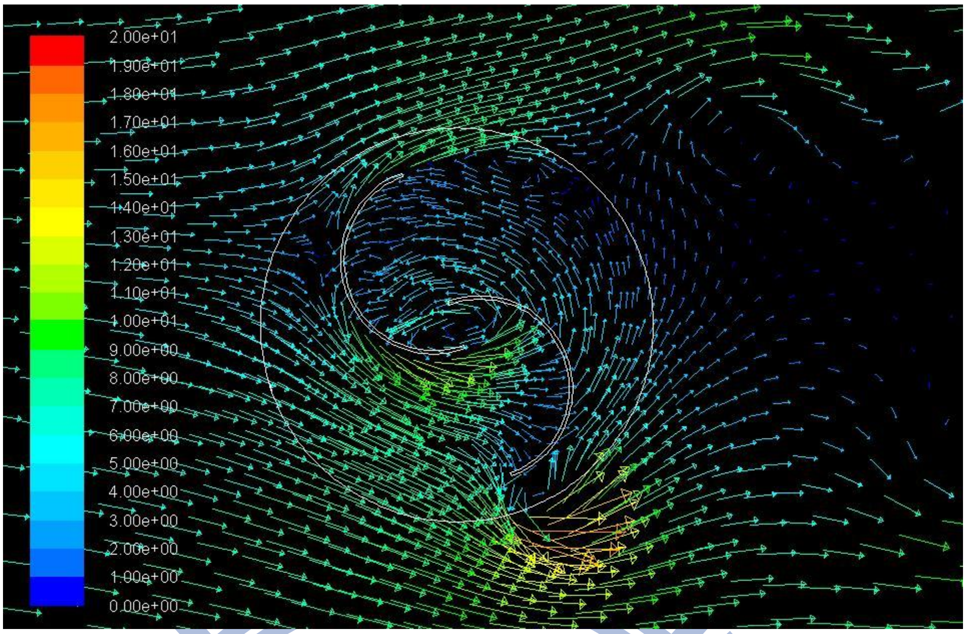

(b)

Fig. 4.14 Velocity vector distribution around one single Savonius wind rotor in atmosphere in 2-D simulation at: (a) α=10°; (b) α=110°

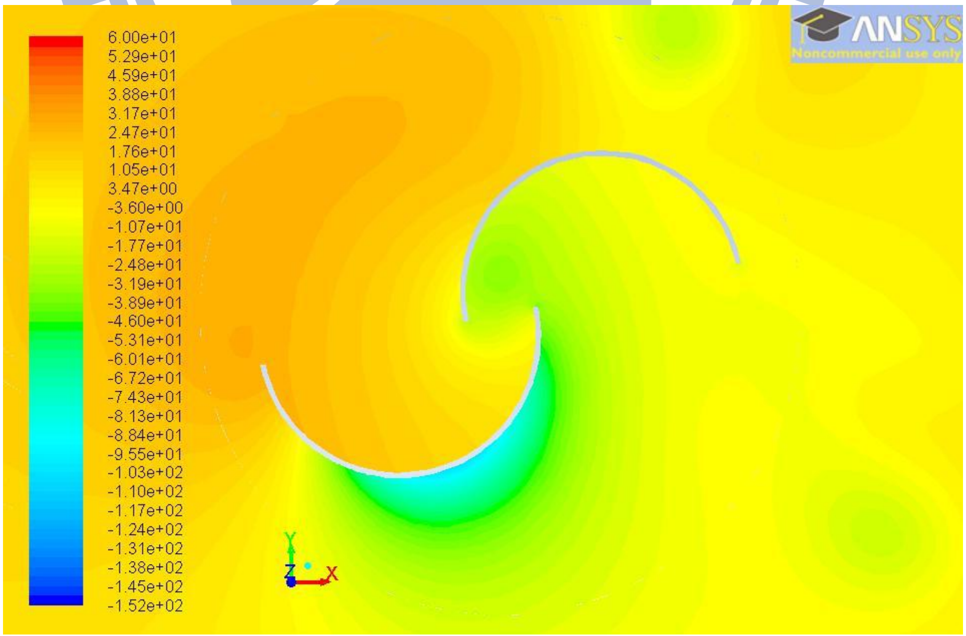

(a)

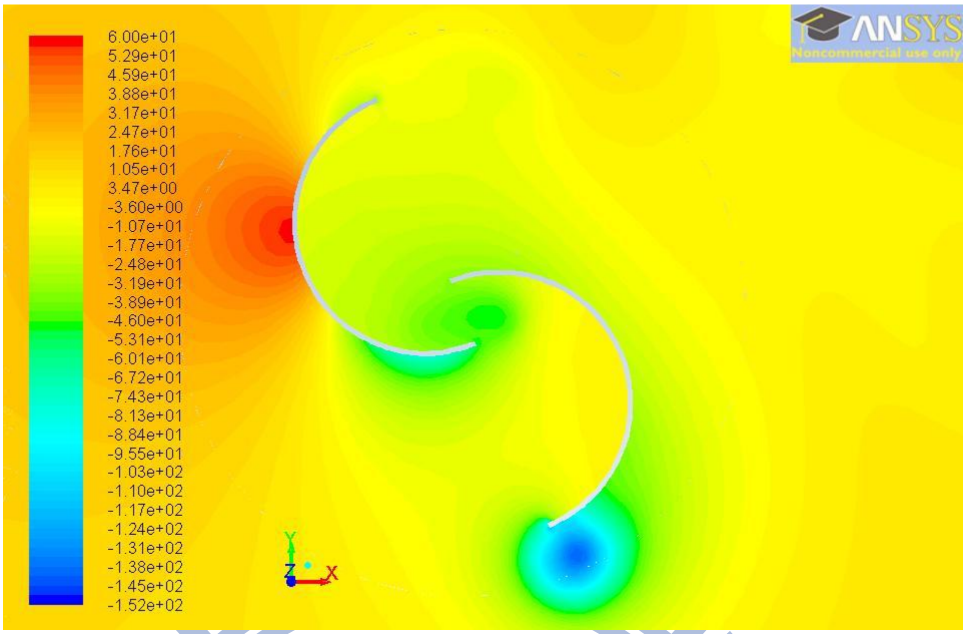

(b)

Fig. 4.15 Static pressure field around one single Savonius wind rotor in atmosphere in 3-D simulation at z=1m and: (a) α=10°; (b) α=110°

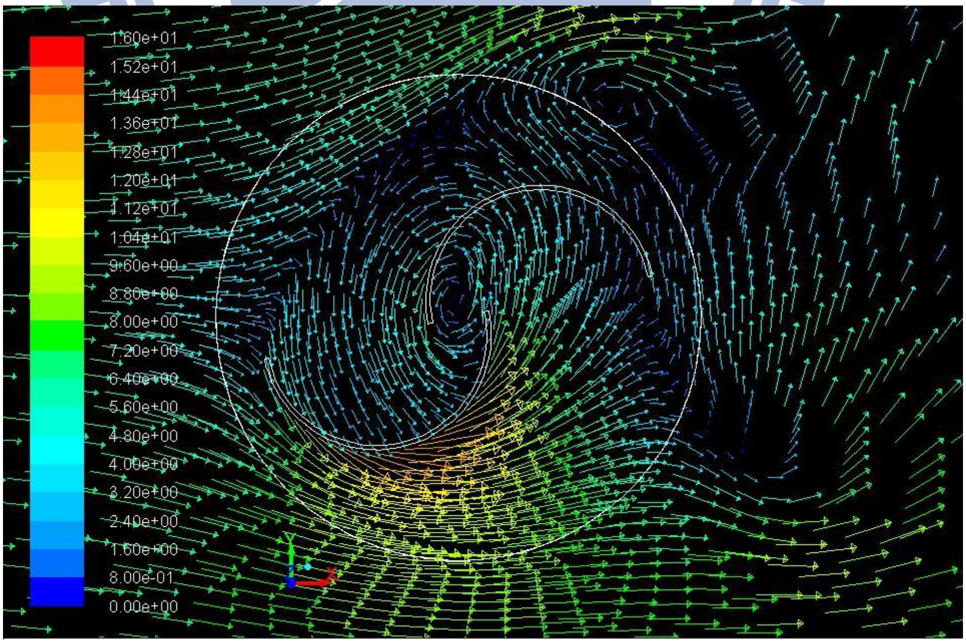

(a)

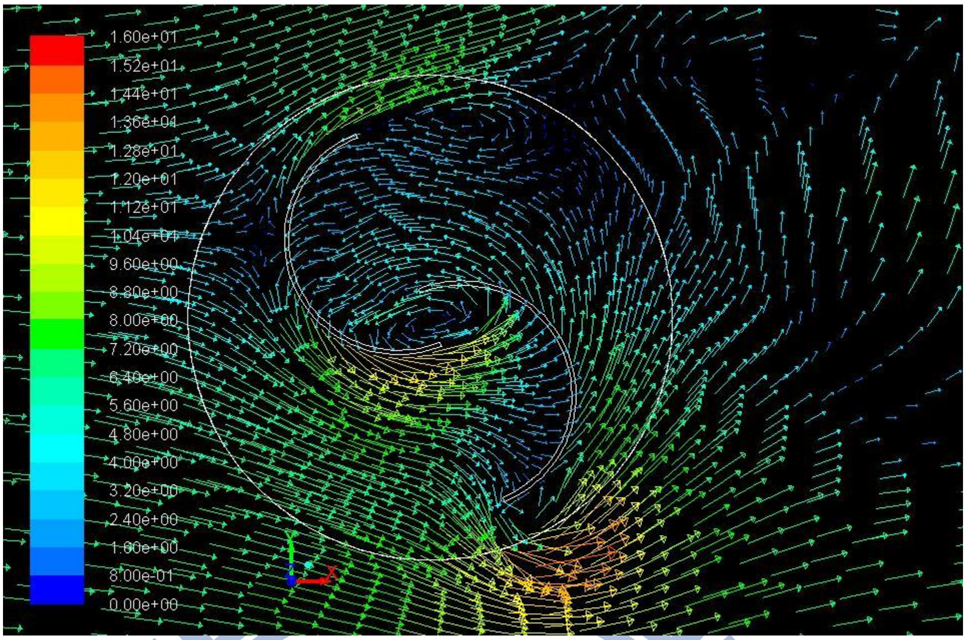

(b)

Fig. 4.16 Velocity vector distribution around one single Savonius wind rotor in atmosphere in 3-D simulation at z=1m and: (a) α=10°; (b) α=110°

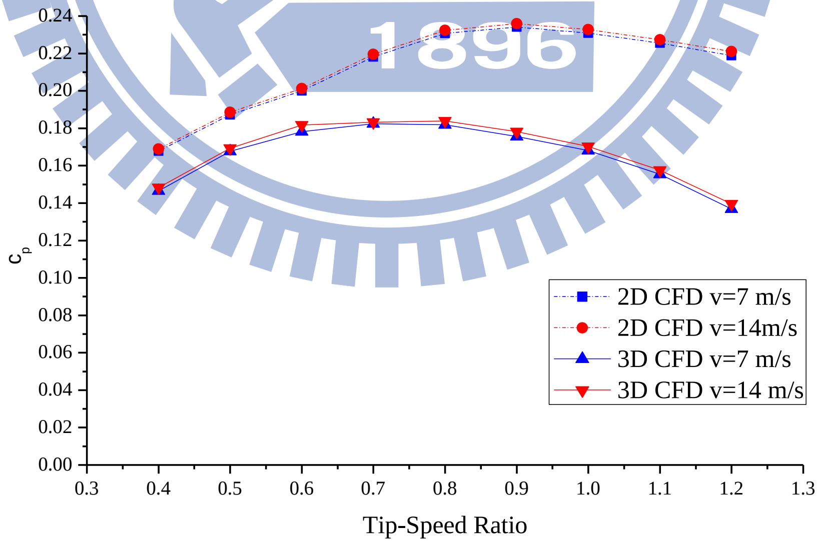

Fig. 4.17 The performance of a single Savonius wind rotor in atmosphere

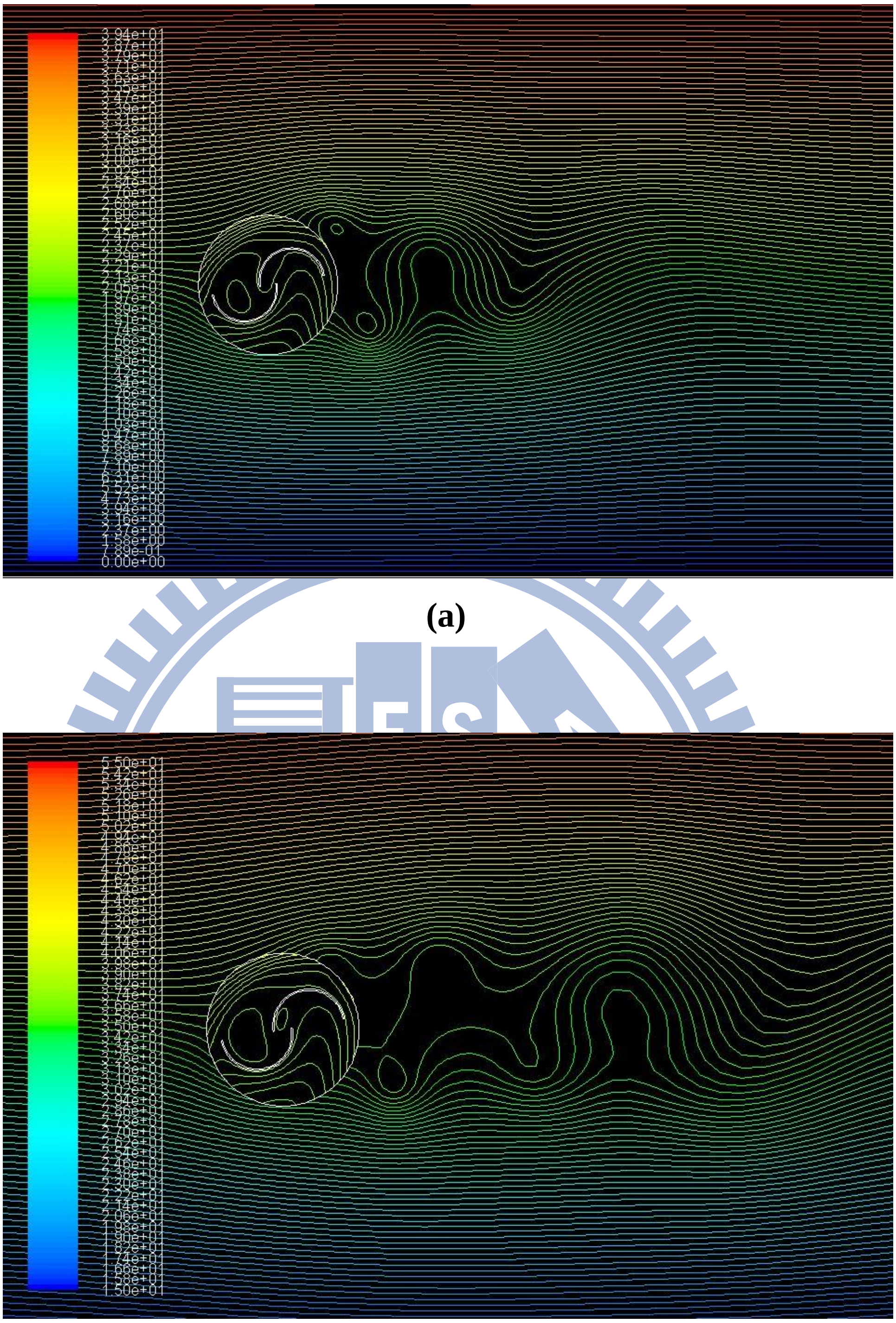

(a)

(b)

Fig. 4.18 Streamlines around one single Savonius wind rotor at α=10°: (a) inside the wind tunnel; (b) in atmosphere

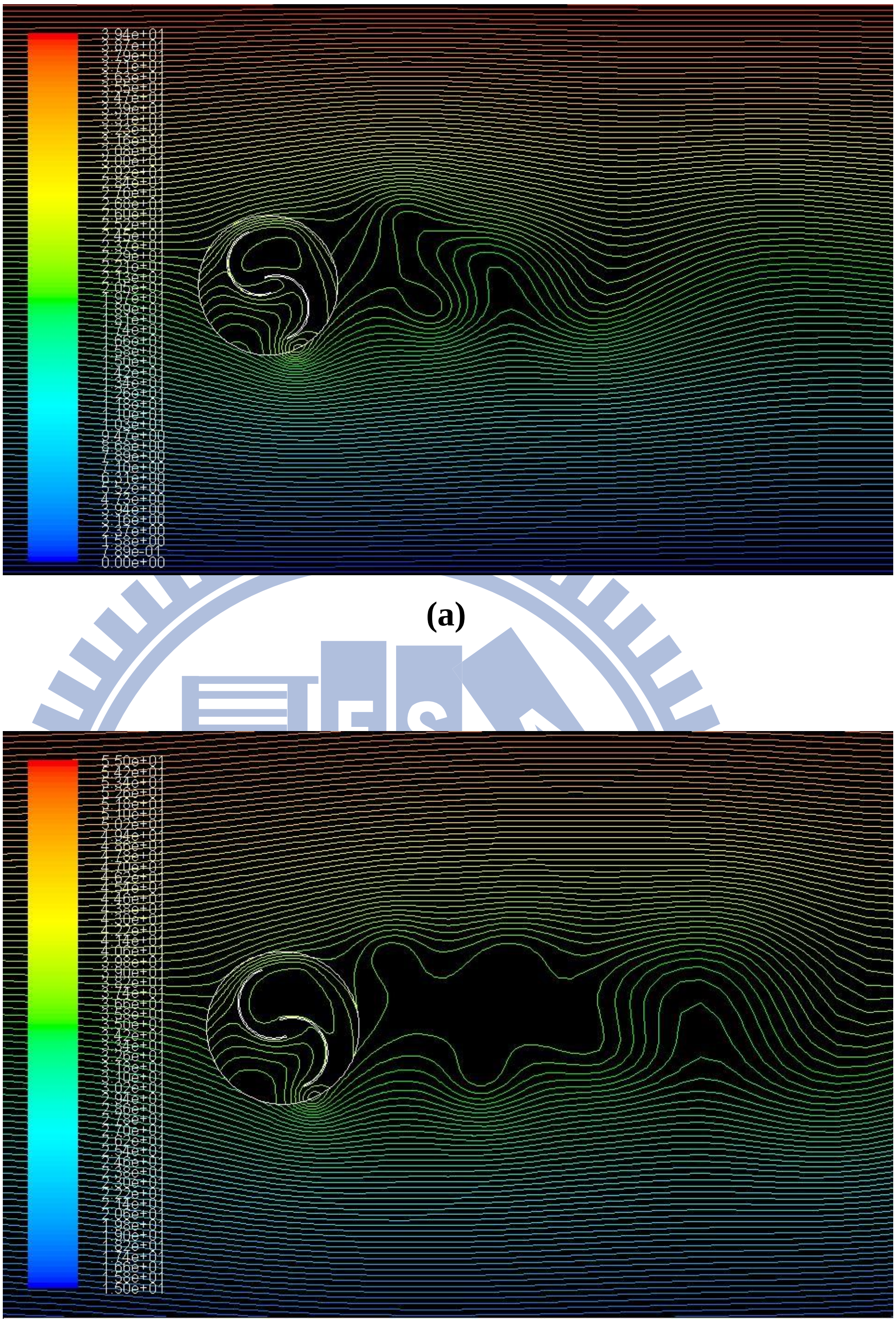

(a)

(b)

Fig. 4.19 Streamlines around one single Savonius wind rotor at α=110°: (a) inside the wind tunnel; (b) in atmosphere

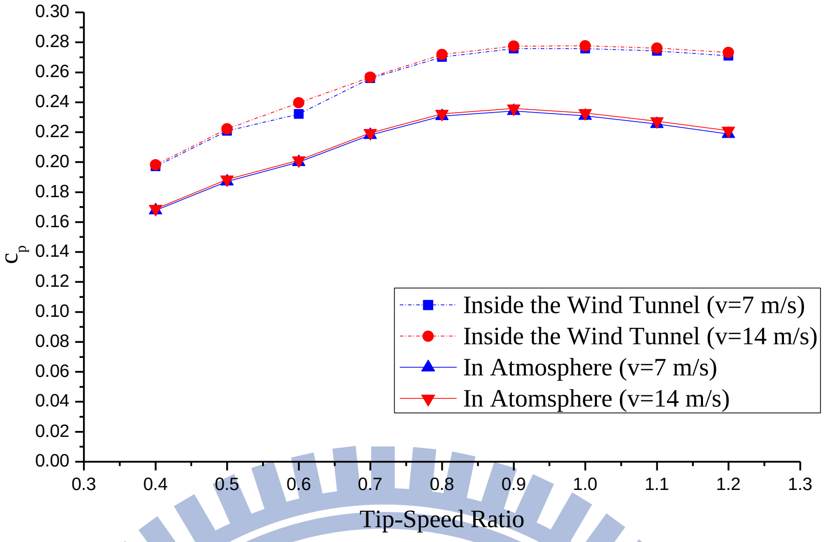

(a)

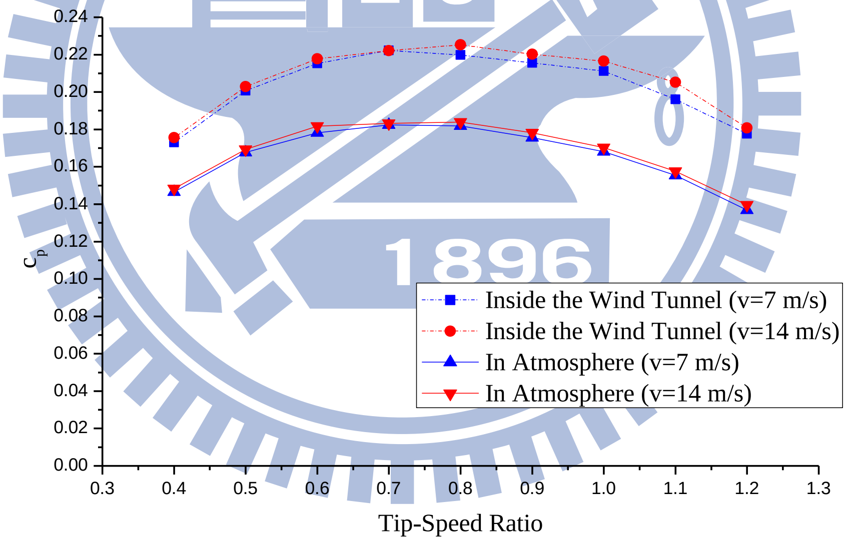

(b)

Fig. 4.20 Performance comparisons between one single Savonius wind rotor inside the wind tunnel and one in atmosphere in: (a) 2-D simulation; (b) 3-D simulation

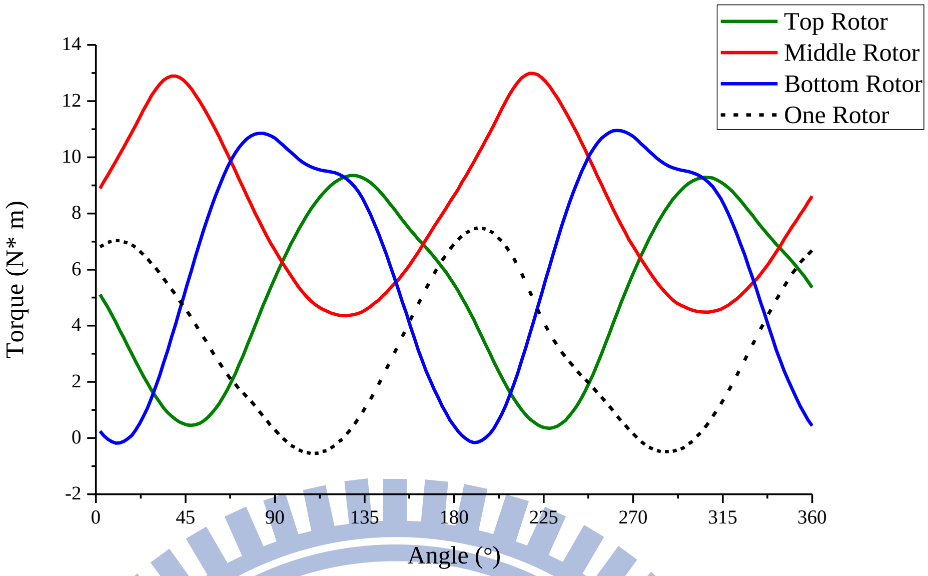

Fig. 4.21 Torque curves of the three Savonius wind rotor with phase angle difference 90° in wind speed 7 m/s at tip-speed ratio 0.9

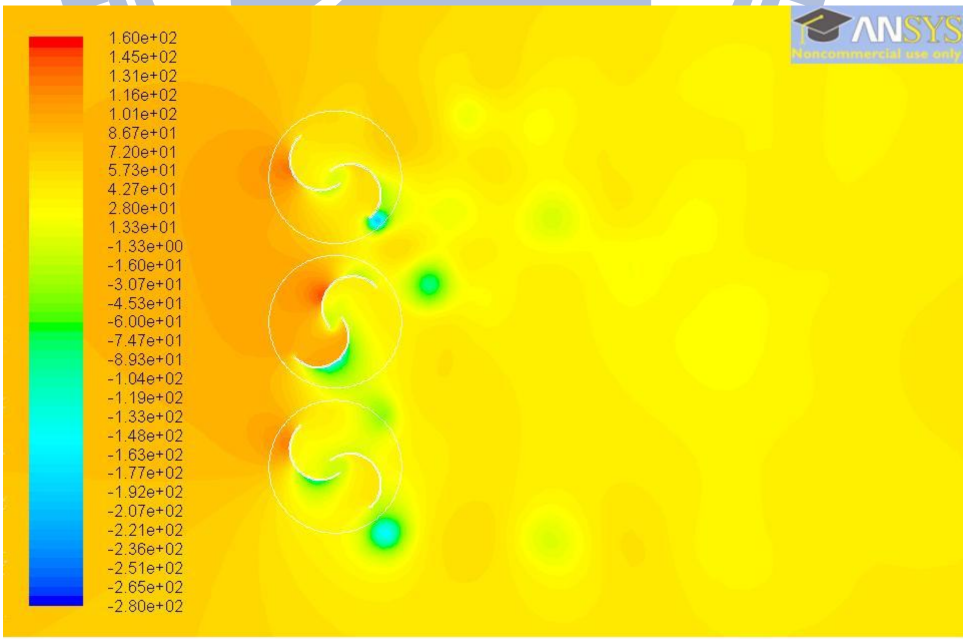

(a)

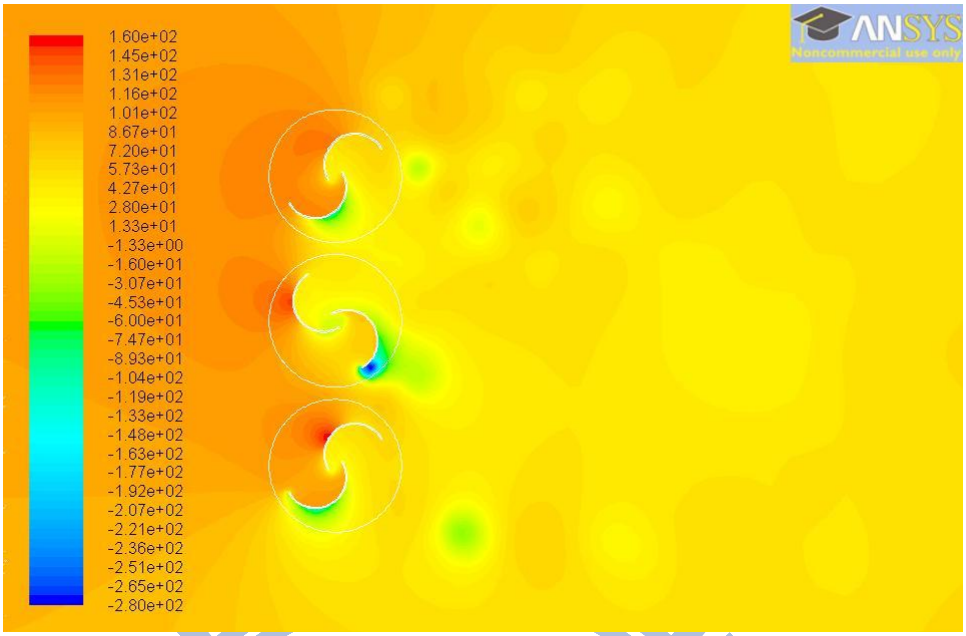

(b)

Fig. 4.22 Static pressure field around three Savonius wind rotors with phase angle difference 90° at: (a) *α*=40°; (b) *α*=120°

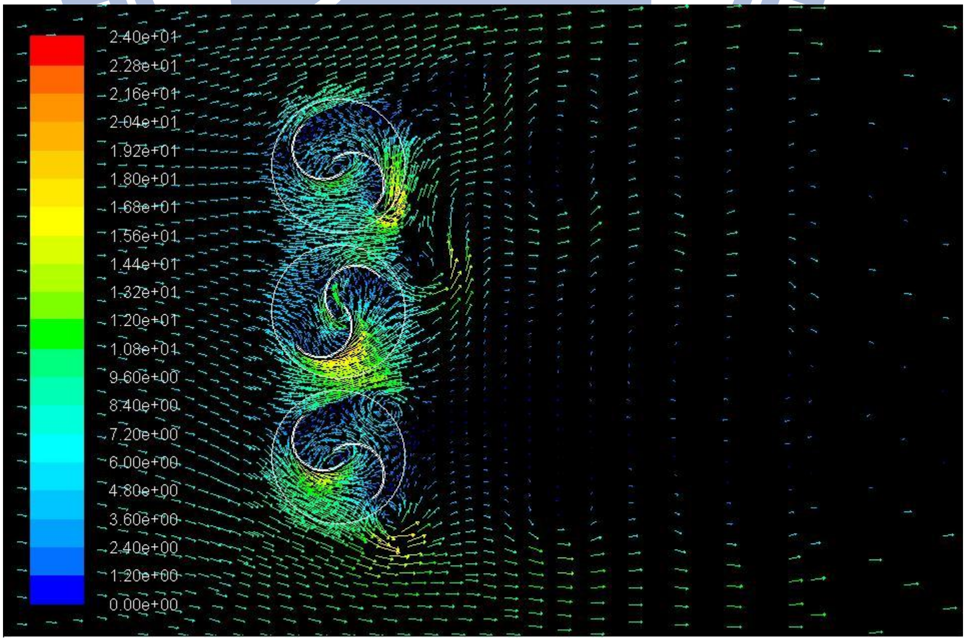

(a)

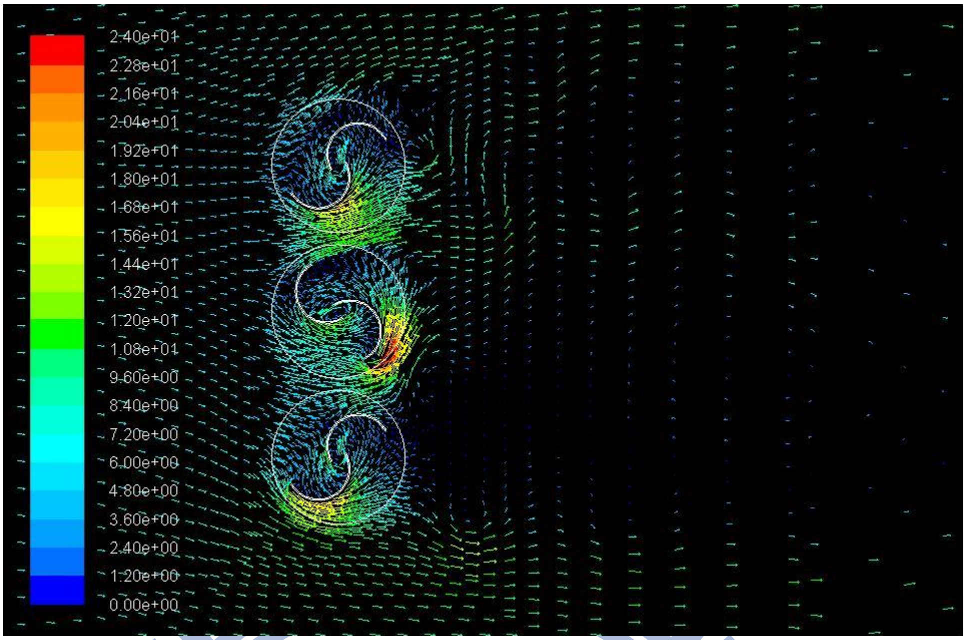

(b)

Fig. 4.23 Velocity vector distribution around three Savonius wind rotors with phase angle difference 90° at: (a) α=40°; (b) α=120°

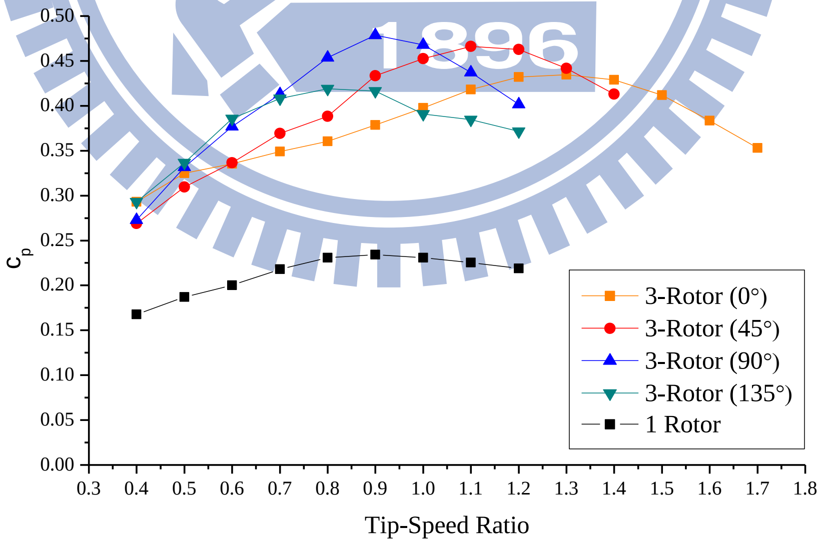

(a)

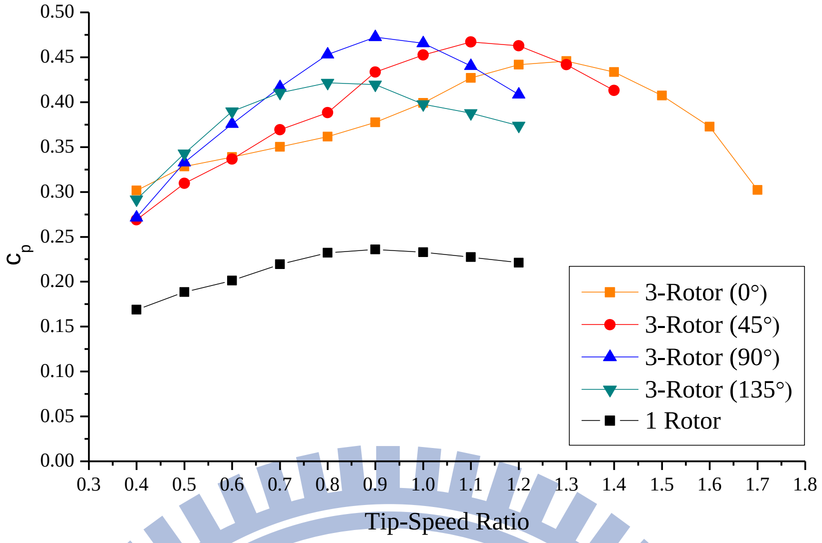

(b)

Fig. 4.24 Performances of three-rotor with different phase angle differences in 2-D simulation in: (a) wind speed 7 m/s; (b) wind speed 14 m/s

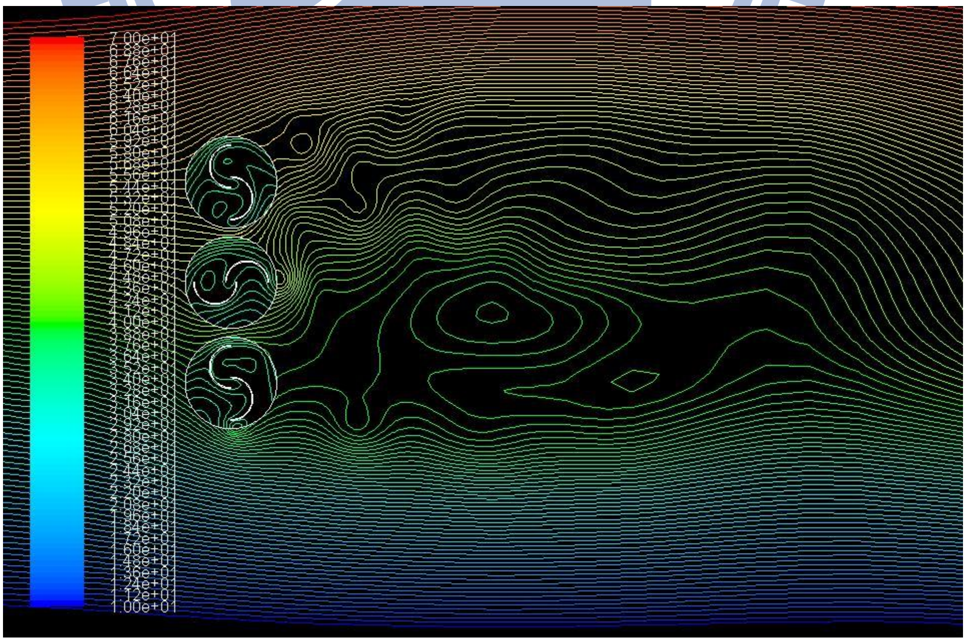

(a)

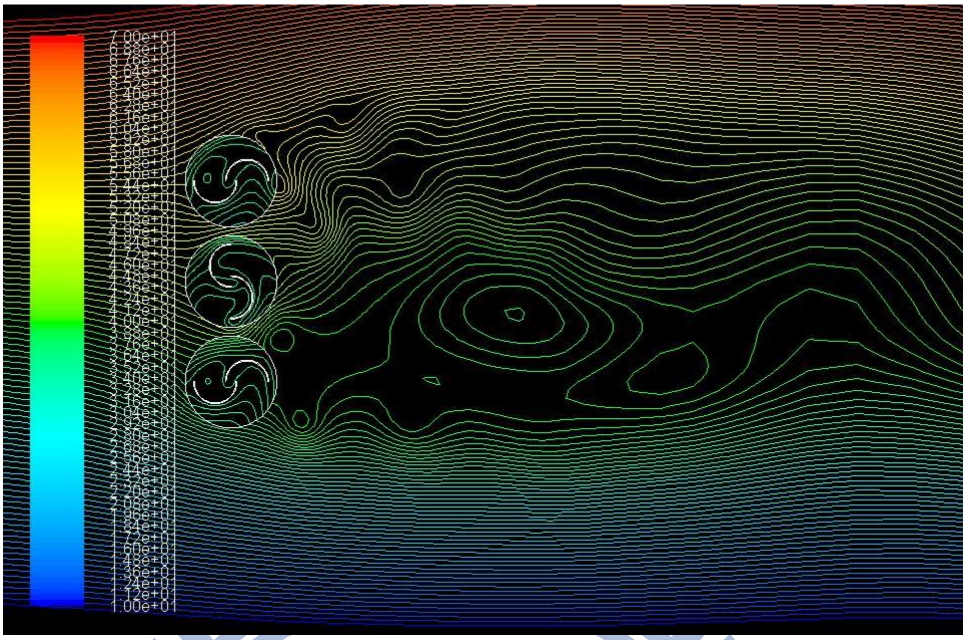

(b)

Fig. 4.25 Streamlines around three Savonius wind rotors with phase angle difference 90° at: (a) α=0°; (b) α=90°

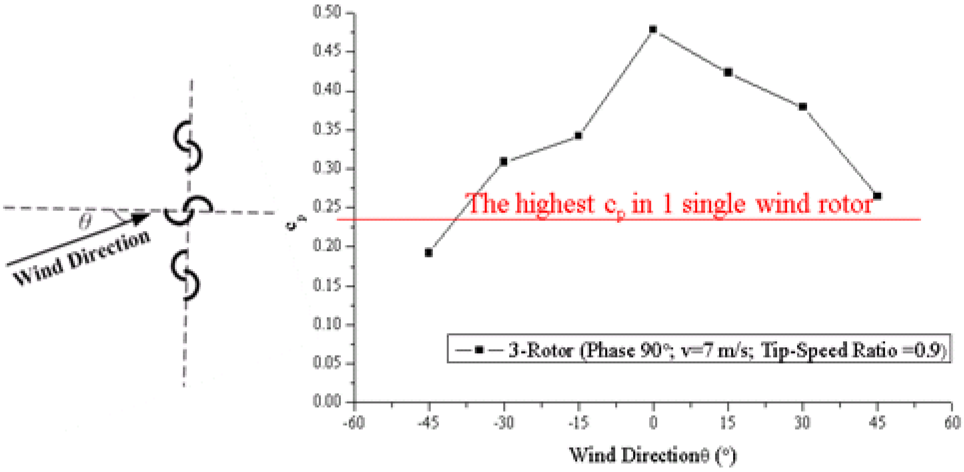

Fig. 4.26 Three-rotor with phase angle difference 90° in different wind directions

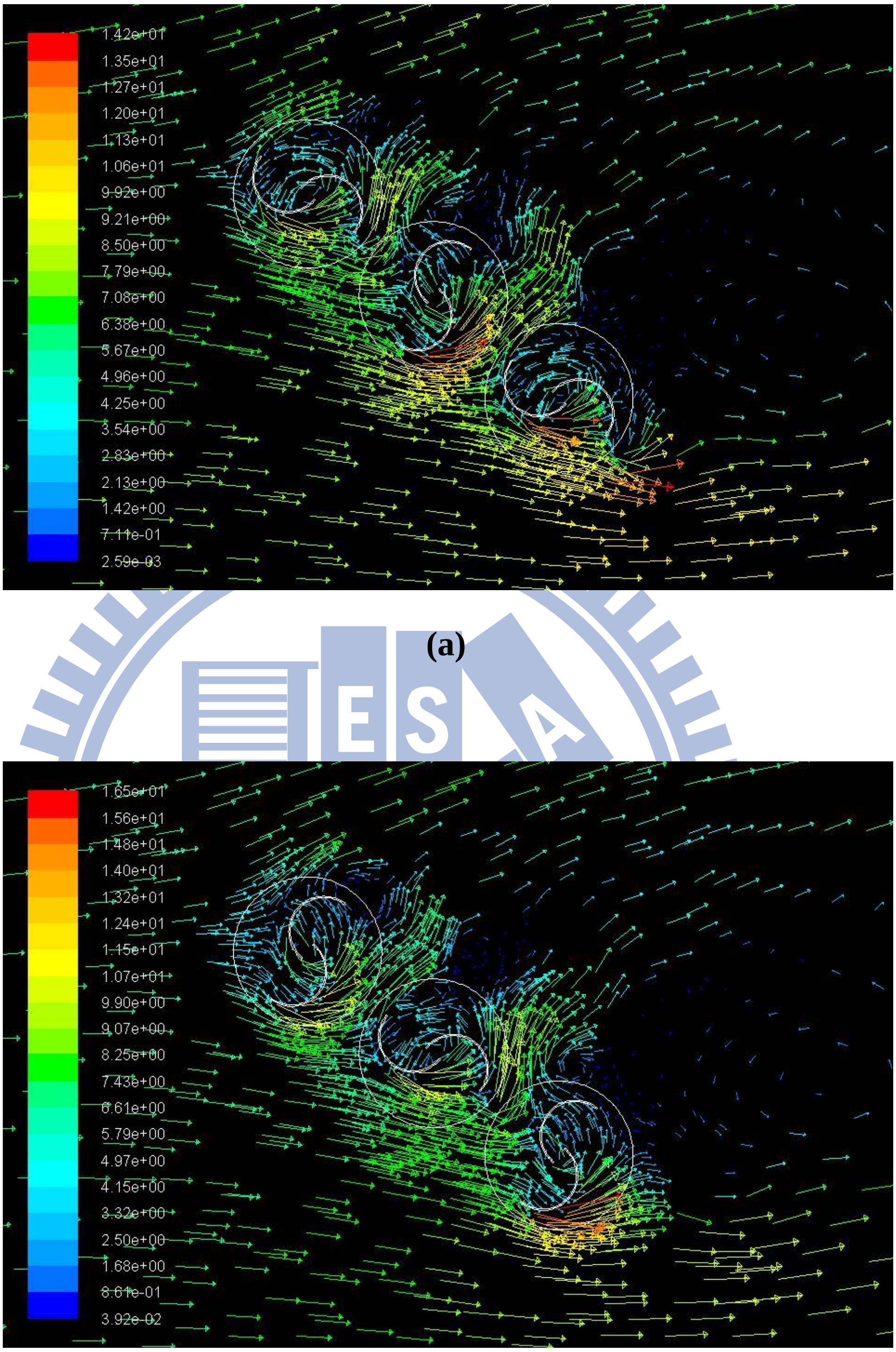

(a)

(b)

Fig. 4.27 Velocity vector distribution around the three Savonius wind rotors with a change of wind direction θ = -45° at: (a) α=0°; (b) α=90°

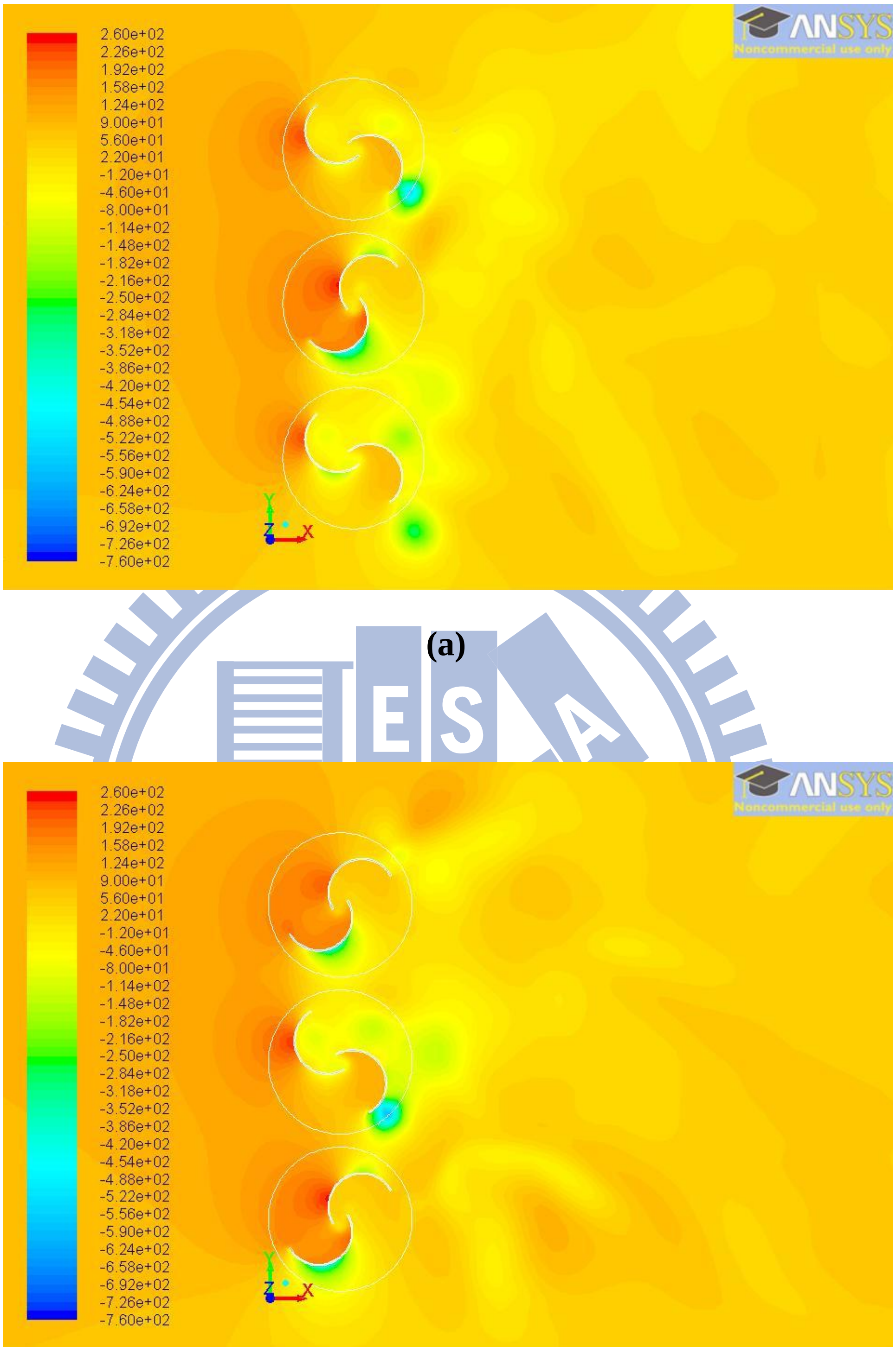

(a)

(b)

Fig. 4.28 Static pressure field around three Savonius wind rotors in 3-D simulation at z=1m and: (a) α=40°; (b) α=120°

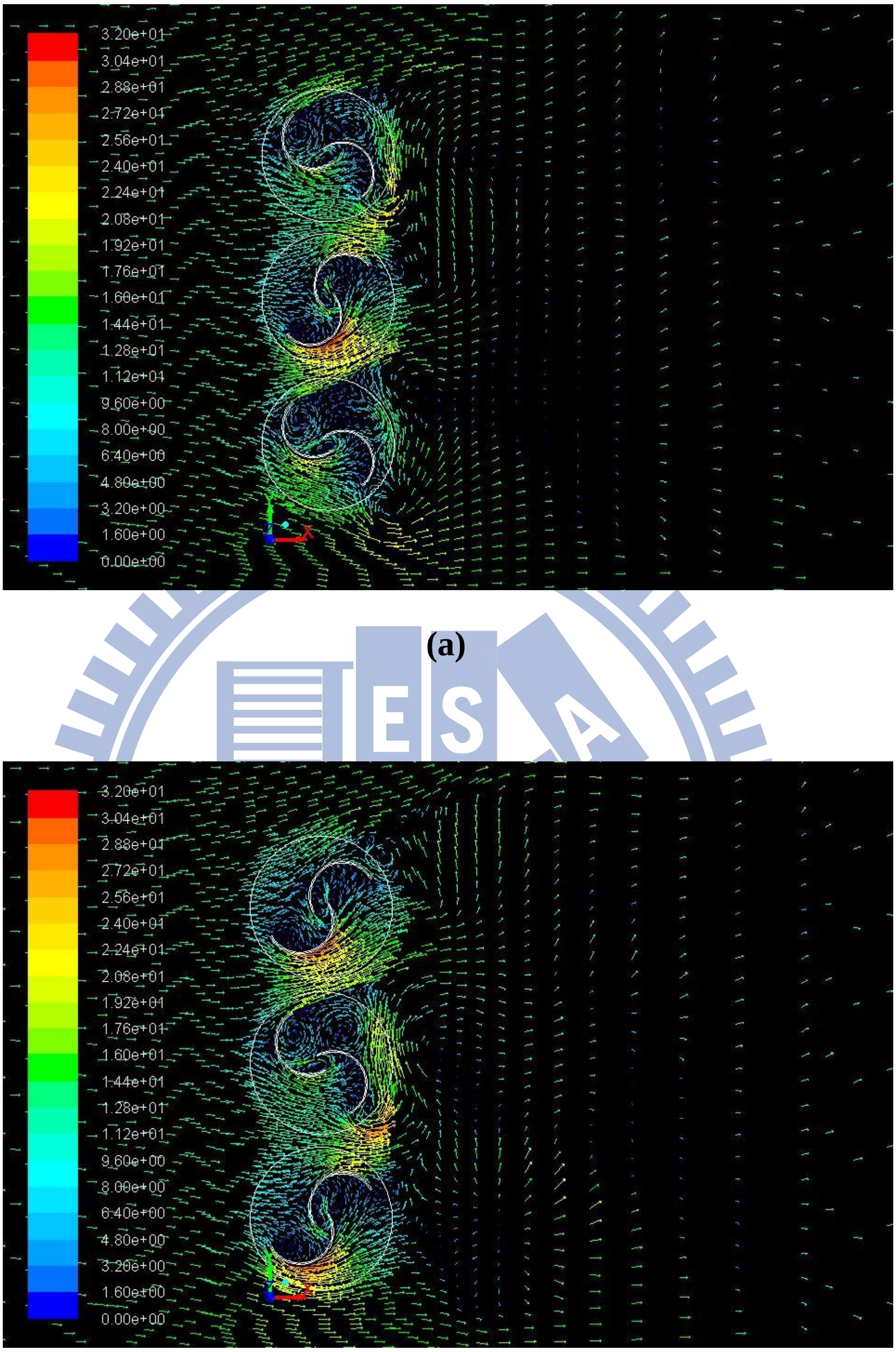

(a)

(b)

Fig. 4.29 Velocity vector distribution around three Savonius wind rotors in 3-D simulation at z=1m and: (a) α=40°; (b) α=120°

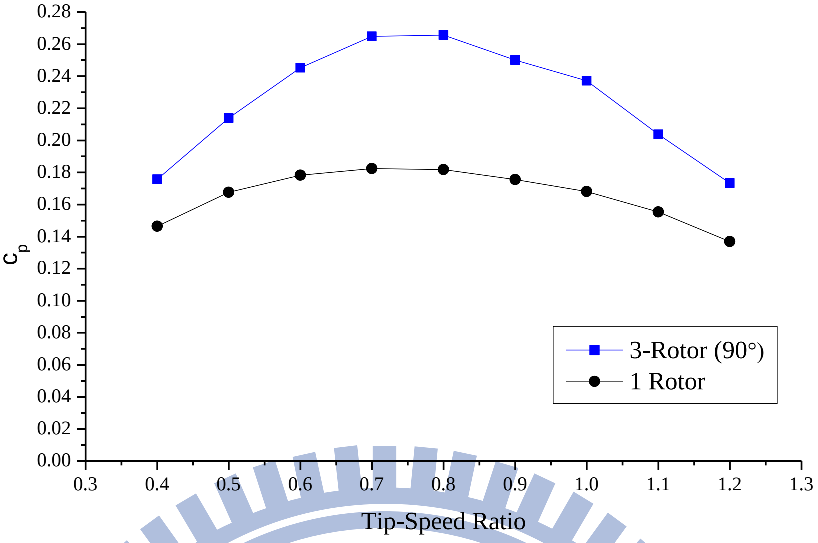

(a)

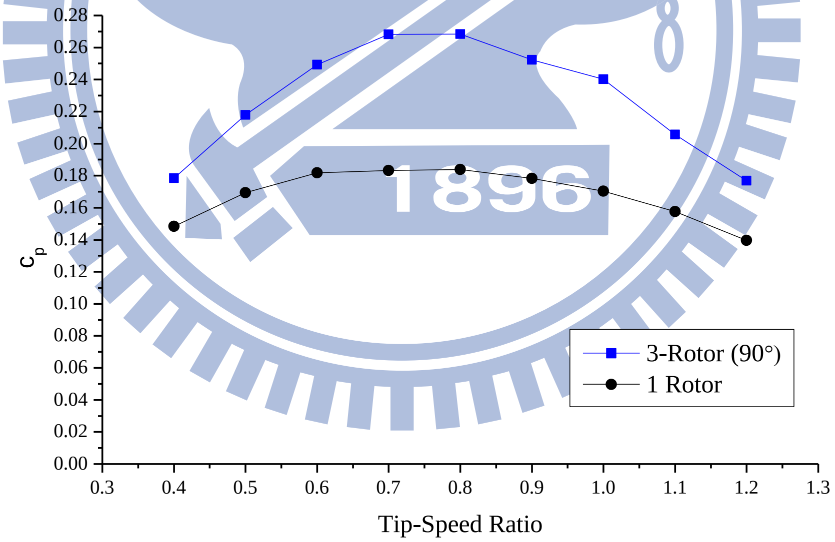

(b)

Fig. 4.30 Performances of three-rotor with phase angle difference 90° in 3-D simulation in: (a) wind speed 7 m/s; (b) wind speed 14 m/s

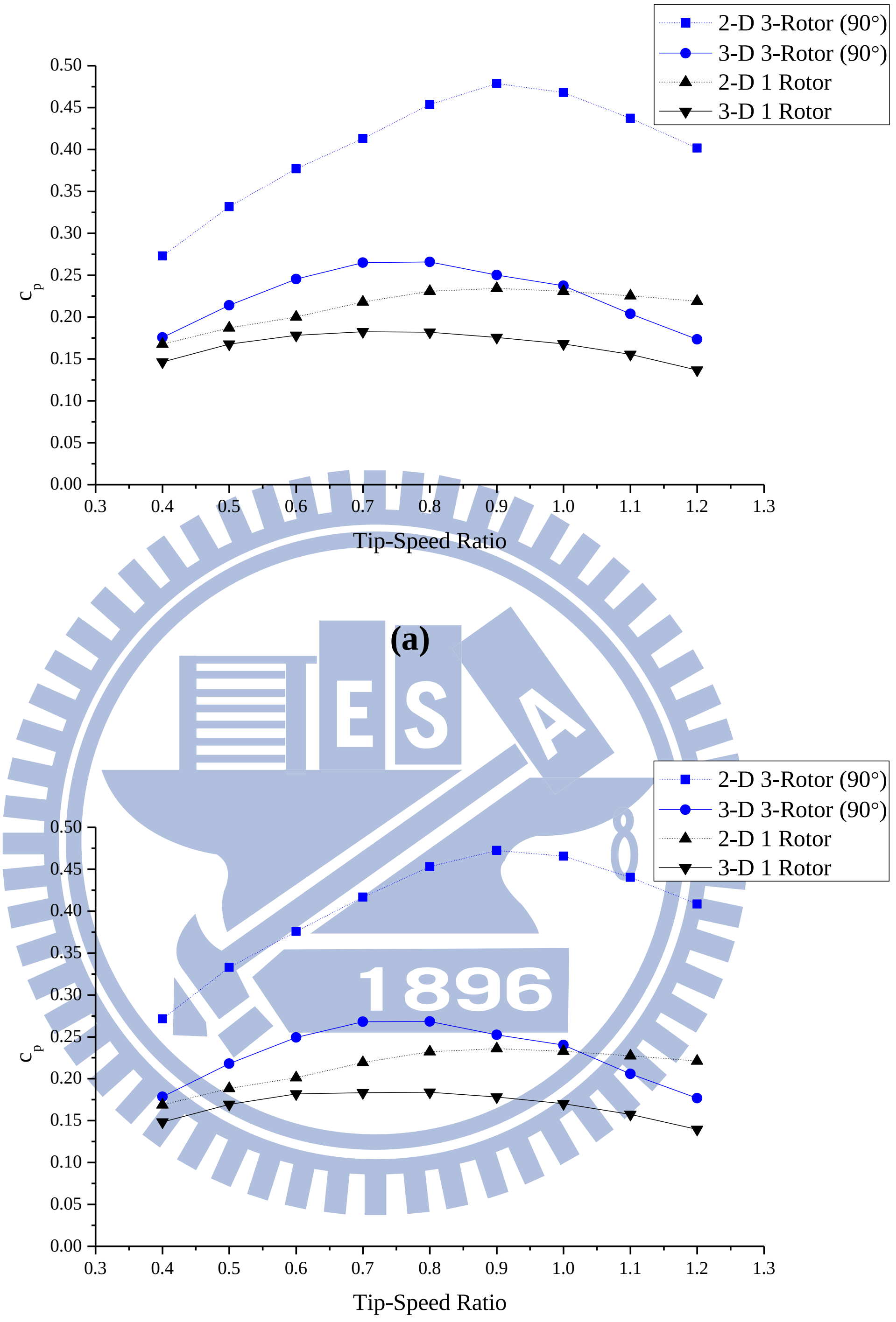

(a)

(b)

Fig. 4.31 Performance comparisons between 2-D and 3-D simulations in: (a) wind speed 7 m/s; (b) wind speed 14 m/s

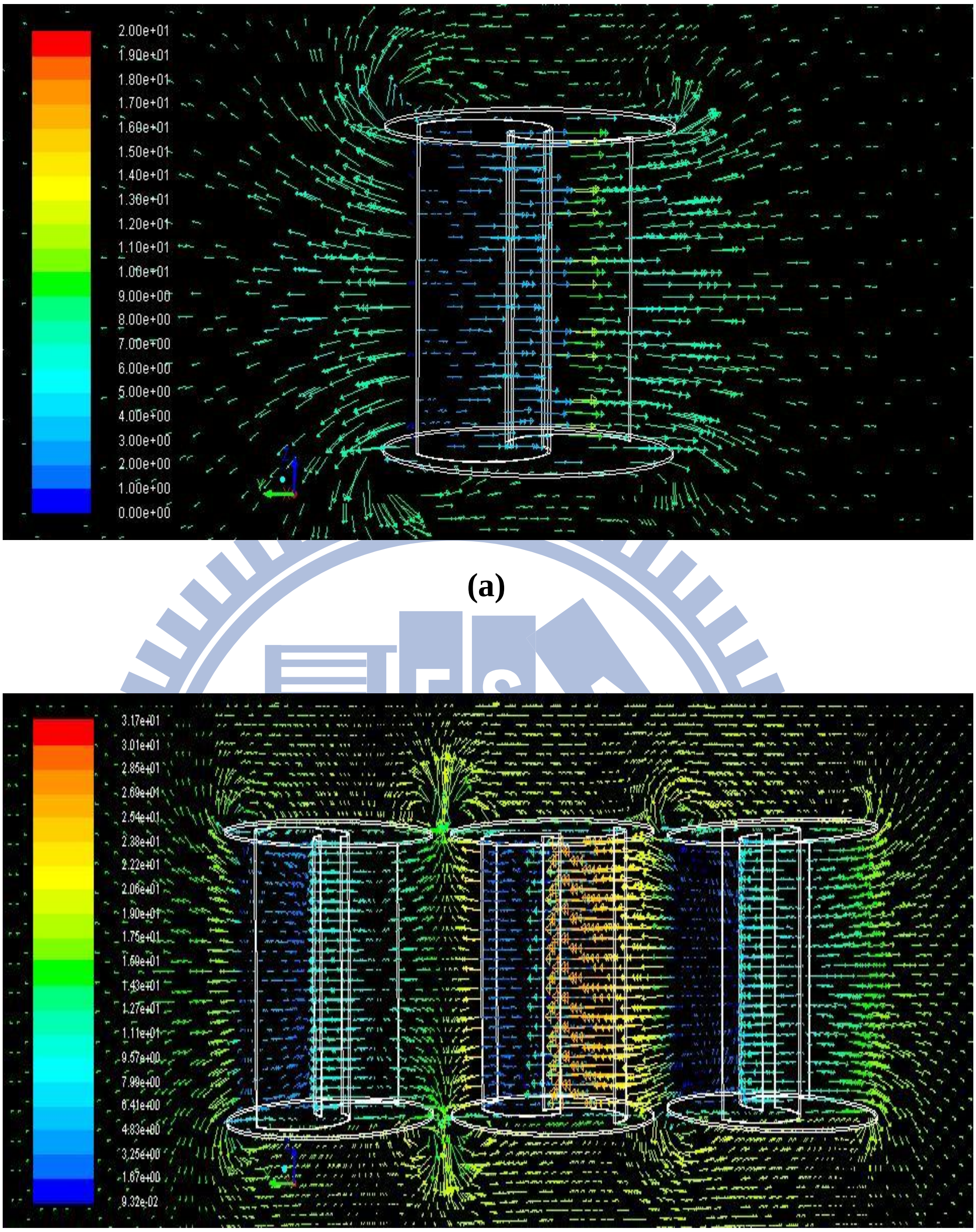

(a)

(b)

Fig. 4.32 Velocity vector distribution in 3-D simulations at x=0 around: (a) one single wind rotor; (b) three wind rotors

CHAPTER 5

CONCLUSIONS AND RECOMMENDATIONS

5.1 Conclusions

This study is divided into three parts. Firstly, the numerical investigation on performance of a single Savonius wind rotor is carried out and demonstrated. Two conditions, a single Savonius wind rotor inside the wind tunnel corresponding to the reference case and the one in atmosphere, are analyzed respectively. Secondly, a parallel matrix system, which includes three Savonius wind rotors rotating with the same angular speed, is demonstrated. And the performance comparison between a single rotor and three-rotor connected in parallel is carried out. Furthermore, the influence of wind direction change on the parallel system is also studied. Finally, comparisons with other researchers are given.

According to the simulation results, this study can obtain the following conclusions:

1. The 3-D simulation is more suitable than the 2-D one in dealing with this problem.
2. The c_p slightly increases with wind speeds at the same tip speed ratio in both 2-D and 3-D simulation.
3. The performance of one single Savonius wind rotor in atmosphere is lower than that inside the wind tunnel. The simulations carried out in atmosphere are more practical.
4. In the 2-D simulation results of parallel matrix system, the c_p with phase angle difference 135° is the worst, but it is still 1.79 times of that by a single Savonius wind rotor. Phase angle difference 90° can obtain the best c_p, which

is 2.05 times of that by a single Savonius wind rotor. The higher performance is resulted from the positive interaction between these Savonius wind rotors, and the flow fluctuation plays the major role in contributing to this effect.

5. The parallel matrix system is strongly influenced by the change of wind direction, representing that one of the advantages in VAWTs is lost. At the condition of three Savonius wind rotors with phase angle difference 90°, when $\theta = 45°$, its c_p stays almost the same as that of a single Savonius wind rotor; and when $\theta = -45°$, the c_p is even lower than that of a single one.
6. The 3-D simulation results show that either in wind speed 7 or 14 m/s, the maximal c_p in the parallel matrix system is about 1.45 times of that by a single Savonius wind rotor.
7. In the single Savonius wind rotor condition, the ratio of 2-D c_p to 3-D one is about 1.28; and in the parallel matrix system, the corresponding ratio is about 1.83.
8. The parallel matrix system seems to be regarded as a compromising way that does not need to change the geometry of the shape and also can obtain good promotion of c_p. But it still subjects to the restriction on wind directions, just like the method of adding a windshield.

5.2 Recommendations

This research has some lacks on the simulations. Followings are the recommendations for the parallel matrix wind rotor system:

1. Investigating the influences of distance between wind rotors on the parallel matrix system.
2. Studying the system with more than three wind rotors and observing its

influence.

3. Comparing simulation results with experimental data in the parallel matrix system.

REFERENCES

[1] Akinari Shigetomi, Yuichi Murai, Yuji Tasaka, and Yasushi Takeda, "Interactive flow field around two Savonius turbines", Renewable Energy, 36, pp.536-545, 2011.

[2] Sylvain Antheaumea, Thierry Maıtre, and Jean-Luc Achard, “Hydraulic Darrieus turbines efficiency for free fluid flow conditions versus power farms conditions” Renewable Energy, 33, pp. 2186-2198, 2008.

[3] Nobuyuki Fujisawa, “On the torque mechanism of Savonius rotors”, Journal of Wind Engineering and Industrial Aerodynamics, 40, pp. 277-292, 1992.

[4] Ben F. Blackwell, Robert E. Sheldahl, and Louis V. Feltz, “Wind tunnel performance data for two- and three-bucket Savonius rotors”, Journal of Energy, 2, pp.160-164, 1978.

[5] K. Pope, V. Rodrigues, R. Doyle, A. Tsopelas, R. Gravelsins, G.F. Naterer, and E. Tsang, “Effects of stator vanes on power coefficients of a zephyr vertical axis wind turbine”, Renewable Energy, 35, pp. 1043-1051, 2010.

[6] Robert Howell, Ning Qin, and Jonathan Edwards, Naveed Durrani, “Wind tunnel and numerical study of a small vertical axis wind turbine”, Renewable Energy, 35, pp. 412-422, 2010.

[7] Hu Yong-Hai and Tong Zheng-Ming, "The Influence of Windshield on Aerodynamic Performance of VAWT," 2009 International Conference on Energy and Environment Technology, iceet, vol. 1, pp.893-896, 2009.

[8] M.A. Kamoji, S.B. Kedare, and S.V. Prabhu, “Experimental investigations on single stage modified Savonius rotor”, Applied Energy, 86, pp.1064-1073, 2009.

[9] Burçin Deda Altan, Mehmet Atılgan, and Aydog˘an Özdamar, "An experimental study on improvement of a Savonius rotor performance with curtaining", Experimental Thermal and Fluid Science, 32, pp. 1673-1678, 2008.

[10]M.H. Mohamed, G.Janiga, E.Pap, and D.Thévenin, "Optimization of Savonius turbines using an obstacle shielding the returning blade", Renewable Energy, 35, pp. 2618-2626, 2010.

[11]U.K. Saha, S. Thotla, and D. Maity, "Optimum design configuration of Savonius rotor through wind tunnel experiments", Journal of Wind Engineering and Industrial Aerodynamics, 96, pp. 1359-1375, 2008.

[12]Zhenzhou Zhao, Yuan Zheng, Xiaoyun Xu, Wenming Liu, and Guoxiang Hu, “Research on the improvement of the performance of savonius rotor based on numerical study”, Sustainable Power Generation and Supply, pp.1-6, 2009.

[13]R. Gupta, R. Das, and K. Sharma, “Experimental Study of a Savonius-Darrieus Wind Machine”, Proceedings of the International Conference on Renewable Energy for Developing Countries, 2006.

[14]Kunio Irabu and Jitendro Nath Roy, “Characteristics of wind power on Savonius rotor using a guide-box tunnel”, Experimental Thermal and Fluid Science, 32, pp. 580-586, 2007.

[15]Rigoberto Chinchilla, Samuel Guccione, and Joseph Tillman, “Wind Power Technologies: A Need for Research and Development in Improving VAWT’s Airfoil Characteristics”, Journal of Industrial Technology, Volume 27, Number 1, 2011.

[16]Tsang-Jung Chang, Yu-Ting Wu, Hua-Yi Hsu, Chia-Ren Chu, and

Chun-Min Liao, “Assessment of wind characteristics and wind turbine characteristics in Taiwan”, Renewable Energy, 28, pp. 851-871, 2003.

[17]Hiroki Hondo, "Life cycle GHG emission analysis of power generation systems Japanese case", Energy, 30, pp. 2042-2056, 2005.

[18]Manfred Stiebler, “Wind Energy Systems for Electric Power Generation”, Springer-Verlag, Berlin Heidelberg, 2008.

[19]Erich Hau, “Wind Turbines: Fundamentals, Technologies, Application, Economics”, Springer-Verlag, Berlin Heidelberg, 2006.

[20]ANSYS FLUENT Theory Guide (Release 13.0), ANSYS Inc., 2010.